POLYTECHNIQUE MONTRÉAL

affiliée à l'Université de Montréal

Physical and Chemical Approaches for Water Micro-Droplet Capture

ALESSIO AUFOUJAL

Département de génie chimique

Mémoire présenté en vue de l'obtention du diplôme de *Maîtrise ès sciences appliquées*

Génie chimique

Mai 2020

POLYTECHNIQUE MONTRÉAL

affiliée à l'Université de Montréal

Ce mémoire intitulé :

Physical and Chemical Approaches for Water Micro-Droplet Capture

présenté par **Alessio AUFOUJAL**

en vue de l'obtention du diplôme de *Maîtrise ès sciences appliquées*

a été dûment accepté par le jury d'examen constitué de :

Daria Camilla BOFFITO, présidente
Jason Robert TAVARES, membre et directeur de recherche
Jean-Luc MEUNIER, membre et codirecteur de recherche
Anne-Marie KIETZIG, membre externe

DEDICATION

For Pauline

ACKNOWLEDGEMENTS

To both of my parents, Lina Pagliarulo and Michel Aufoujal, for fueling me with love and support throughout this endeavor. Thank you for always being there for me.

To my big brother, Sebastiano Aufoujal, who provided me with countless warm moments of laughter. Thank you for being my best friend.

A te bella nonna, Filomena Lo Russo, senza di te tutto questo non saresti possibile. Grazie di essere une donna inspirante.

To Pauline, for sharing the most valuable of resources a person has with me, time. Your love and care are a bottomless well for me. Thank you for being the woman that you are.

To my PhotoSEL lab colleagues, for your creativity, thoughtful discussion and now friendships. Thank you for building a beyond enjoyable work environment.

Thank you to the Natural Sciences and Engineering Research Council of Canada (NSERC) for financing this ambitious project. It brings me much faith and hope to know that important subject matter receives attention from important organizations still. I would also like to thank AWN Nanotech, for funding this research and initiating work on a pressing world issue. The strong research team we built and the efforts we continue invest will, in time, greatly benefit our vision for this project.

Thank you to the jury, for taking the time to read and evaluate this master's thesis.

Thank you to my co-director, Jean-Luc Meunier, for being an endless source of knowledge and wisdom from the very beginning. Your maturity has always inspired me, and I consider it a privilege to have shared this time with you.

Finally, thank you to my research director, Jason Robert Tavares. Thank you for seeing potential and believing in it. You are an example for all of your students and your peers. I would specifically like to thank you for your openness which was most surprising to me in my first explorations in the world of academia. I never thought to have such a constructive and dynamic relationship with my director. You always allowed me to do both the easiest and most difficult thing in my experiments: try. This made for two years of few major successes after many minor failures. Nevertheless, a learning experience I will always cherish. For that alone, I am forever grateful.

RÉSUMÉ

La pénurie d'eau est devenue un enjeu pressant dans le monde d'aujourd'hui. Sur la planète, 1,2 milliard de personnes n'ont pas accès à de l'eau propre et 2,7 milliards vivent en pénurie au moins un mois par an. Bien que cette ressource couvre 71 % de la surface de la Terre, seulement 2,5 % de celle-ci est accessible par des sources conventionnelles telles que les lacs et les eaux souterraines. Celles-ci se remplissent naturellement grâce au cycle de l'eau. Les sécheresses sont devenues plus fréquentes ces dernières années et ne font que s'aggraver avec les changements anthropiques apportés au climat. De plus, la population mondiale ne cesse de croître alors que la quantité d'eau renouvelable est en décroissance. Cette situation se traduit par une augmentation de la demande et une diminution de l'offre. Cela est dû en grande partie à l'industrialisation rapide depuis les années 1960, qui a entraîné une forte utilisation des ressources en eau. Pour répondre à cette demande, des processus de production d'eau douce, tel que l'osmose inverse sont des solutions plus en plus intéressantes. L'osmose inverse est devenue plus rentable au cours de la dernière décennie avec un coût d'exploitation de 0,50 $US par m^3 d'eau. Toutefois, ce procédé nécessite la disponibilité de grandes quantités d'eau salée et d'énergie électrique pour fonctionner. Pour les régions intérieures ou non côtières, ce coût peut être prohibitif en raison de l'importance des investissements et des coûts d'opération. En revanche, l'atmosphère contient 13 000 km^3 d'eau douce sous forme de vapeur, de gouttelettes liquides et sous forme solide (neige ou glace). Bien qu'elle ne soit pas facilement disponible, cette eau peut être extraite et purifiée en eau potable. Ainsi, la récolte du brouillard, un processus par lequel des microgouttelettes d'eau sont capturées par une surface et traitées pour une consommation ultérieure, est apparue comme une méthode alternative pour la production d'eau potable. Cette méthode consiste généralement à utiliser un matériau polymérique maillé permettant de capturer le brouillard à son contact. À l'heure actuelle, les principaux inconvénients dans ce domaine sont la dégradabilité des matériaux utilisés, due à l'exposition à des vents violents ou à des débris transportés dans l'air par exemple, et la faible efficacité de la collecte due à une mauvaise conception de la surface.

L'objectif principal de ce projet est de concevoir et de construire un dispositif optimisé de récolte de brouillard. La performance dépend de la capacité d'une surface à capturer continuellement les micro-gouttelettes d'eau entrantes, puis à évacuer rapidement cette eau. Cela implique qu'une surface doit présenter des propriétés d'adhésion appropriées pour assurer qu'un maximum de micro-

gouttelettes adhèrent à la surface lors de l'impact, mais aussi des propriétés répulsives qui permettent d'éliminer facilement cette eau afin de régénérer la surface. Des propriétés telles que la géométrie, la topologie et la chimie de la surface sont donc fortement impliquées dans le processus de conception d'une surface efficace de récolte de brouillard. La géométrie joue un rôle dans l'optimisation de l'efficacité aérodynamique de l'écoulement du brouillard. Dans les conceptions de type maille, il est possible que la zone ouverte se colmate lorsque les gouttelettes se coalescent entre elles. Cela affecte négativement l'écoulement, ce qui entraîne une diminution de la quantité d'eau qui entre en contact avec la surface de récolte. En outre, lorsque les pores sont bouchés, les forces d'adhésion sont augmentées, ce qui rend plus difficile l'élimination de l'eau. La topologie et la chimie des surfaces jouent également un rôle important pour adapter l'interaction des surfaces avec l'eau. Cela peut être réalisé par la fonctionnalisation pour obtenir des mouillabilités propices. Le dépôt chimique en phase vapeur photo-initié (PICVD) est une technique de dépôt de couches minces peu coûteuse, peu énergétique et avec une bonne capacité de mise à l'échelle. Cette méthode est capable de produire une large gamme de mouillabilité sur un substrat, allant de super-hydrophile à super-hydrophobe, en variant les paramètres de traitement. Cependant, dans les dépôts super-hydrophiles, un phénomène de vieillissement connu sous le nom de recouvrement hydrophobe se produit. Il s'agit d'un processus par lequel un certain pourcentage de groupes fonctionnels mobiles oxygénés se diffuse et se réoriente vers l'intérieur du film plutôt que de rester près de la surface et, ce faisant, supprime le caractère hydrophile de la surface.

Dans l'ouvrage suivant, un dispositif efficace et modulable de récolte du brouillard est décrit. Une étude paramétrique sur les variables de conception est présentée. Pour traiter les questions relatives à la durabilité, la sélection des matériaux pour le dispositif est cruciale. L'acier inoxydable a été choisi comme un matériau approprié. L'effet de la géométrie sur le taux de collecte du brouillard a été étudié en comparant l'utilisation de substrats en forme de maille et d'un réseau de fils alignés verticalement, régulièrement espacés, appelé "harpe". Le taux de collecte de l'eau, qui représente les grammes d'eau collectés par heure et par cm^2, s'est avéré significativement amélioré dans ce dernier cas, atteignant des taux jusqu'à 10 fois supérieurs à ceux des mailles. L'effet de la topologie et de la chimie de surface a été étudié en faisant pousser une forêt de nanotubes de carbone sur les substrats en acier inoxydable et en modifiant sa mouillabilité par la fonctionnalisation via PICVD. Afin de contrer la récupération hydrophobe et d'obtenir une surface super-hydrophile stable, un

nouveau protocole PICVD a été développé. Enfin, une analyse approfondie des paramètres de conception de la "harpe" a été réalisée. Ces paramètres inclus l'espacement des fils, le diamètre des fils, l'angle d'inclinaison, la mouillabilité, l'ajout d'un étage secondaire et la vibration. Cela a permis de concevoir une "harpe" optimisée et d'en construire une version à grande échelle. Les principales recommandations pour les travaux futurs sont d'étudier plus en détail la mouillabilité de ce dispositif de collecte de brouillard. L'ajout de motifs de mouillabilité ou un mouillage hétérogène, pourrait éventuellement répondre aux deux critères nécessaires à l'optimisation de la récolte : améliorer la capture de l'eau dans les régions hydrophiles et accélérer l'élimination des gouttelettes dans les régions hydrophobes. Enfin, il est fortement recommandé de réaliser des expériences de récolte du brouillard dans des conditions réelles avec la harpe à grande échelle.

ABSTRACT

Water scarcity has become a pressing issue in today's world. On the planet, 1.2 billion people do not have access to clean freshwater and 2.7 billion experience this scarcity a minimum of one month out of the year. Although this resource covers 71% of the earth, a mere 2.5% of it is accessible through conventional sources such as lakes and groundwater that are naturally replenished through the water cycle. Droughts have become more common in the past years and is only getting worse with anthropogenic changes brought to the climate. Moreover, the world's population continues to grow as the amount of renewable water decreases. This results in an increase in demand and a decrease in supply. This trend is largely due to the rapid industrialization as of the 1960s, forcing heavy usage of water resources. To fulfill this demand, processes for intensive production of freshwater such as reverse osmosis (RO) have become more and more interesting. However, this process requires the availability of large bodies of saline water as feedstock and high amounts of electrical power. For inland or noncoastal regions, this can be cost prohibitive due to high capital investment and operational costs. On the other hand, Earth's atmosphere holds 13 000 km^3 of freshwater in the atmosphere present in vapor, liquid droplets and solid (snow or ice) form. Although not readily available, this water can be extracted and purified into potable water. Thus, fog harvesting, a process by which water micro-droplets are captured by a surface and treated for further consumption, has emerged as an alternative method for freshwater generation. This is typically done by employing a mesh-like polymeric material through where fog is capture upon contact. At this time, major drawbacks in this field are the durability of widespread materials used for fog harvesting, stemming from exposure to high wind speeds or debris carried in the air for instance, and the low collection efficiency due to poor surface design.

The main goal of this project is to design and construct an optimized fog harvesting device. Fog harvesting performance relies on the ability of a surface to continuously capture incoming water micro-droplets followed by rapid shedding of this water. This implies that a surface must exhibit appropriate adhesion properties to assure that a maximum of fog micro-droplets stick to the surface upon impaction but also repelling properties that allow for easy removal of this water in order to regenerate the surface. Properties such as geometry, surface topology and surface chemistry are therefore heavily involved in the process of designing an efficient fog harvesting surface. Geometry plays a role in optimizing the aerodynamic efficiency of fog flow. In mesh-like designs, clogging

can occur when water droplets on the surface grow to the point of blocking the open area of the mesh. This negatively affects fog flow resulting in a decrease in the amount of incoming water micro-droplets to come into contact with the fog harvester. Additionally, when pores get clogged, the adhesion forces between water and the surface are increased, making it more difficult to further remove the water. Surface topology and chemistry have been found to play an important role as well, for tailoring the surfaces interaction with water. This can be achieved through functionalization to achieve desired wettabilities. Photo-initiated chemical vapor deposition (PICVD) is a low cost, low energy and scalable gas phase thin film deposition technique. This method is capable of producing a wide range of wettabilities on a substrate from super-hydrophilic to superhydrophobic through varying processing parameters. However, in super-hydrophilic depositions, an aging phenomenon known as hydrophobic recovery occurs. This is a process by which a certain percentage of oxygenated mobile functional groups diffuse and reorient themselves towards the bulk of the film rather than remain near the surface and, in doing so, removing the hydrophilicity of the surface.

In the following work, an efficient and scalable fog harvesting device is described. A study on several design variables is presented. This was done as a first look into the possibilities and highlights important aspects to consider when designing a fog harvesting surface. To address issues regarding durability, material selection for the fog harvesting device was crucial. Stainless steel was selected as an appropriate material. The effect of geometry on fog collection rate is studied by comparing the use of mesh-like substrates and an array of evenly spaced taut vertically aligned wires, named “harps”. Water collection rate, measured in grams of water collected per hour per cm^2, was found to be significantly improved in harps, achieving rates up to 10 times higher than meshes. The effect of surface topology and surface chemistry was explored by growing a carbon nanotube forest on the stainless-steel substrates and altering its wettability through PICVD functionalization. In order to counter hydrophobic recovery and achieve a stable super-hydrophilic surface, a novel PICVD protocol was developed. Finally, a thorough analysis of harp design parameters was performed. These parameters were wire spacing, wire diameter, tilt angle, wettability, secondary stage addition and vibration. This led to the optimal design of the harp and allowed for the construction of a large-scale version of it. The main recommendations for future work are to further investigate the possibilities involving wettability in the design of this fog

harvester. Introducing surface wettability patterns (heterogeneous wettability) would possibly meet both criteria necessary for improved fog harvesting: enhancing water capture in hydrophilic regions and accelerating droplet shedding in hydrophobic ones. Lastly, it is highly recommended to perform fog harvesting experiments in real-life conditions with the large-scale harp.

TABLE OF CONTENTS

LIST OF TABLES

LIST OF FIGURES

LIST OF SYMBOLS AND ABBREVIATIONS

A	Surface area
A_{op}	Opening area
APCVD	Atmospheric pressure chemical vapor deposition
AWG	Atmospheric water generation
c	Pitch
C_d	Drag coefficient
C_o	Pressure loss coefficient
CA	Contact angle
CNT	Carbon nanotubes
CVD	Chemical vapor deposition
D	Wire diameter
E_b	Binding energy
E_k	Kinetic energy
$F_{adhesion}$	Adhesion force
F_g	Gravitational force
F_L	Laplace pressure force
F_{wd}	Wettable different force
F_{wg}	Wettable gradient force
FEG	Field-emission guns
FRP	Free radical polymerization
ΔG	Gibbs free energy
ΔG^*_{hetero}	Critical Gibbs free energy for heterogeneous nucleation
ΔG^*_{homo}	Critical Gibbs free energy for homogeneous nucleation
GDP	Gross domestic product
ΔH	Change in enthalpy
HMDSO	Hexamethyldisiloxane
hv	Photon energy
k_b	Boltzmann constant
K_T	Equilibrium constant
LFC	Large fog collector
LWC	Liquid water content
MOCVD	Metal-organic chemical vapor deposition
MOF	Metal-organic framework
MPACVD	Microwave plasma-assisted chemical vapor deposition
N_x	Number of moles of x
P	Pressure
p_{sat}	Saturation vapor pressure
p_{water}	Water vapor pressure
PDMS	Poly(dimethylsiloxane)
PDMS	Polydimethylsiloxane
PDVB	polydivinylbenzene
PECVD	Plasma-enhanced chemical vapor deposition
PGMA	poly(glycidil methacrylate)

pHEMA	poly(2-hydroxylethyl methacrylate)
PICVD	Photo-initiated chemical vapor deposition
PLD	Pulsed layer deposition
PMMA	poly(methyl methacrylate)
PP	Polypropylene
PPF	Plasma polymer film
PPHA	Plasma polymerized heptylamine
PS	Polystyrene
PTFE	Polytetrafluoroethylene
R	Ideal gas constant
r^*	Critical radius
$r_{cluster}$	Cluster Radius
r_{wire}	Wire radius
Re	Reynolds number
RF	Radio frequency
RH	Relative humidity
RO	Reverse osmosis
S	Saturation ratio
ΔS	Change in entropy
SC	Shade coefficient
SE	Secondary electrons
SEM	Scanning electron microscopy
SFC	Standard fog collector
SS	Stainless steel
SS-CNT	Stainless steel carbon nanotube
St	Stokes number
T	Temperature
TACVD	Thermally activated chemical vapor deposition
USD	US dollar
UVC	Ultraviolet-C
UVC	Ultraviolet
V	Wind speed
VCG	Vertical chemical gradient
W_a	Work of adhesion
XPS	X-Ray Photoelectron Spectroscopy
α	Half angle
η_a	Aerodynamic efficiency
$\eta_{collection}$	Collection efficiency
η_d	Deposition efficiency
γ	surface tension
γ_{lv}	Liquid-vapor surface tension
γ_{sl}	Solid-liquid surface tension
γ_{sv}	Solid-vapor surface tension
μ_{air}	Viscosity of air
ϕ	Work function

ρ_{air}	Density of air
σ	Surface specific energy
θ	Contact angle
$\theta_{a-philic}$	Advancing contact angle in a hydrophilic region
θ_{avg}	Average contact angle
θ_{CB}	Cassie-Baxter contact angle
θ_{philic}	Contact angle in a hydrophilic region
$\theta_{r-phobic}$	Receding contact angle in a hydrophobic region

CHAPTER 1 INTRODUCTION

1.1 Context

Water is a fundamental resource for all living beings on Earth. It covers approximately 71% of the its surface, yet a mere 2.5% is considered to as freshwater and, thus, directly consumable for human beings [1], [2]. Figure 1 shows the distribution of water in all major sources.

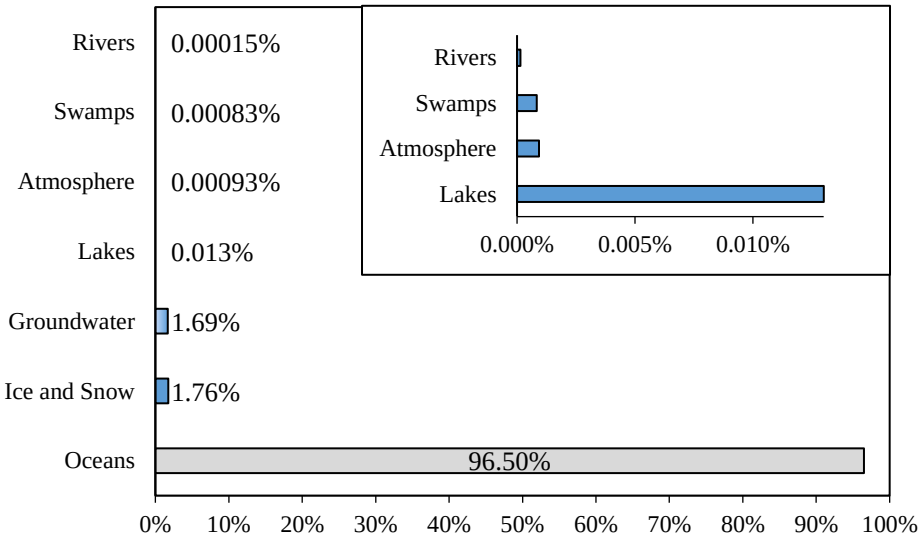

Figure 1. Distribution of water on the planet [3]

Considering a relatively constant total of 1.4 billion km^3 of water on the planet, this would leave 35 million km^3 of available freshwater (1 cubic kilometer is equivalent to 1 trillion liters). This freshwater, nonetheless, is not readily available as it is distributed amongst diverse sources, primarily in ice and snow (69%) and groundwater (30%) [3]. The remainder of the 1% is found in soil moisture, freshwater lakes, atmosphere, swamps, rivers and biological water [3]. Hence, roughly 10.5 million km^3 of freshwater, originating from groundwater and surface water, is truly used to fuel our consumption habits. Despite the inaccessibility of these major sources, the entire human civilization has been able to prosper with these mere amounts of water, relative to the totality. However, this image of prosperity does not reflect the entire situation as water scarcity has become a serious environmental issue for a significant amount of people worldwide. In the 20^{th} century alone, water consumption has quadrupled, yet individuals threatened by scarcity has grown from 14 to 58% of the global population [4]. This is largely due to overexploitation of this precious

resource [1], [2], [5]. As shown in Figure 2 (a), the world's total renewable internal freshwater per capita has been rapidly decreasing over the past decades, where internal freshwater refers to the amount of freshwater available in sources that are replenished through the hydrological cycle (rivers, groundwater, lakes etc.) [6]. In other words, water is being extracted at a higher rate than its being naturally renewed through the water cycle. All the while, world population has been on a steady climb. As population increases, need for food will inevitably increase causing a higher demand of water for agricultural purposes. On a global scale, water usage for agriculture (food crops, livestock, biofuels etc.) through rainfall or irrigation systems, accounts for approximately 70% [7]. In turn, this percentage greatly varies depending on the level of development of a country. Developed countries dedicate 41% of water on agriculture while this share increases to 79% and 90% in middle and low-income countries respectively [8]. Juxtaposing these values with freshwater usage in industry, the inverse relationship appears, with a larger share in high-income countries compared to those with low income. In 2017, Canada, for instance, allocated 30% of its potable water to industrial, commercial, institutional and other non-residential sectors [9]. This trend coincides with an increase in Gross Domestic Product (GDP) as shown in Figure 2 (b) [10]. Figure 2 (a) drastically expresses the inability to meet freshwater needs of the entire human mass on the planet. Observing the data, it becomes clear that the pressure stemming from water overexploitation in both domestic and industrial uses, urbanization and climate change are overwhelming and increase the difficulty to sustainably manage this fundamental resource.

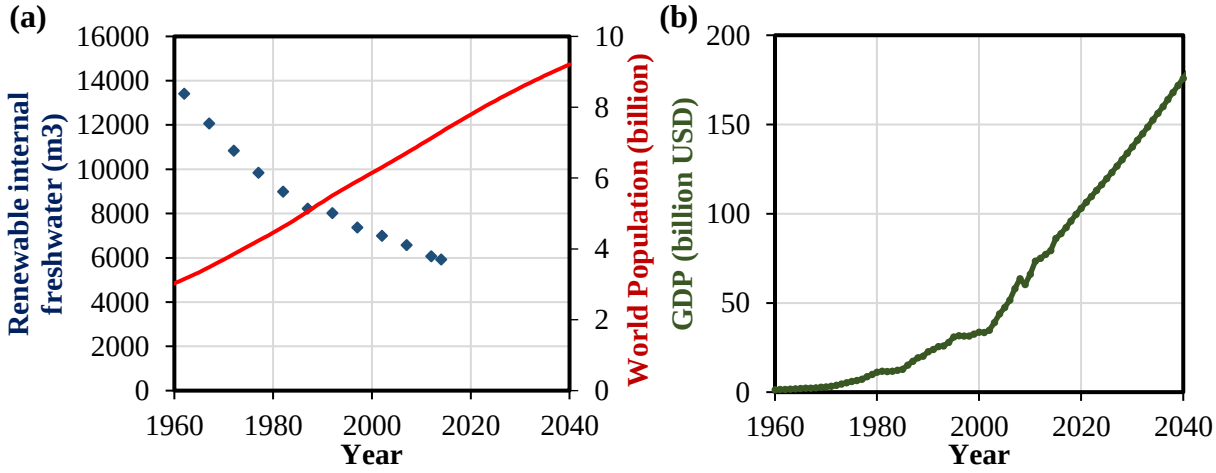

Figure 2. (a) Renewable freshwater per capita and World population, (b) Gross domestic product from 1960-2040 [6], [10]

Water scarcity can be expressed as shortage and stress. Shortage refers to the impacts of having low water availability per capita and stress is the impact resulting from a higher withdrawal compared than the available supply [4]. Figure 3 shows the evolution of water stress in the next 20 years. This dilemma is two-fold in which first-order scarcity describes the lack of water as a resource and second-order scarcity represents hydropolitics – the social pressure on managing this resource [5].

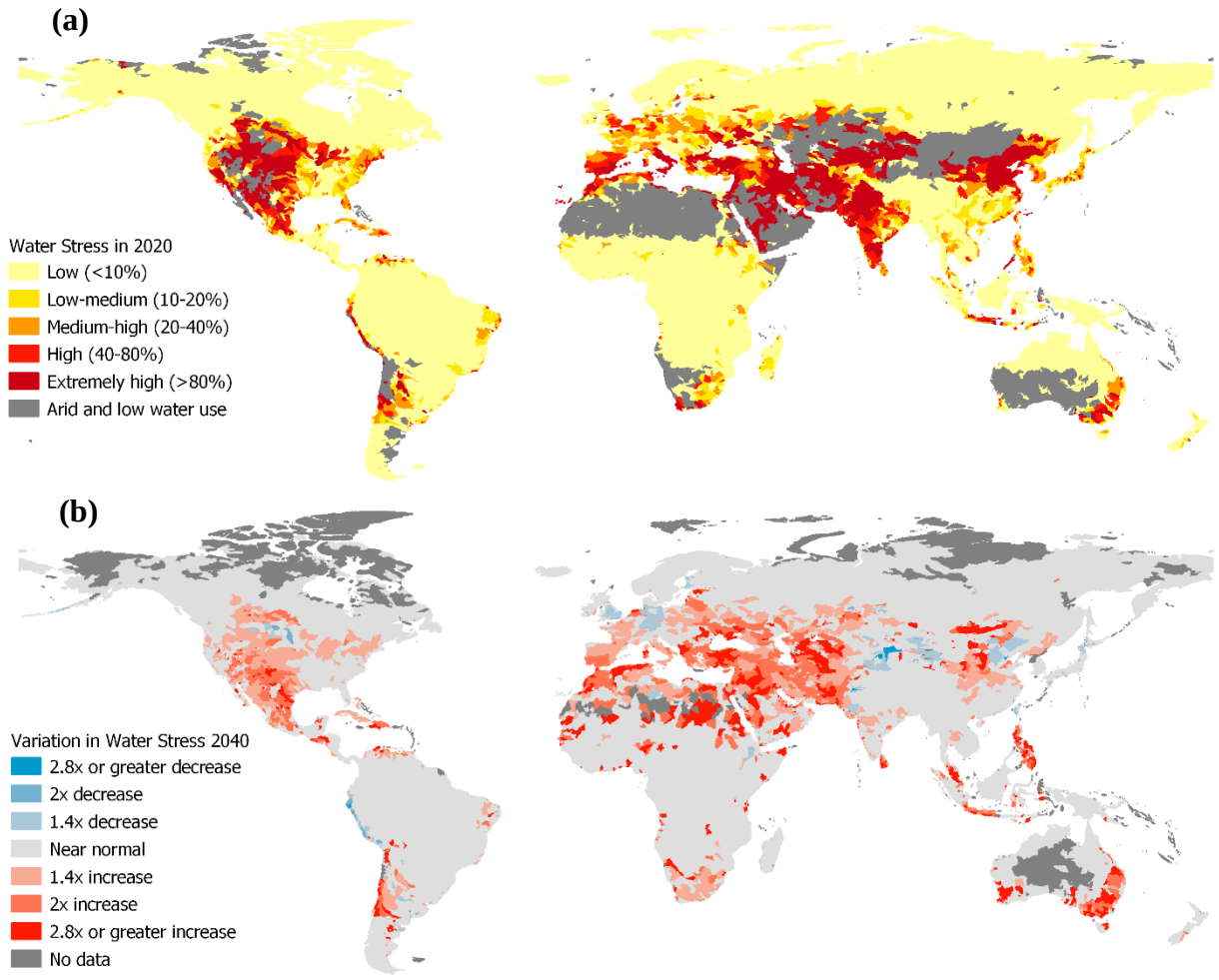

Figure 3. (a) World map of water stress in 2020, (b) Variation of water stress from 2020 to 2040 [239]

1.2 Problematic

Confronted to this reality, there is a need to find solutions to alleviate this water crisis. Currently, the majority of drinking water is provided by freshwater sources (rivers, aquifers, etc.) [11].

However, with their depletion, saltwater treatment has become a new high potential source of freshwater. Desalination has rapidly become the major technology to perform this treatment [12]–[16]. Table 1 shows the total desalination capacities by region and by income level:

Table 1. Desalination Capacity by region and income level [15]

		Number of desalination plants	**Desalination Capacity**	
			(million m^3/day)	*(%)*
Global		15 906	95.37	100
	Geographic Region			
	Middle East and North Africa	4 826	45.32	47.5
	East Asia and Pacific	3 505	17.52	18.4
	North America	2 341	11.34	11.9
	Western Europe	2 337	8.75	9.2
	Latin America and Caribbean	1 373	5.46	5.7
	Southern Asia	655	2.94	3.1
	Eastern Europe and Central Asia	566	2.26	2.4
	Sub-Saharan Africa	303	1.78	1.9
	Income Level			
	High	10 684	67.24	70.5
	Upper Middle	3 075	19.16	20.1
	Lower Middle	2 056	8.88	9.3
	Lower	53	0.04	0.0

This method consists in treating surface and ground brine water by removing the dissolved minerals inside of it [12], [13], [15]–[17]. There are several technologies capable of achieving this goal. These can be divided into two categories: thermal-based (i.e. multi-stage flash distillation, multi-effect distillation, solar evaporation etc.) and membrane-based (i.e. reverse osmosis) [13]. Thermal methods employ thermal energy to evaporate water and to recondense it elsewhere, yielding clean freshwater and leaving behind the dissolved solids [13], [15], [17]. These technologies require a substantial amount of energy (4-150 kWh/m^3) to operate and become less viable at large scales simply due to this energetic implications [17], [18]. There are also limitations based on geography. For instance, thermal methods were traditionally employed in the Persian Gulf, where seawater was already at a relatively high temperature when compared to other bodies of water around the world [17]. Membrane methods, specifically reverse osmosis (RO), on the other hand, has rapidly

become the leading technology for freshwater generation. Water is pumped through semi-permeable membranes at high pressures – between 0.2-8.3 MPa depending on the quality of water fed – that overcome osmotic pressure of the water [13], [15]–[17]. In this process, minerals and ions are removed [12], [16], [19]. The advantages of this technique are the simplicity of fabrication, operation and maintenance, the lower capital and operating cost compared to thermal methods, the ambient conditions (temperature), modularity and flexibility due to compact nature of reverse osmosis filters [17]. While it is now the most employed technology for providing freshwater at large scales, it consumes a large quantity of energy because of the high-pressure pumping required for its functioning. This energy consumption ranges between 2-9 kWh, depending on the plant capacity [12], [17], [18], [20]. Globally, reverse osmosis consumes 75 terawatt hours of electricity, 99% of which is derived from fossil fuels [14]. This technology has become more cost effective in the past decade with an operating cost between of US$ 0.20-1.72 per m^3 of water depending on the plant size and the quality of the water fed to it (seawater, brackish etc.) [18]. However, this process requires the availability of large bodies of saline water as feedstock and high amounts of cheap electrical power. For inland or noncoastal regions, this can be cost prohibitive due to high capital investment and operational costs [17]–[19]. This stems from the need to construct and operate larger pipelines that bring saltwater from source to RO plant.

Therefore, considering the state of water scarcity and the future that is facing us under business-as-usual conditions, it is necessary to look elsewhere for sustainable sources and methods for generating freshwater. Turning to nature for solutions can prove beneficial as several species of plants and animals have developed, over the course of millennia, fascinating methods to efficiently collect water for their survival in all climatic conditions (arid, semi-arid, humid, costal etc.). From this assessment, fog harvesting has been found to be a promising way to generate enough freshwater for basic needs and that, in a scalable, low impact manner.

1.3 Definitions and Base Concepts

Fog is a body of airborne or atmospheric water consisting of **liquid** microdroplets between 1 and several 10s of micrometers [21]–[23]. Clouds are similar in composition, however they are distinguished by their altitudes. Fog is found at lower altitude and clouds at higher ones. Fog can be visualized as a stable suspension of water microdroplets in air [21], [24], [25]. It is formed when

the air temperature and dew point are equal, and water molecules condense onto a site through heterogeneous nucleation. Similarly, mist is also a stable suspension of water droplets in a parcel of air but differs in its definition. Meteorology distinguishes fog from mist based on their ability to reduce visibility. The former hinders visibility farther than 1 kilometer and the latter, below this threshold [25]. The **mixing ratio** is a ratio of the mass of vapour to dry air [24].

Fog harvesting is then the process of capturing water contained in fog on a given surface through impaction, growth, coalescence and collection [22], [23], [34]–[37], [26]–[33]. The performance of this process can be described through normalized values: capture percentage and collection rate. Capture percentage expresses the total fraction of water removed from the original mass of fog flow by effectively collecting it (%). Collection rate is a value for the rate of this collection, expressed as the mass of water captured per unit area per unit time (g/cm^2h) [38]. A fog harvesting surface, namely a fog harvester or fog collection surface is the substrate used to perform this action. It is generally differentiated through geometric, topological and chemical surface properties [22], [23], [29], [34]–[36]. Figure 4 presents several examples of fog harvesting materials. Geometrical aspects of a fog harvesting surface encompasses the shape, orientation and constituents (wires, plates, etc.). Topological properties include micrometric or nanometric structuring at the surface. Chemical surface properties include the ways in which the fog harvester interacts with water upon contact.

Figure 4. Fog harvesting materials: Raschel mesh (left), stainless steel mesh knitted with poly-yarn material (middle) and 3-D poly material net (right) [23]

Surface functionalization is a method to change the surface properties of a material by addition of chemical functional groups [39]. It is a physico-chemical surface modification intended to bestow properties of interest for intended interactions of a material with its surrounding matrix [39]–[41]. A **functional group** is a set of atoms that possess specific properties and can perform distinctive reactions regardless of the molecules it is attached to. Examples of functional groups are alkanes (-$(CH_2)_n$-H), phenyls (-C_6H_5), amines (-NH_2), alcohols (-OH), ethers(-OR), thiols (-SH), ketone (-COR), carboxyls (-COOH). Functionalization can be done physically or chemically. Physical functionalization such as wrapping, or surfactant treatments usually lead to noncovalent bonding between functional groups and the surface. Chemical functionalization, on the other hand, is often achieved through vapor deposition processes (including plasma), polymer grafting or amidation, esterification, thiolation reactions, yield covalently bonded structures.

A **hydrophobic** surface is one that has a poor affinity with water and thus is not attracted to it. It consists of nonpolar or nonionic molecules that have a preference for nonaqueous environments [42]–[45]. Hydrophobicity is then a measure of the degree of this preference. A surface that has a low degree of interactions with water molecules is said to have low wettability as it does not allow itself to become wet [43], [45]. Water will therefore form a spherical droplet to minimize its surface free energy because it is more attracted to itself and thus reduces the interfacial surface area shared with the hydrophobic material [45]. It can be assessed through contact angle measurements with water droplets. For a surface to be considered hydrophobic, its contact angle with water must be over 90° [45]–[50]. This value, however, is purely mathematical and by taking into account physico-chemical interactions such as the interactions between water and the substrate, namely long range attraction forces, the threshold is located at 65° [51], [52]. This concept was first introduced by Berg et al. in 1994 who measured surface forces on thin films containing carboxylic acid with increasing amounts of diacid, effectively incorporating oxygenated groups and increasing hydrophilicity [51]. They found that long range hydrophobic attraction forces were still measurable at 90° (25% diacid) contact angle and these forces were no longer observed at 65° (50% diacid). Similar results have been found in several other research works in the literature [52]. The technical

aspects of this measurement and definition is further discussed in Chapter 3. Figure 5 shows a schematic of how hydrophobic surfaces interact with water.

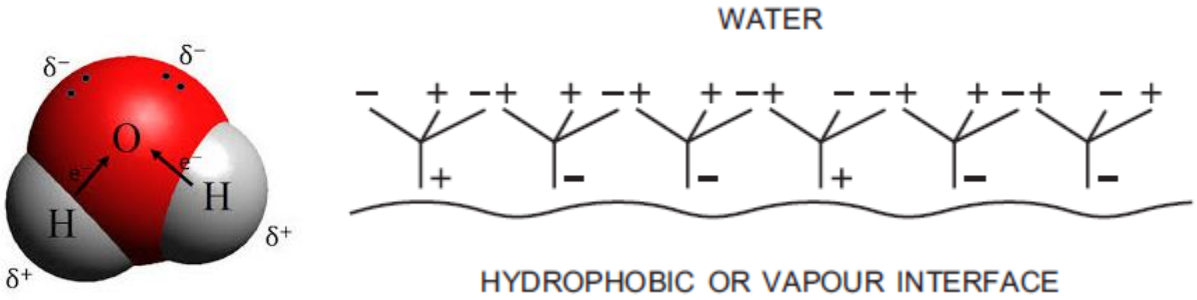

Figure 5. (a) Charges (δ) on a water molecule (b) Water molecules interactions with hydrophobic surfaces [44], [240]

Inversely, a **hydrophilic surface** has high affinity with water molecules and is typically polar [44], [53], [54]. This implies that upon contact, water will spread along the surface to minimize the surface energy of the system [50], [53], [55]. It will favor hydrogen bonding with water molecules, as shown in Figure 6 [44].

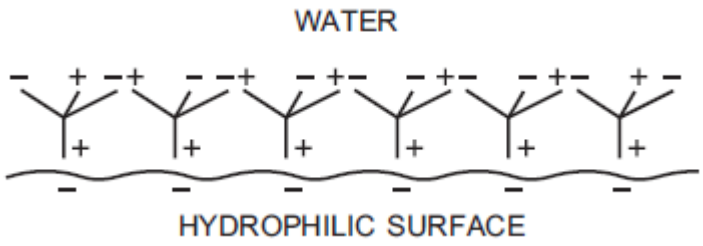

Figure 6. Water molecules interactions with hydrophilic surfaces [44]

1.4 Main Objectives for the Research Project

In this research project, we attempted to address water scarcity concerns through the development of an efficient fog harvester. Through the exploration of past advances in the field, several limitations were brought to the forefront. This led to a thorough investigation into the effects of a multitude of design parameters for fog harvesting such as material selection, geometry and surface chemistry. In the course of this study, we addressed several issues with experimental systems such

as fog simulation, droplet impaction and the growth onto a surface of functionalized films through photo-initiated chemical vapor deposition (PICVD). One important concern with regards to the functional films in the water harvesting application was the stability of the PICVD coatings. This stability issue became a key focus in the project, leading us to develop a surface functionalization strategy for improving stability in thin film coatings generated by PICVD. Ultimately, after having performed an assessment on design criteria for fog harvesting, scalability of our proposed system was evaluated through the construction of a large-scale device.

1.5 Master's Thesis Plan

This memoir is organised in 7 chapters to allow for a complete understanding of the work achieved throughout this research project. First, a general introduction giving the context in which the work is situated was given in Chapter 1. Then, core concepts are further developed in the literature review in Chapter 2. This section covers the macroscopic elements involved in the project such as the physics of fog generation and a detailed review of fog harvesting technology. We then describe how microscopic elements, namely surface science, can intervene in the fog harvesting process. This leads to a split between two types of surface interactions with fog: physical and chemical. Thus, surface topology is introduced and explained followed by surface chemistry, these being related to the main subject of fog harvesting. Upon elaborating the theoretical aspects, state of the art and current limitations in the field, Chapter 3 lays out the specific objectives that aim to address these holes in the literature. The methodological elements, especially characterization technique, used through the research project are also described in detail. Chapter 4 presents a summary of the fog harvesting experiments and important results as well as preliminary discussion points in response to them. One important element that was studied and presented in this chapter was surface chemistry. Specifically, the stability of PICVD treatment was found to be poor. This was further investigated, and the results of this study is presented in Chapter 5 (in the form of a manuscript submitted for publication). Chapter 6 then presents additional results and analysis of the fog harvesting experiments. It also lists the major limitations of the work presented after rigorous hindsight evaluation and proposes solutions to address these drawbacks. Finally, Chapter 7 concludes this memoir through a summary of the work done in this master's project and offers orientation for any future researcher interested in continuing this project.

CHAPTER 2 LITTERATURE REVIEW

2.1 Water Capture: Fog Harvesting

2.1.1 Fog Formation and Composition

Fog is created when air becomes supersaturated with water, and eventually condenses on nuclei upon cooling, forming microdroplets or ice crystals in a stable suspension in air [21], [24], [25], [56]–[59]. Supersaturation can be expressed as a function of the saturation ratio S. This is synonymous with relative humidity (RH) and can be expressed as the ratio of water vapour pressure to saturation vapor pressure at a given temperature:

$$S = \frac{p_{water}}{p_{sat}} \quad (1)$$

When $S < 1$, air is subsaturated. Then, saturation occurs when $S = 1$ [60]. Finally, for values above 1, supersaturated conditions are achieved. To achieve supersaturation, three different pathways are available depending on environmental conditions: isobaric cooling of air, adiabatic cooling of air or addition of water vapour into the air through mixing [21], [57], [59], [60]. Fog formation through isobaric cooling can occur when air temperature decreases, causing p_{sat} to decrease also [59], [60]. However, p_{water} remains constant, effectively increasing the saturation ratio towards 1 and beyond. Thus, once this point is reached, saturated water vapour is pushed beyond equilibrium and droplets begin to condense. Direct cooling is possible through advection or radiation. Advection fog occurs when water laden air passes over a cooled surface, sufficiently lowering its temperature to induce condensation through heat transfer between the surface and air [57], [59]–[61]. For radiation fog, air cooling is the result of an imbalance between absorbed and emitted longwave radiation from the earth surface leading to a higher amount of radiation leaving the surface and, ultimately, cooling the surface and the air close to it below the dew point [57], [59]–[61]. This type of radiative cooling typically occurs overnight.

Upslope fog happens when moist air is cooled by flowing over surface elevations due to topological changes (hills, mountains, etc.) [60], [61]. In this case, decrease in air temperature occurs through expansion as pressure drops at higher altitudes. The low velocity of this air movement leads to a process that occurs at constant energy (adiabatic). All the parameters of Eq. 1 are decreasing

simultaneously. Supersaturation can be achieved due to the fact that p_{sat} decreases at a quicker rate than p_{water} [60]. Another way of producing fog is by adding water vapour to cold air through mixing. Two air parcels are added together, and their properties are added proportionally to the number of moles present in each parcel such that:

$$p_{water} = \frac{N_1}{N_1 + N_2} p_{water,1} + \frac{N_2}{N_1 + N_2} p_{water,2} \quad (2)$$

$$T = \frac{N_1}{N_1 + N_2} T_1 + \frac{N_2}{N_1 + N_2} T_2 \quad (3)$$

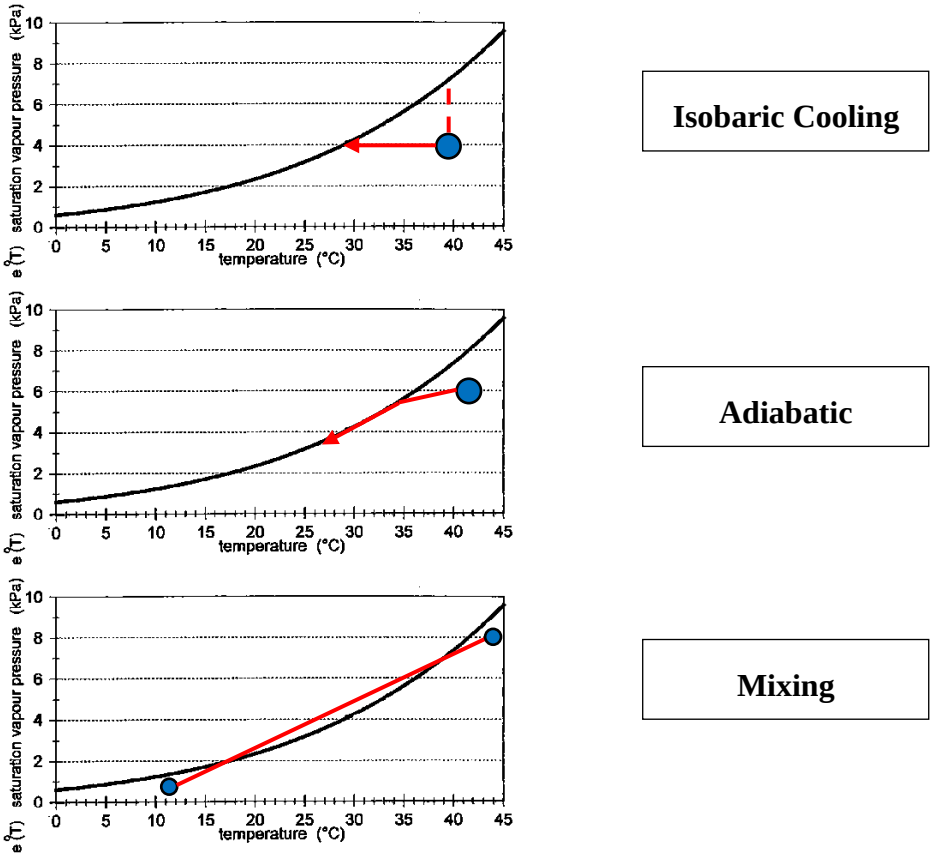

Figure 7. Evolution of the saturation water pressure with temperature. Summary of fog formation mechanism showing the thermodynamic pathways (red line) for fog formation. The blue dots represent thermodynamic states of water vapor prior to fog formation

In all cases, formation of fog droplets can be achieved if the properties lie above the saturation line. For all three mechanisms (Figure 7) to create fog, it is necessary for air to contain particulate matter on which water can nucleate [21], [57]–[61].

2.2 Surface Properties

When a liquid is brought to contact with a solid surface, capillary forces induce the movement of the liquid contact line at the interface [45], [53], [55], [62]. In the case where this contact line motion leads to spreading of liquid along the surface, forming a film, then the liquid has attractive interactions with the solid and is said to be hydrophilic [44], [55], [62], [63]. In the opposite case, the liquid retracts itself, forming a finite contact angle and the surface is said to be hydrophobic [63]. These possible outcomes are dependent on both the liquid and solid intrinsic properties. The contact angle (θ) at the solid-liquid interface is widely considered to be the determining factor for attributing such qualifiers to a surface [45], [48], [55], [62]–[65]. Thomas Young, the father of contact angle theory, first described the notion of surface wettability in 1804 [48], [52], [66]. He theorized that wettability could be quantified from the tangential angle at the interface of all three phases (liquid-solid-air) through the following relationship for a flat surface:

$$\gamma_{sv} = \gamma_{lv} cos\theta + \gamma_{sl} \quad (4)$$

Where γ_{sv}, γ_{lv} and γ_{sl} are the solid-vapor, liquid-vapor and solid-liquid surface tensions [67]. These surface tensions represent the free energies at the interfaces per unit surface area. Young also derived a relationship to quantitatively express the work of adhesion, W_a, of a liquid:

$$W_a = \gamma_{lv}(1 + cos\theta) \quad (5)$$

This represents the work required to separate the liquid and solid phases [49]. This equation was particularly interesting as it defines the adhesion work as a function of measurable quantities whereas γ_{sv} and γ_{sl} were difficult to measure.

Surface tension itself is defined as the work needed to increase the surface area of the liquid isothermally and reversibly by one unit [62]. A liquid is held together by the sum of attractive forces that are at equilibrium with other surrounding forces [45], [46], [48], [50], [66], [68]. The molecules found at the liquid interface with another phase experience a competition between cohesive forces, that pull them towards the bulk of the liquid, and adhesive forces that pulls them

outwards [50]. When molecules are found in the bulk, the cohesive forces are balanced as it is surrounded by like molecules. These forces may be van der Waals forces or hydrogen bonding for example [44], [55]. However, at the interface, they are surrounded by both internal, identical molecules and external, foreign molecules [62]. This causes them to lose cohesive interactions. If there is poor chemical affinity with the foreign molecules, interactions are reduced, and the resultant force will be directed inward (Fig. 8). Here we can better visualize that the energy required to overcome this cohesive resultant corresponds to the surface tension. With this view, a decrease in surface tension corresponds to a decrease in cohesive forces and increases spreading along a surface.

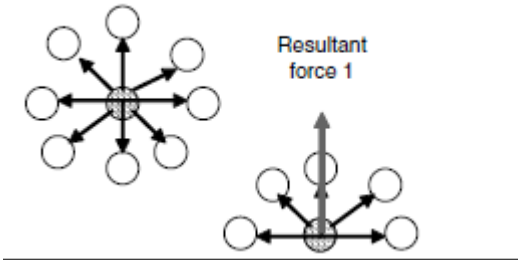

Figure 8. Cohesive forces within the bulk of a liquid and at the bi-phasic interface

Other than surface tension forces acting on a drop, capillary pressure – the differential pressure between the inside of the drop and outside – also acts upon droplet shape [48], [69]. The geometry of the droplet at an interface can be described through Young-Laplace equation which relates a droplet's radii of curvature to the capillary. This relationship provides insight into prediction and analysis of drop shape, contact angle and surface tension. This equation is presented below:

$$\Delta P = \gamma_{lv}\left(\frac{1}{R_1}+\frac{1}{R_2}\right) \quad (6)$$

Where ΔP, R_1 and R_2 are the capillary pressure and the principal radii of curvature at the interface. For a spherical droplet, $R_1 = R_2$ and thus, the Laplace pressure becomes $\Delta P = \frac{2\gamma_{lv}}{R}$. Before going any further, it is important to discuss contact angle hysteresis. Equation 6 is valid for a pure liquid on a flat, rigid and smooth surface. Similarly, θ defined by Young's equation assumes ideal conditions and does not adequately represents reality [70]. A droplet undergoes kinetic phenomena such as evaporation, swelling and adsorption of solution impurities as well as thermodynamic ones that are a result of surface properties like roughness and surface heterogeneity [45]. This leads to a

droplet having a range of static contact angles due to interactions at the three-phase boundary. When a volume of liquid advances onto a new, non-wetted surface area, an advancing contact angle is formed [45], [55], [66]. In the opposite case, a receding contact angle is formed. The difference between these two give the contact angle hysteresis. Generally, they are measured through dynamic methods where the substrate is tilted to induce the movement of a droplet along the surface [62], [64], [65]. This is particularly important in the case of water moving down a surface, like in fog harvesting, since it gives a more precise expression of the force balance between adhesion and gravity [38], [71]–[74]. Therefore, the criterion for a droplet to run down a surface, gravity must overcome adhesion:

$$F_{adhesion} < F_g \quad (7)$$

Several studies have defined the adhesion force on meshes and wires [31], [33].

$$\pi r\gamma\left(cos\theta_{receding} - cos\theta_{advancing}\right) < \rho V g sin\alpha \quad (8)$$

Where r, $\theta_{receding}$, $\theta_{advancing}$ and α are the wire radius, receding and advancing contact angles and the inclination angle respectively.

2.2.1 Surface Free Energy and Work of Adhesion

Surface free energy is the energy required to form a new unit of interfacial surface area [50], [55], [64], [68]. This science relies on attractive forces between molecules of a phase with others. As mentioned in the previous section, attraction forces of molecules of a liquid can be divided into two distinct categories: cohesive and adhesive [45], [55], [62], [75]. Cohesive force corresponds to the attraction of molecules composing a liquid amongst themselves. These interactions are what keep the molecules in the bulk of the liquid. Adhesion, in turn, is the attractive force of liquid molecule with other, adjacent phases. Thus, molecules found at a phase boundary, liquid-solid or liquid-vapor, will experience both a pull inward and outward. Once equilibrium has been reached in this force balance, the liquid will hold its shape, a droplet for instance, with a fixed interfacial area. Hence, surface free energy corresponds to the balance of the loss of cohesive force needed to increase this interfacial area. When a droplet increases the interfacial area, spreading along the wetted surface occurs. This spreading stops once the surface free energy is maximized. A spherical geometry is therefore prioritized for liquid drops because this shape has the lowest ratio of surface

area to volume. Generally, surface free energy is calculated with Young's equation (equation 4). This relationship assumes an ideal surface with a chemically homogeneous, a smooth (atomically flat) surface and that the system is in equilibrium. This is an oversimplification for real surfaces that are more often than not, heterogeneous and rough. Other models for wetting have been derived for non-ideal surfaces such as Wenzel and Cassie-Baxter states [52], [65], [70], [76], [77]. In the former, a liquid drop wets the surface between surface rugosity such that the liquid impregnates the totality of the solid surface. In the latter, droplets sit atop of trapped air bubbles located between surface irregularities. These wetting states are schematised in Figure 9.

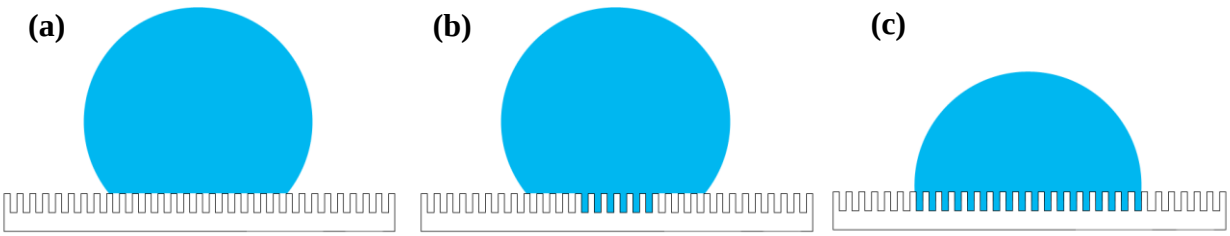

Figure 9. (a) Cassie-Baxter wetting, (b) transition state and (c) Wenzel state

For CNT forests, it has been found that wetting exhibits a metastable state that shifts from a Cassie-Baxter with a slow infiltration into the dense forest and adhesion on the CNTs corresponding to a Wenzel state [78]. This transition is highly dependent on the CNT forest density and atmospheric conditions. It has been found that for high density (>1x10^{10} CNTs/cm^2), water droplets are stable for over 25 minutes at room temperature and atmospheric pressure. However, this stability is further increased when stored in a saturated environment, highlighting the importance of evaporation in the stability. In the case of this research project, Cassie-Baxter wetting is considered. Hence, Young's equation is modified towards Cassie-Baxter's equation:

$$cos\theta_{CB} = fcos\theta + f - 1 \quad (9)$$

Where f is the area fraction of solid-liquid contact and is equal to approximately 0.038 for untreated CNT forests. Once CNTs are hydrophilically treated, it is assumed that f is equal to 1 due to full wetting of the CNT walls, and thus, $\theta_{CB}=\theta$.

2.3 Nucleation Theory

Water vapour will condense onto an airborne particle through nucleation. Historically, it was believed that dust and soot served this role [58], [79]. This was further expanded to include hygroscopic materials due to their efficiency to attract water molecules. Materials such as salt (NaCl) and secondary particles like volatile organic compounds may also serve as nucleation sites [24], [25], [59]–[61]. For instance, sulfur oxides (SO_x) that react with atmospheric compounds like OH, effectively oxidizing them and forming nuclei such as H_2SO_4 [60]. Generally, nuclei can be generated through condensation and deposition of vapours from smokestacks, mechanical dispersion of physical material or by particle agglomeration in the atmosphere [24], [25]. This is done through nucleation, a process that describes the transition from a high free energy thermodynamic phase to an organized and structured new, low free energy, one [80]–[82]. When a new phase is created from an older one, we can visualize an infinitesimal amount of the newer phase (liquid or solid) suddenly appears within the bulk with thermodynamic properties that differ significantly from its mother phase [80], [81]. This corresponds to a first-order phase transition [80]. The process of nucleation is in fact a first-order transition. Examples of this phenomenon can be observed in fundamental natural processes such as cloud and rain formation, volcanic eruptions, earthquakes etc [59], [60]. Many attempts to accurately model this transition, including the many factors that influence it, have been developed [80]–[82]. Some models set their roots in macroscopic properties such as cluster radius and surface tension for instance, while others are founded in kinetic, molecular properties and interactions, usually derived from first principles [81]. From these, Classical Nucleation Theory was the first model that attempts to describing nucleation behaviour and rates phenomenologically [81]. It should be noted that Classical Nucleation Theory is the basis for understanding and modelling phase transition phenomena. It assumes that the free energy ΔG can be approximated as the sum of a bulk and interfacial terms that are representative of the volume and surface area of the newly formed nucleus [81]. Classical nucleation theory also assumes a spherical nucleus that possesses a clear boundary between itself and the surrounding phase [81]. This is a reductive model since macroscopic elements are considered when it is known that such properties do not apply at the molecular scale. However, it gives a clear idea of the nucleation phenomenon. It stipulates that the change in Gibbs free energy during initial spherical

cluster formation for phase transition from vapor to liquid is given by the following probabilistic equation:

$$\Delta G = -\frac{4\pi r_{cluster}^3}{3} k_b T ln S + 4\pi r^2 \sigma \quad (10)$$

$r_{cluster}: cluster\ radius$

$k_b: Boltzmann\ constant$

$T: Temperature$

$S: Saturation\ Ratio$

$\sigma: Surface\ specific\ energy$

This displays the competition between two terms on the right-hand side of the equation: the energy gain in the formation of a new bulk phase versus the energy cost at the interface between the new and old phase [80]–[82]. A cluster, or nucleus consists of a small grouping of new phase atoms or molecules. Upon inspection, it can be deduced that at high cluster radius r, the first term will increase at a higher rate than the second, reducing ΔG. Inversely, for small r, the second term, associated with the formation of a new surface, is dominant and ΔG increases. Therefore, there must be an intermediate value for cluster radius that maximizes the free energy. From this observation, a critical radius r^* and critical free energy ΔG* were defined. This can be visualized as the slow addition of molecules to a cluster. As it grows, it reaches a critical point beyond which nucleation can occur and a new phase will appear [80]–[83]. Figure 10 presents this phenomenon.

$$\frac{d\Delta G}{dr} = 0 \quad (11)$$

$$\Delta G^* = \frac{16\pi\sigma^3}{3(k_b T ln S)^2} \quad (12)$$

$$r^* = \frac{2\sigma}{k_b T ln S} \quad (13)$$

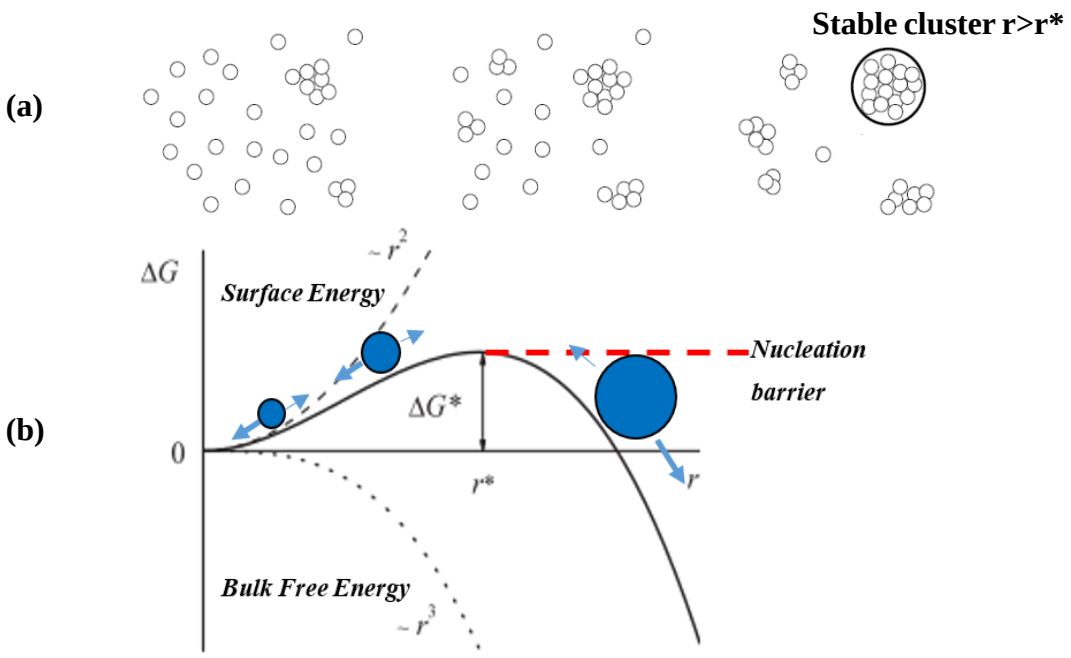

Figure 10. (a) Schematic of cluster formation and nucleation and (b) change in free energy as a function of cluster radius [80], [84]

Nucleation can be further separated into two distinct categories: homogeneous and heterogeneous [80]–[82]. In homogeneous nucleation, a stable phase is pushed towards a metastable through temperature variations. An important aspect in homogeneous nucleation is that the phase transition occurs without the presence of a foreign body or surface [80]–[82], [84], [85]. The main requirement to initiate spontaneous condensation or freezing is very high supersaturation levels in the order of several hundreds of percent [21]. Yet, in the atmosphere, supersaturation above 1% rarely occur [59]. Thus, homogeneous nucleation is much less likely to occur [21], [59]–[61].

Heterogeneous nucleation occurs at preferential sites situated on external surfaces like walls, cavities and particles to initiate phase transition [59], [60], [80]–[82], [85]. With the presence of a nucleation site, the free energy barrier is greatly reduced, and condensation can occur at lower supersaturation levels ($\Delta G^*_{hetero} << \Delta G^*_{homo}$). While the Gibbs theory for nucleation remains true, Volmer has developed an expression for heterogeneous nucleation that includes geometrical implications of condensation onto another solid [80], [81], [86], [87]. Assuming spherical geometries for nucleation, when a cluster is formed and reaches its critical point, it will condense as a cap whose shape will be dependent on the affinity of the surface with the newly formed phase

[81], [86], [87]. Thus, in heterogeneous nucleation there is a dependency on contact angle (θ). The critical free energy becomes:

$$\Delta G^*_{hetero} = \Delta G^*_{homo} f(\theta) \quad (14)$$

$$f(\theta) = \frac{2 - 3\cos\theta + \cos^3\theta}{4} \quad (15)$$

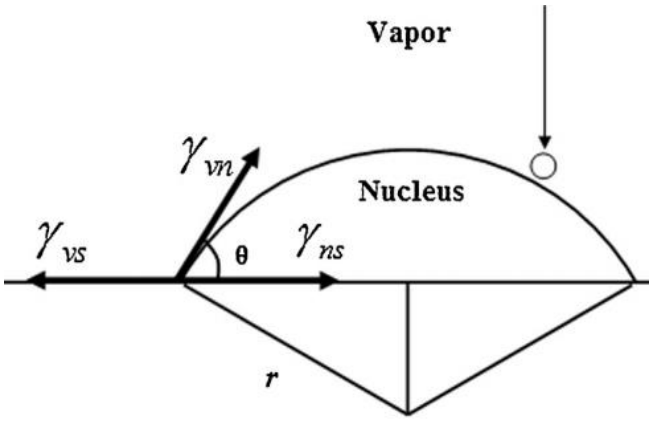

Figure 11. Heterogeneous nucleation spherical cap formation [88]

Where γ_{vs}, γ_{vn} and γ_{ns} are the vapor-solid, vapor-nucleus and nucleus-solid interfacial tensions. By inspection, it can be seen that from equation 15, surfaces that possess low contact angles (i.e.: hydrophilic) lower the energy barrier for nucleation [60]. Therefore, hygroscopic aerosols are preferred nucleation sites for condensation in the atmosphere [24], [25], [59]–[61]. Heterogeneous nucleation involving airborne particles is most often responsible for cloud and fog formation.

2.4 Fog Harvesting

2.4.1 State of the Art

Looking at the various sources of available freshwater, removal of airborne water largely has been under-explored when compared to conventional water generation techniques. Water present in the atmosphere accounts for 0.001% of the total amount available on the planet or approximately 13000 km^3 [3]. It can appear under its gaseous (vapour) or condensed (clouds, mist and fog) form. Collecting such freshwater is therefore categorised into two distinctly different families: atmospheric water generation (AWG) and fog harvesting [23], [29], [35], [89], [90]. The former

focuses on capturing atmospheric water that is found under its gaseous (vapour) phase corresponding to humidity [89], [90]. This process involves capturing moisture onto a surface, condensing it into liquid water, separating and treating it for consumption. Currently, AWG technologies that are under research and development rely mainly on passive radiative condensers or sorption-based materials [89]–[91]. Thermodynamic approaches rely on cooling humid air below its dew point to condense water onto a cooled surface, collect and clean water. These techniques have slowly become the most used technique in the AWG industry, but the main limitation lies in its high energy consumption. On the other hand, considerable on-going research is being done on adsorption-based techniques. These techniques use desiccant hygroscopic materials that allow for water vapour adsorption within the material. Once the material is saturated, water is removed by heating it, releasing the water vapour that is then recondensed for treatment and consumption. As an example, a collaboration between the Massachussetts Institute of Technology and the University of California-Berkeley has led to the development of a metal-organic framework (MOF), designed to capture dew in arid climates (10-40% relative humidity) at rates of 0.25 liters per kg of MOF [92], [93]. The main limits for commercialisation for AWG technologies lies in the energy, performance and cost efficiency of the designed system [90]. To capture dew, there are several thermodynamic barriers to overcome namely, water condensation and removal from the system which is intimately linked with nucleation theory explained previously [29], [36], [37], [89], [90], [94]. Hence, AWG systems must find ways to pay this cost with a minimum input of external energy. Using locally available renewable sources of energy such as solar power has often been hypothesized for such needs [89], [90], [92]. Finally, water output must be maximized for a wide range of conditions. That being said, AWG is out of the scope of the work presented in this thesis and will not be further discussed.

Even though fog requires specific atmospheric conditions for its viability, compared to moisture, the field remains interesting when comparing yields. In fact, annual dew frequency has been estimated to 48.8% compared to 5.5% for fog, making the former much more attractive in terms of potential [29]. This is highly dependent on geographical factors such as climate and topology [22], [35]. Nevertheless, in appropriate scenarios, fog capture rates are typically between 1.5-12 L m^{-2} per day whereas AWG has shown, to this day, yields between 0.3-2.5 L m^{-2} of collector area per day [90]. As for energy consumption, the lowest values reported was of 2 kWh kg^{-1} [90]. This

aspect highlights the need for appropriate project planning in terms of technological selection and design based on the designated location.

Fog harvesting focuses on capturing the remaining available water in the atmosphere. The distinguishing factor, again, is that water is already present in the liquid phase as 1-50μL droplets [22], [24], [35], [95]. Thus, already-condensed water is collected through impaction onto a material - droplets adhere to the surface, accumulate and grow via coalescence to a critical size before they run down the surface [22], [23], [96], [29], [30], [34]–[36], [90], [94], [95]. Once collected, water can be further treated depending on its composition. Fog harvesting, therefore, consists in a low-cost, sustainable and passive technique for collecting freshwater in regions where fog is present.

Collecting water from fog is not a novelty. Early documentation of fog and dew harvesting can be traced back to the Modern Era in the XVth century in the Canary Islands with the Garoé tree (Figure 12) [97]–[99]. This tree has been the source of many legends and intrigue since its discovery and has adopted many names such as the weeping tree, distillery tree and even the magic rain tree amongst others [98]. We now understand that this tree is one of nature's examples of fog harvesters, effectively supplying water to entire villages [98]. The fog is generated from warm wind passing over the Canary cold current, cooling the air and creating advection fog at the coast of the island. In other cases, structures were constructed to capture fog such as cisterns beneath trees in the

mountains of Oman or piling stones that cooled overnight to collect dew and fog water in the Atacama Desert [23], [35], [99].

Figure 12. Drawings of the fog harvesting Garoe tree [97], [98]

Despite these ancestral techniques, the development of modern fog harvesters began in the mid-XXth century [99]. Since, a substantial number of projects have been initiated world-wide located primarily in mountainous or coastal regions [21]–[23], [95], [99]. Figure 13 shows a map describing areas that are prone to abundant fog superposed with ongoing projects [29].

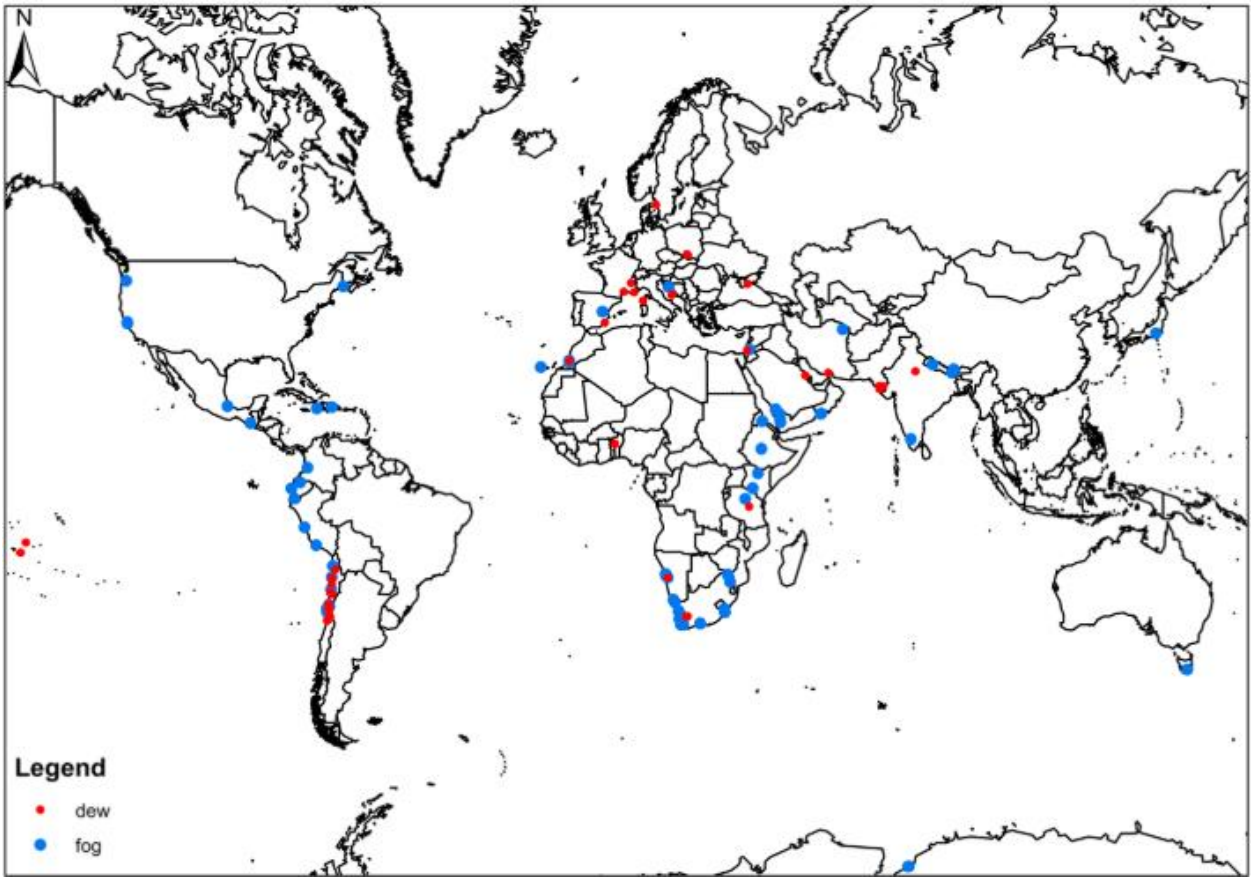

Figure 13. Map of fog and dew harvesting projects [29]

As mentioned previously, these devices can take many forms. It is in 1994 that Robert Schemenauer and Pilar Cereceda proposed a design for Standard Fog Collectors (SFC) consisting in a food-grade polypropylene (PP) mesh, manufactured in Chile under the name of Raschel nets [100]. These are stretched along a 1m by 1m metal frame and elevated at a height of 2m above the ground. Beneath the mesh, a gutter is attached to collect the water. SFCs have since been used to evaluate fog harvesting potential in studies for fog harvesting projects. SFCs have average collection rates between 1-10 L m^{-2} per day. This is highly dependent on fog conditions such as windspeed, fog density, liquid water content (LWC) and the size of the microdroplets [21], [23], [29], [34], [90]. In optimal conditions, these rates can increase to 30-40 L m^{-2} per day [22], [23], [35]. This design was further scaled-up into a 4m x 10m Large Fog Collector (LFC) [23], [29], [35], [99]. On the Pacific coast of South America, projects in Chile, Peru and Ecuador were shown to collect between 6-12 L m^{-2} per day providing water for small villages as well as afforestation [23]. In the Guatemalan village of Tojquia, located 3300 m above the mean sea level, 35 LFCs

were installed in 2006, capturing approximately 6300 liters of water per day [23]. This example also illustrates social pressure alleviation because prior to the installation of these LFCs, women and children were tasked with gathering water from sources located far from the village (usually in the valley at the base of the mountain) [23], [29], [35], [99]. A non-exhaustive list of fog harvesting projects world-wide is presented in the following table:

Table 2. Summary of fog harvesting projects using standard fog collectors (SFC) and large fog collectors (LFC)

Site	**Material**	**Surface (m^2)**	**Yield (L m^{-2} / day)**
Alto Patache (Chile)	SFC	2	6
Tojquia (Guatemala)	35 LFCs	~1400	4.5
Yemen (in mountainous region)	25 LFCs	~1000	4.5
South Africa (various projects)	SFCs	-	1-10
Oman	-	-	30
Bica da Cana (Portugal)	SFC	2	8.2
Chao das Feiteiras (Portugal)	SFC	2	2.9
Topnaar Villages (Namib Desert)	14 SFCs	~28	0.096-1
Cape Verde	SFC	-	3-75
Lepelfontein (South Africa)	SFC	-	4.5
Coimbatore	SFC	-	7.7
Mount Velebit (Croatia)	SFC	2	4
Mount Machos (Spain)	LFC	40	3.3

The SFC and LFC are examples of two-dimensional technologies. There exist structures that are 3 dimensional that are designed to increase the collection efficiency. An example of this is the “Eiffel Collector” that is made with 2 layers of Raschel meshes and collects ten times more water than its single layer counterpart [22], [23], [35], [99], [101].

A drawback lies in the simplicity of Raschel meshes. Granted, their design was purposed for ease of use and installation, however, fog harvesting can greatly benefit from research aimed to improve their collection yield. Many advances in the fields of surface science and biomimicry have been put to use to improve the state of fog harvesting technology [29], [89]. The Stenocara beetle,

surviving in the Namib Desert, has often been used as a source of inspiration for surface design in fog and dew harvesting applications [28], [36], [73], [76], [102], [103]. This beetle is capable of efficiently collecting incoming fog onto their exoskeleton, possessing several 0.5 mm diameter microbumps. Parker et al. had hypothesized that this enhanced fog harvesting capacity was due to a wettability pattern by which water was captured on the hydrophilic microbumps and coalesced across the waxy, hydrophobic surface of the beetle's back. The water would then be carried, overcoming gravity, towards the insect's mouth. This hypothesis has since been revisited by the original author as no conclusive proof of a contrasting hydrophilic-hydrophobic exoskeleton was found, leaving this phenomenon unresolved [36]. Despite this oversight, several research groups have developed such enhanced surface.

Bai et al. have designed surfaces with a variety of wettability patterns [104]. Starting with a glass, hydrophilic substrate, they spin coated a slurry of titanium dioxide (TiO_2) which was then treated with heptadecafluorodecyl-trimethoxysilane (FAS) through chemical vapor deposition (CVD), rendering the surface superhydrophobic. Finally, the samples were placed under UV lamps emitting at 365 nm with an irradiance of 25mW/cm^2 to remove the FAS coating selectively by using photomasks. Several shapes were explored with this methodology like circle and n-pointed star shapes (n=1-8). A schematic of these shapes is shown below in Figure 14.

Figure 14. Wettability patterns explored by Bai et al.

It was found that asymmetric shapes (stars), lead to asymmetric wetting and droplet movement from the points towards the center. This is due to Laplace pressure gradients induced by the change in geometry. In fact, a single water drop located at the point of the star has a different, higher contact angle than the portion located in towards the hydrophilic center. This causes a force that drives motion of the droplet inwards. The highest water collection rate achieved was with the 5-pointed star with a value of approximately 2.7g/cm^2-h. Further insight into the forces involved in the droplet transport through pressure gradients was also provided by Deng et al. [105] They designed a surface with both a wettable gradient and Laplace pressure on a high adhesion surface. Figure 15 shows this material:

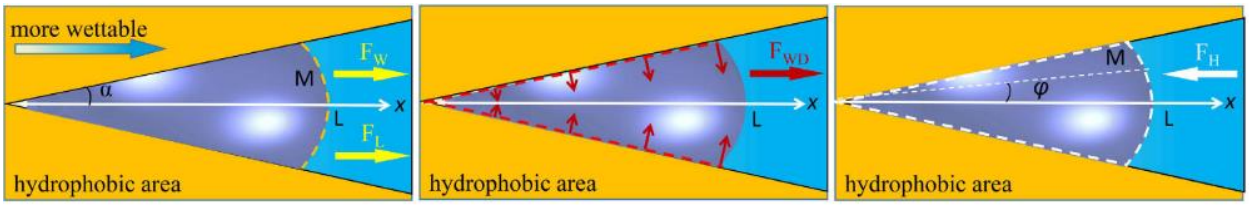

Figure 15. Wettability and Laplace Gradient surface designed by Deng et al [105]

These forces pushing the motion forward are the wettable gradient force (F_{wg}), Laplace pressure force (F_L) and the wettable different force (F_{wd}). Inversely, the force acting against the movement is the force of adhesion through hysteresis (F_a). These are defined as follows:

$$F_{wg} = \alpha\gamma L^2 k sin\theta_{philic} \quad (16)$$

where α is the half angle of the star point, γ is the liquid surface tension, L is the length that the droplet extends into the hydrophilic region, *k* is the gradient variation (degrees per unit length) and θ_{philic} is the contact angle in the hydrophilic region. The Laplace gradient can be calculated from the previously mentioned Young-Laplace equation and has been described by Ghosh et al. Locally, Laplace pressure for a sphere can be estimated as:

$$\Delta P_{local} \sim \frac{\gamma_{lv}}{r(x)} \quad (17)$$

where r(x) representes the local curvature and can be expressed as:

$$r(x) \approx \frac{\delta(x)}{2\sin\theta(x)} \quad (18)$$

Thus, the Laplace pressure gradient along the axis of movement is expressed as:

$$\frac{dP}{dx} \approx -\frac{d\gamma_{lv}}{r(x)dx} \approx -\gamma_{lv}\frac{d}{d\delta(x)}\left(\frac{2sin\theta(x)}{\delta(x)}\right)\frac{d\delta(x)}{dx} \sim 2\gamma_{lv}sin\theta\frac{1}{\delta(x)}\alpha \quad (19)$$

Where $\delta(x)$ represents the width of the hydrophilic region upon which the droplet is situated [106]. This equation shows that the pressure gradient is proportional to the half-angle of the wedge (α) and it describes the driving motion of a droplet into wider regions of the wedge. The Laplace pressure force has been found to be a function of both the α and the droplet volume. This pressure gradient is also the explanation behind droplet movement along conical shapes (cactus, awns, etc.), where the radius varies along the surface induce droplet movement. When the radius of curvature is high, ΔP is low and inversely. Therefore, the difference in Laplace pressures cause liquid to

move from high to low curvature regions. On a conical shape, a droplet will move from a low radius (tip of the cone) towards high radius (base of the cone). This concept is synonymous with the droplet movement from narrow to wide regions.

Both these forces represent forces that are led by the hydrophilic effect of the surface, effectively pulling the droplet inwards. Then, the wettable difference force is the force that is concerned with how the hydrophobic edges push the water inwards and is defined as:

$$F_{wd} = 2L\gamma\left(\cos\theta_{avg} - cos\theta_{phobic}\right)sin\alpha \quad (20)$$

Where θ_{avg} and θ_{phobic} are the average and hydrophobic contact angles of the droplet. Finally, the resisting force of hysteresis corresponds to

$$F_a = 2L\gamma sin\alpha cos\theta_{r-phobic} - cos\theta_{a-philic} \quad (21)$$

Where $\theta_{r\text{-}phobic}$ and $\theta_{a\text{-}philic}$ are the receding contact angle at the hydrophobic edges and advancing contact angle in the hydrophilic region, respectively. Thus, this work has shown the possibility of controlling water droplet movement passively through the modification of surface wettability and how this can be used to improve the state of fog harvesting.

Another recently studied technique for collecting water was developed by Zheng et al. [107] They looked to nature and found that spider silk was composed of evenly spaced spindle-knots that promote droplet growth at specific location through directionally displacement of water towards these protrusions. This represents a geometrical and topological method for passively enhancing droplet movement along a wire [76], [107], [108]. SEM images (Figure 16 (a)) of wet spider silk show that these spindle-knots are essentially randomly aligned nanofibril groupings spaced between aligned nanofibrils. Laplace pressure gradient is the dominant mechanism for droplet movement towards spindle-knots.

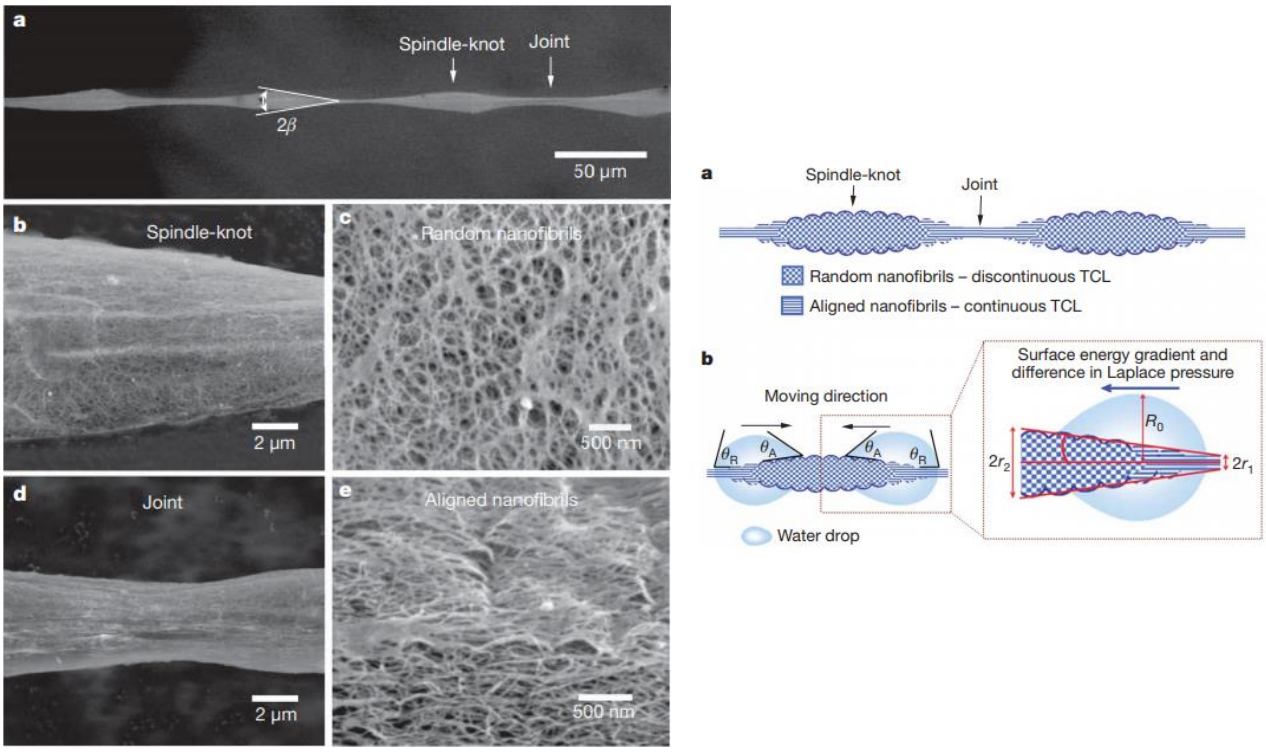

Figure 16. (a) SEM micrograph of spider silk and spindle-knots. (b) schematic of water movement on spindle-knots [107]

Several studies have shown the possibility of creating such biomimetic surfaces through electrospinning or solvent drying methods. For the former, Dong et al. [26] used coaxial electrospinning of a dilute poly(methyl methacrylate)(PMMA) and concentrated polystyrene (PS) solution as the outer and inner solutions. When these are pumped out, the PS forms a fiber through stretching by electrostatic force while the PMMA, adhering to the PS fiber, retracts and forms periodic knots. For solvent methods, Zheng et al. first placed a nylon fiber into a poly(methylmethacrylate)/N,N-dimethylformamide-ethanol (PMMA/DMF-EtOH) solution and then pulled it out rapidly leaving a thin coating of the PMMA/DMF-EtOH solution. The coating separated into caps along the fiber and then dried. This yielded an artificial spider silk-like material.

These two examples have shown how surface chemistry and microstructures are the leading research elements in the field of fog harvesting. Macroscopically, Shi et al., have presented a different approach for enhancing fog harvesting by proposing a vertically aligned wire concept, as opposed to a mesh-like or flat surface [33]. By placing a series of evenly spaced wires, they found

that fog collection was drastically increased when compared with traditional grid designs. This study brought to light the importance of clogging in the process of fog harvesting. Clogging is the phenomenon that occurs when water impinges onto a surface, grows and coalesces with nearby drops, and fills the open space between adjacent wires. This affects fog flow because it blocks the preferential pathway of fog. Although this can be beneficial, due to the increased amount of time that fog is in contact with water, the issue lies in the removal of water once the surface is clogged. The adhesion forces become more and more important as water meets additional surface area. Thus, overall, collection efficiency is decreased. Figure 17 shows the different cases that induce clogging. In the top left, the wires of the mesh are too packed, leading to a high amount of clogging. In the case where the spacing is too large, the amount of water that comes into contact with the screen is reduced. In the bottom images, single vertical wires are shown. The important aspect here is to carefully select the distance between each wire (i.e pitch) so as to lower the possibility of clogging as seen in the bottom left schematic.

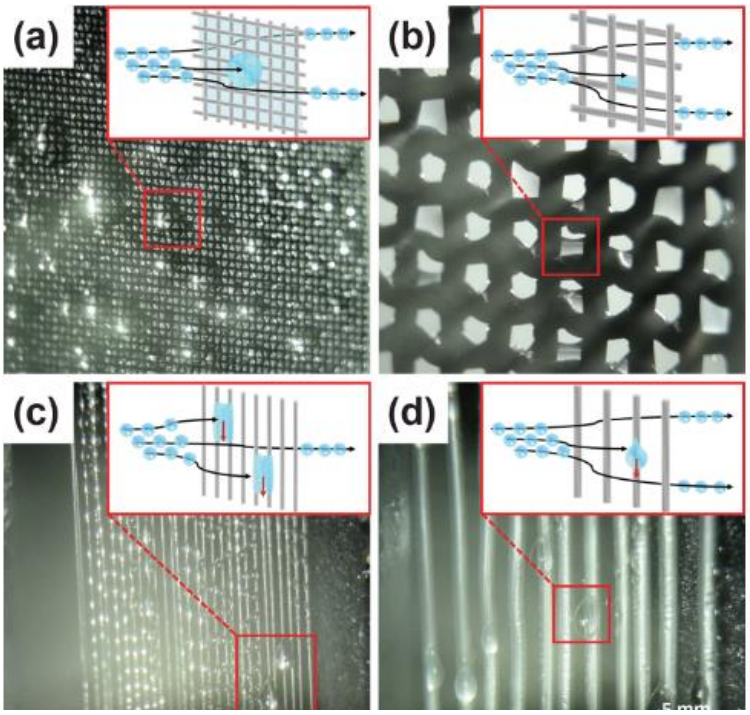

Figure 17. (a) Water clogging on tightly spaced wire mesh, (b) Low water impact on highly spaced wire mesh, (c) Clogging on tightly spaced vertically aligned wires and (d) Reduced clogging on spaced vertically aligned wires. [33]

Despite the advancement of fog harvesting technologies, several limitations must be addressed in order to ensure the long-term viability of this freshwater generating technique. Firstly, and most importantly, seeing as most large-scale fog harvesting projects use polymeric materials, there have been issues with their durability [23], [29], [34], [35], [99]. When exposed to harsh atmospheric conditions like high wind speeds and debris, it has been reported that some meshes break over a period of time. This is an important issue because in remote locations, it becomes increasingly difficult to provide appropriate on-site maintenance for fog harvesters and often times, projects are abandoned for this reason. This also leaves the polymeric material waste into the ecosystem that contributes to its pollution. Secondly, the reported fog collection efficiencies, while sufficient for basic needs in some regions, are still low and cannot completely replace the need for external freshwater sources. Thirdly, geometrical design that lead to clogging have been shown to reduce the fog harvesting performance. Other drawbacks in fog harvesting involve concerns about the quality of the water captured by fog, which is a function of the quality of fog (acidity, particulate matter concentration etc.), simplicity and applicability of fog harvesters, economic considerations as well as political issues with adopting such projects over the implementation of other water generation sources such as reverse osmosis plants or conventional water supply systems [23], [99].

Ultimately, the parameters to keep in mind upon the design of a fog harvesting project are cost-effectiveness, simplicity, passive (no or minimal energy consumption), marginal operating costs and high collection efficiency.

2.4.2 Fog Collection Efficiency

As fog is driven towards the collector, only a fraction of water hits the collector surface area. This is known as the shade coefficient (SC) and is expressed as the percentage of solid collector exposed to incoming fog:

$$SC = 1 - \frac{A_{op}}{A} \quad (22)$$

where A_{op} and A are the opening and total area, respectively [95], [96]. Park et al. have defined a similar expression for the shade coefficient adapted for mesh collector that included a dependency of the wire diameter:

$$SC = \frac{X}{L^2 + X} \quad (23)$$

$$X = r_{wire}(r_{wire} + c) \quad (24)$$

Where r is the wire radius and c is the distance between two wires [38]. Seeing as most fog harvesting materials consist of mesh-like surfaces, equation 24 is considered to be more accurate [95]. To counter the difficulty in reporting fog harvesting data, several researchers have developed standard equations for characterizing overall fog collection efficiency ($\eta_{collection}$) of a material [31], [33], [34], [38], [95], [96]. This collection efficiency is a function of local climatic variables such as fog liquid water content, drop size distribution and wind speed but also from surface design variables like geometry and material selection. Thus, collection efficiency depends on two main factors: fog flow aerodynamics and water deposition. Aerodynamics quantify the amount of water droplets that come into contact with the surface. In a fog harvesting scenario, aerodynamics are dependent on pressure difference of the fog flow across the capture surface and drag in the overall flow [31], [33], [95], [96]. These phenomena are expressed through two coefficients, the pressure loss coefficient (C_o) that is dependant on the shade coefficient and drag coefficient (C_d) [31], [33], [95], [96]. The pressure loss coefficient is given by

$$C_o = 1.3SC\left(\frac{SC}{1 - SC}\right)^2 \quad (25)$$

The velocity locally decreases at the solid interface because of no-slip and no penetration boundary conditions [38]. The drag coefficient thus models this momentum and C_d can be found in the literature depending on the geometry of the mesh. This value for cylinders is approximately to 1.15 [34], [95], [96]. From this, the aerodynamic efficiency (η_a) is given by

$$\eta_a = \frac{SC}{1 + \sqrt{\frac{C_o}{C_d}}} \quad (26)$$

Although this represents the fraction of unperturbed fog flow that can be captured by a collector, not all impacting droplets are retained and further collected [31], [33], [34], [38], [95], [96]. This occurs when droplets deviate from their initial trajectory around an object without adhering to it due to bouncing of the droplet off the surface [31]. Deposition can be explained as a trade-off between water captured and drained. The capture or impaction mechanism is therefore the potential

of droplets to remain on the collector. Several mechanisms have been proposed for impaction such as inertial impaction, direct interception, Brownian diffusion motion and gravitational sedimentation [95]. Brownian diffusion is known to contribute significantly when droplets are below 1μm [22], [95]. Direct interception becomes significant under conditions where the droplet diameter is in the same order of magnitude or larger than the wire dimension [22], [95]. Gravitational sedimentation plays a significant role in impaction when droplets are larger than 80μm, which is much larger than typical water in fog [95]. Thus, generally, these three mechanisms are neglected when evaluating the capture efficiency. Finally, inertial impaction is the main mechanism involved and is expressed as a function of the Stokes number [22], [31], [33], [95]. The Stokes number is then used to calculate the fog deposition efficiency, η_d.

$$St = \frac{2\rho_{air} D^2 V}{9\mu_{air} R} \quad (26)$$

$\rho_{air}: Density\ of\ air$

$D: Fog\ droplet\ diameter$

$V: Fog\ velocity$

$\mu_{air}: Viscosity\ of\ air$

$R: Fog\ harvestor\ wire\ radius$

$$\eta_d = \frac{St}{(St + \frac{\pi}{2})} \quad (27)$$

The overall collection efficiency can be expressed as a product of both aerodynamics and deposition efficiencies.

$$\eta_{collection} = \eta_a \eta_d \quad (28)$$

Having a better understanding of how macroscopic design can affect fog collection, we must therefore be mindful during the selection of physical properties such as shape and geometry upon the design phase of the fog harvesting surfaces presented in this research project.

Looking at the development of fog harvesting, it is important to gain better understanding in how surface properties can affect the performance of an eventual collector. In the following sections, we look at two important factors that influence surface wettability: topology and chemistry. To

properly design a fog harvester, we descend further to see how structural features on the nanometric scale affect performance.

2.4.3 Influence of Topology

Topological surface modifications have been found to lead to superhydrophobic surfaces. This was first observed by looking at biological surfaces like the *Nelumbo* leaf, commonly known as the lotus leaf. This superhydrophobicity is induced by the presence of micropapillae, themselves covered by branch-like nanostructures. Other natural surface that exhibit such behaviour are rice leaves, butterfly wings, giant Salvinia leaves and many more. The texturing can be of microscopic or nanoscopic scale and may lead to two distinct wettability models: Wenzel (liquid penetrates the space between structures) and Cassie-Baxter (penetration does not occur). Air pockets are formed in the grooves and they lift the liquid above them in the Cassie-Baxter state. In both cases, hydrophobicity is amplified. In fog harvesting, hierarchal topography is known to enhance collection efficiency due to this hydrophobic effect. Ideally, a hydrophobic low-adhesion (Cassie-Baxter type) surface is preferable in order to rapidly shed water droplets from the surface. This will dewet completely and reduce the chance of clogging on a surface. Texturing a surface can be done through physical (direct templating) and chemical – solvent or solvent-free methods [27], [77], [109]. Inducing topological modifications via solvents include methods such as spin coating, sol-gel, electrospinning and single or multi-step protocols [110], [111]. Solvent free methods include chemical vapor deposition and plasma processing for instance [112], [113]. As mentioned in the previous section, electrospinning was used to mimic spider silk spindle knots. Another example of surface nanostructuring in fog harvesting has been presented by Raut et al. [27] They employ nanoimprint lithography, a templating technique to generated a surface with an array of micro-lenses onto which nanofibrils were then added through the same process. This nanostructure imparted a superhydrophobic quality that can be beneficial for rapid water removal on a fog harvesting surface.

2.4.4 Influence of Surface Chemistry

Surface chemistry plays in the force balance between water adhesion and further collection. While hydrophilic surface features enhance water capture and coalescence, fully hydrophilic surface are

not favorable for water collection because water removal becomes an issue. This stems from the high adhesion water has with hydrophilic groups on a fog harvesting surface, reducing the probability of dropping and collection. In this respect, the only way for water to be collected from a fog harvester is by waiting for water to grow to the point where its gravitational force exceeds the adhesion force it exhibits towards the surface. Additionally, increased pinning of water on a fog harvesting substrate was found to lead to increase clogging and thus, hinder aerodynamic flow of fog and lower removal efficiency. On the other hand, homogeneously hydrophobic surface can rapidly shed water, but the droplets do not have the opportunity to grow and collect additional incoming fog droplets. Between both of these homogenous wettability surfaces, however, it has been found that hydrophobic ones yield higher water collection rates in fog harvesting conditions. Increases between 20-180% were experimentally observed with hydrophobic surfaces when compared to hydrophilic [30], [31], [37], [104].

It should be mentioned that these conclusions are completely inversed in the case of moisture harvesting (AWG) as hydrophilic surface aid water vapor heterogeneous nucleation due to lower contact angles as seen in previous sections. Therefore, to counter the limitations of each case (hydrophobic and hydrophilic), heterogeneous or patterned wettabilities have been explored. Heavily inspired by biological phenomena, patterned surfaces composed of a wide variety of shapes and materials have been explored. These have been discussed previously in Chapter 2.4.1.

Knowing the importance of wettability in collection rates, it became important to investigate this parameter in our own research. To accomplish this, functionalization was used as a surface modification technique on fog harvesting substrates.

2.5 Functionalization

Functionalization methods can be categorized as wet or dry. The former uses solvent-based chemistry to functionalize surfaces. The latter employs gas phase precursors to accomplish this. Wet methods benefit from a high controllability of the desired reactions, process conditions and lack of specialized equipment, simplifying the entire method and rendering it cost-effective at lower scales [39], [114]–[116]. However, there are considerable drawbacks and especially in the framework of this research project. Solvent techniques can often generate undesired side-products that can be damageable and, at larger-scales, must be separated and dispensed in a safe manner.

For the substrates used in this project for fog harvesting, stainless steel meshes covered with carbon nanotube (CNT) forest, wet functionalization can be damaging to the CNTs. Thus, although relevant in other spheres of research, solvent techniques are not further discussed in this master's thesis and the focus will be on dry functionalization methods.

2.5.1 Chemical Vapor Deposition

Chemical vapour deposition (CVD) is a versatile technique for producing conformal thin films, coatings, powders and nanomaterials [41], [113], [117]–[120]. This is achieved through the decomposition of a gaseous precursors onto a substrate. The general mechanism is as follows: a precursor gas is injected into a closed reactor. This gas is submitted to an energy source that causes its decomposition. Once the reactant is decomposed, it follows the following steps (in reference to Figure 18):

1. Reactants then diffuse through a boundary layer above the solid substrate. Highly reactive molecules from the gas can then react amongst themselves in the gas phase, bounce off or adsorb to the substrate;
2. Upon adsorption. Surface diffusion and/or chemisorption processes bring the species to preferred nucleation sites where chemical reactions occur (i.e. propagation);
3. This corresponds to the growth step, forming the final product;
4. Reaction by-products diffuse away from the substrate;

5. Desorbtion of some by-products from the surface and diffuse towards the outlet.

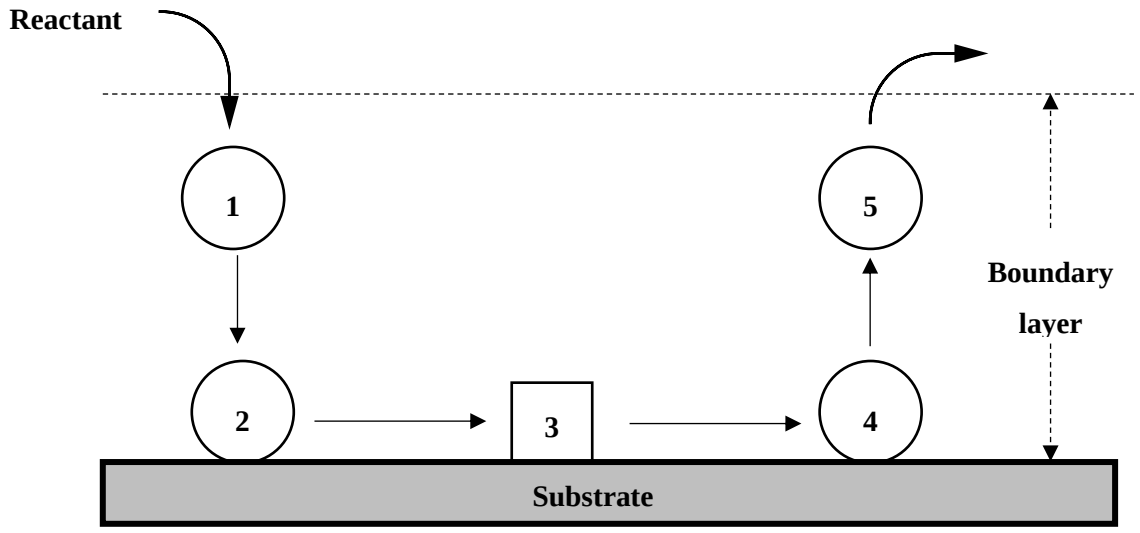

Figure 18. CVD process steps

Within this process, gas phase reactions are undesired. Figure 17 presents a schematic of the sequential steps that occur in CVD. The versatility of this technique stems from its ability to use a wide variety of precursor gases, depending on the desired product, as well as the initiation source for decomposition. Typically, CVD sub-categories are either classified by this initiation source for deposition to occur (temperature, plasma, photons etc.) or process conditions (pressure). These can be plasma-enhanced (PECVD), thermally activated (TACVD), microwave plasma-assisted (MPACVD), atmospheric pressure (APCVD), metal-organic (MOCVD), photo-initiated (PICVD) etc. Table 3 presents a brief description of these sub-categories [119]. This list is intended to emphasize the flexibility of CVD and does not include all developed methods.

Table 3. Summary of CVD techniques

Technique	Description
Plasma-enhanced (PECVD)	Uses ionised gas species (plasma) to enhance reaction rates
Thermally activated (TACVD)	Uses heat to initiate and maintain reactions
Photo-initiated (PICVD)	Uses photons to initiate and maintain reactions
Atmospheric Pressure (APCVD)	Atmospheric pressure process
Low pressure (LPCVD)	Sub-atmospheric pressure process
Ultrahigh vacuum (UHVCVD)	Pressures in the order of 10^{-6}Pa
Microwave plasma assisted (MPACVD)	Glow-discharge plasma generated with microwaves initiates and maintains reactions
Atomic layer (ALCVD or ALD)	Deposition occurs 1 dimensionally, layer by layer

For all these methods, the CVD apparatus components are similar [114]. Each system consists of:

1. Gas delivery system
2. Reactor chamber
3. Energy source
4. Vacuum system
5. Exhaust system
6. Exhaust treatment system
7. Process controllers.

There exists a vast array of possibilities, but plasma and thermally driven methods are often regarded as staples in CVD technology. CVD presents many advantages when compared to other thin film deposition techniques [113], [114], [120]. Firstly, it provides a wide array of choices for precursors, initiation sources and process conditions making it a versatile technique that can be adapted for many purposes. In terms of precursors, CVD has been successfully used with organic and inorganic compounds spanning 70% of elements in the periodic table [113]. Secondly, it generates conformal depositions. Conformity is a property that describes the ratio between vertical and horizontal growth on a surface [120]. It is a factor that represents the geometrical uniformity of the thin film. This is particularly important for structured surfaces as they are not completely flat and possess surface deformations such as crevasses, micro or nanostructures and contours. When this ratio is unity, equal growth is achieved on all exposed surfaces independently of their orientation. Figure 19 shows different conformal depositions.

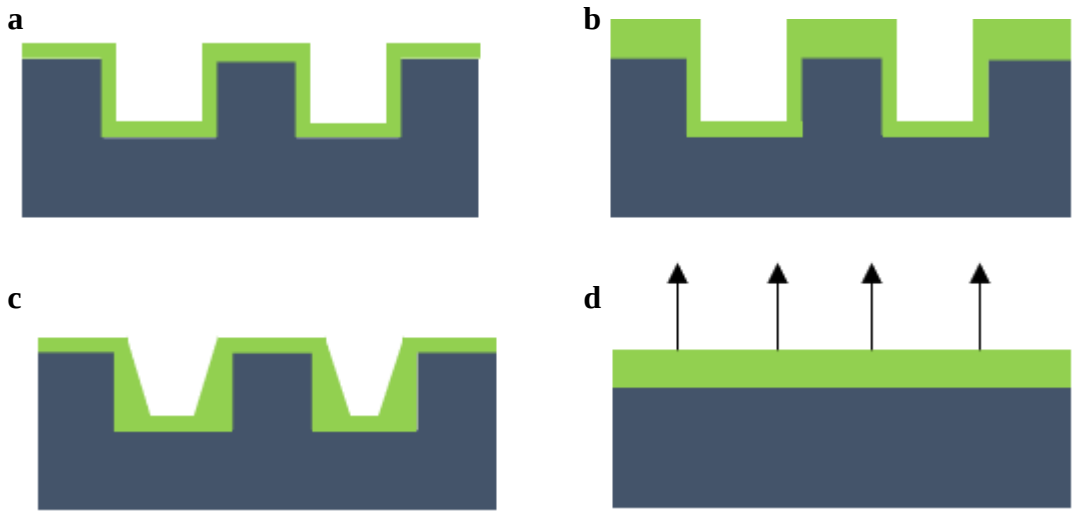

Figure 19. Conformal (a,d) and non-conformal (b,c) coatings

Thirdly, chemical vapor deposition is known to provide good control on deposition rates depending on the application. Typically, low deposition rates are desired for microelectronics thin film coating due to the epitaxiality of CVD depositions [41], [120]. However, for thick coatings, used in fields such as protective wear and erosion resistant coatings, high deposition rates are preferred [120]. Limitations associated to the CVD processes include the complexity of such process, and the requirement of a profound understanding of the designed system and the molecules involved. Finally, some applications of CVD use hazardous chemical compounds that present safety

considerations for researchers. It is also important to assess the health hazards of the product depending on its use post-deposition.

2.5.2 Thermodynamics of CVD

In all the CVD embodiments presented previously, thermodynamics describes the driving forces that will dictate whether a reaction will occur [113], [117]–[120]. This will determine the feasibility of a chemical reaction. The spontaneity of thermodynamic processes can typically be deduced from changes in entropy (ΔS). The second law of thermodynamics states that this change in entropy must be positive for a process to occur spontaneously. However, in the case where the driving force is chemical in nature, Gibbs free energy (ΔG_r) is used to describe this spontaneity. Generally, chemical thermodynamics are considered because it deals with the transfer of energy between chemical states and thus allows for strong predictions of the reaction dynamics at different experimental conditions. Thus, much like for entropy, a spontaneous CVD reaction in the forward direction (i.e.: product formation) will take place when the Gibbs free energy change is negative. In such cases, a process is known to be exergonic. If this value is positive for given conditions, no reaction will occur, and the process is referred to as endergonic.

$$\Delta G < 0 - Favorable, spontaneous\ reactions \quad (29)$$

$$\Delta G > 0 - Unfavorable, non-spontaneous\ reactions \quad (30)$$

In the case where multiple reactions are possible in a system, the reaction with the most negative ΔG_r will dominate and lead to the most stable products. Gibbs free energy is calculated from the enthalpy (ΔH_r) and entropy (ΔS_r) of reaction as well as temperature of the system (T)

$$\Delta G_r = \Delta H_r - T\Delta S_r \quad (31)$$

The enthalpy of reaction is calculated by subtracting the formation enthalpies of reactants to the products. This data is readily available in the literature for many species.

$$\Delta H_r = \sum \Delta H_f\ (product) - \sum \Delta H_f\ (reactants) \quad (32)$$

This equation can also be applied for reaction entropy such that Gibbs free energy of reaction can be rewritten as:

$$\Delta G_r = \sum \Delta G_f(product) - \sum \Delta G_f\ (reactants) \quad (33)$$

Furthermore, the change in free energy of reaction can be used to calculate the equilibrium constant K_T. This constant describes the relationship between products and reactants at the point of equilibrium and, for gases, can be expressed through the partial pressures of each species (n):

$$K_T = e^{-\frac{\Delta G_r}{RT}} \quad (34)$$

$$K_T = \frac{\prod_{i=1}^{n} p_i\ (products)}{\prod_{i=1}^{n} p_i\ (reactants)} \quad (35)$$

Thus, this equilibrium constant can be used as a criterion to ascribe feasibility of a CVD process. If K_T is positive, then there are more products than reactants in the system and can be visualized as the consumption of reactants and a forward motion of the desired reaction. In the opposite case, no products are formed, hence, no reaction is occurring in the system. It follows that a higher equilibrium constant results in more thermodynamically favorable reactions. In the situation where data is unavailable for standard change in entropy (ΔS^0), enthalpy can be used to approximate CVD feasibility. Considering that most CVD occur above ambient temperature, endothermic reactions would be considered favorable as heat is consumed to form a new product, whereas exothermic ones are less likely to occur at higher temperatures. Once feasibility has been assessed, it is important to understand how species in the reaction mixture interact with each other and the deposition surface.

2.5.3 Kinetics and Mass Transport in CVD

CVD occurs in sequential steps: (1) Transport and diffusion of reactants through the boundary layer towards the substrate; (2) adsorption onto the substrate; (3) diffusion towards preferential nucleation sites; (4) surface chemical reactions; (5) desorption and evacuation of by-products. Each of these steps occur in order and possess their own kinetics [113], [118], [120]. However, the overall CVD kinetics will be determined by the slowest of these steps – the rate determining step. CVD can thus operate under three mass transfer control groups [118]. The first group is equilibrium process where the input and output (steps 1 and 5) are the rate-limiting steps. This implies that the mass transfer through the boundary layer and surface reactions are fast. The second type of control occurs when the diffusional mass transfer through the boundary layer (2-5) is the rate-limiting step.

In the case where diffusional mass transfer is the limiting step, the diffusion rates of the reactant through and out of the boundary layer are crucial. For this control type, typically, temperature, pressure and gas velocity are low, causing an increase in the boundary layer thickness, making it more difficult for reactants to diffuse through it. Also, high temperatures usually tend to increase reactant decomposition and surface reactions. Finally, the last group is kinetic control in which the surface adsorption, reaction and desorption are the slowest. Surface kinetically controlled CVD processes occur when temperature and pressure are low. Lower pressures reduce the thickness of the boundary and reactants can easily diffuse and adsorb to the substrate. Relationships between process parameters have been found to predict whether a CVD reaction is of equilibrium, diffusional or surface control type. These are shown in Table 4.

Table 4. Relationship between process parameters and rate-limiting steps [118]

Control type	Growth variable	Effect on Growth Rate
Equilibrium	Temperature (T)	Decreases rapidly with increasing T (exothermic) OR Increases with T (endothermic)
	Flow rate (F), gas velocity (v)	Linear increase with F, independent of v
	Substrate crystal orientation	Independent
Diffusion	Temperature	Moderate increase with T for both endothermic and exothermic reactions
	Flow rate, gas velocity	Linear increase with both F and v
	Substrate crystal orientation	Growth rate depends on orientation.
	Pressure (P)	Decreases with P

Surface	Temperature	Exponential increase with T for both endothermic and exothermic reactions.
	Flow rate, gas velocity	Independent
	Substrate crystal orientation	Growth rate depends on orientation.
	Pressure	Decrease with P

From these relationships, it is possible to deduce the dominating kinetic and mass transport phenomena within a CVD system.

2.5.4 TACVD and CNT Growth

As mentioned in previous sections, TACVD is one of the most used techniques [114], [119], [120]. A block diagram of the components involved in TACVD are shown in Figure 20. It employs thermal energy that can be provided by radio frequency (RF) heating, infrared radiation or resistive heating. Thermal decomposition of precursor gas over a hot surface is known as pyrolysis [118]. Pyrolytic reactions can be represented in the general from: $AB_{(g)} \rightarrow A_{(s)} + B_{(g)}$. Examples of this genre of reaction include carburization and nitridation such as the decomposition of methane (CH_4) onto a heated surface. Reduction reactions are also possible when hydrogen is present as a reducing

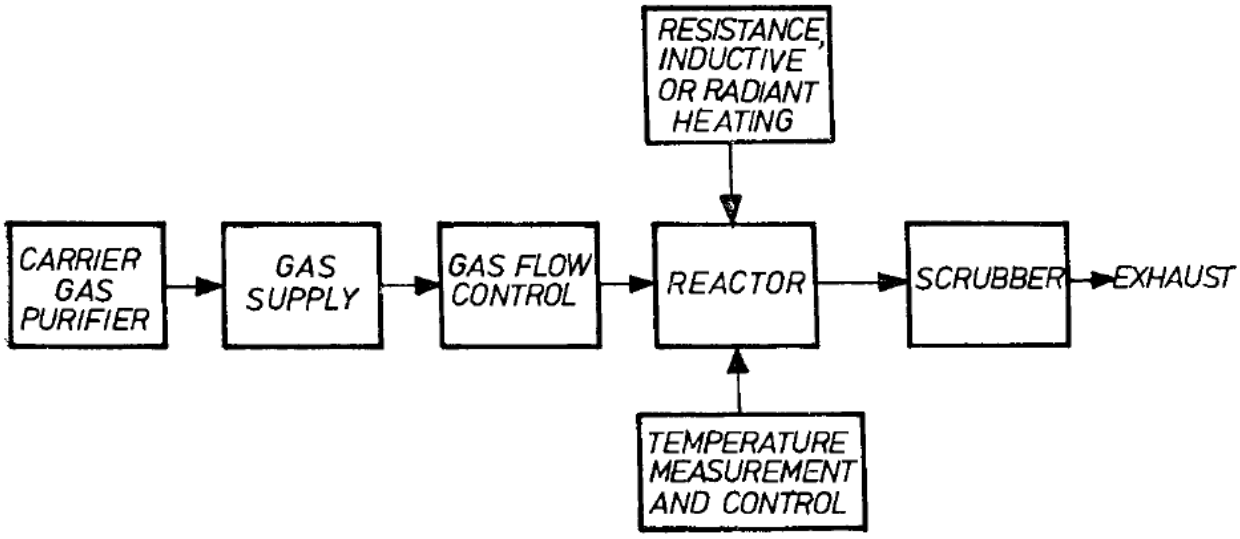

Figure 20. Block diagram of TACVD process [118]

agent under high heat ($2AB_{(g)} + H_2 \rightarrow 2A_{(s)} + 2HB_{(g)}$) [118], [119]. Besides these most common reaction pathways, other possible routes include exchange, disproportionation and coupled reactions [118]–[120]. Finally, reactor configuration can be hot or cold walled. In a hot wall configuration, the entire reactor is heated, typically from the outside in, much like a furnace. In the case of a cold wall reactor, only the substrate is heated.

In this research project, Carbon nanotubes (CNTs) grown onto stainless steel substrates were used as a fog harvesting substrate. CNTs can be grown via TACVD. Most often, this is done through the decomposition of a hydrocarbon gas onto a substrate possessing nanoparticle catalysts that serve as nucleation sites for CNT growth. These nanoparticles are typically transition metals such as iron (Fe), cobalt (Co), nickel (Ni) or alloys serve as a template for a metallurgical phase transformation. The entire process occurs at temperatures between 500-1200°C and the heat is the initiation source for precursor decomposition. There is still uncertainty on the growth mechanism of carbon nanotubes. At first, the most widely accepted model is the Vapor-Solid-Solid (VSS) model [121]–[123]. It stipulated that excess carbon molecules from the decomposition step precipitates onto the substrate and diffuses into the catalytic sites due to a concentration gradient. It then nucleates and grows outwards to form nanotubes. This theory, however, was dismissed in this case. It is important to consider several elements to appropriately describe the CNT growth mechanism such as the affinity of the substrate with carbon and the diffusivity of carbon in the substrate [112], [124]. Typically, transition metals with a large number of unfilled d-orbitals are preferred for bonding with carbon. Thus, on the periodic table, affinity for carbon increases from right to left. Iron, the template used in this research, lies in the middle of these transition metals, possessing a finite number of unfilled d-orbitals that can allow for carbon solubility and therefore the possibility of CNT growth. That being said, the actual mechanism responsible for CNT growth is still highly debated. Despite this, the outcome nanomaterial can be tailored through the selection of metal catalysts (geometry, size, material etc.) due to a considerable amount of experimental results. Two distinct growth types have been proposed upon CNT nucleation at catalytic sites: tip or base growth [122]. In the former case, nanotubes grow below the catalyst particle, effectively lifting it as it nucleates. In the latter case, the opposite occurs and CNTs grow above the nanoparticle. In the case of this research project, CNT forests are grown directly onto stainless steel grids that act both as a substrate and catalyst. This allows for a strong attachment of the CNTs on

the surface as it grows directly from it. Further details on the CNT growth procedure is given in Chapter 4.

2.5.5 PICVD

Photo-initiated chemical vapor deposition (PICVD) uses UVC light to initiate photochemical reactions in the gas phase [116], [117], [119], [125]. To obtain a better understanding of the complexities of the PICVD process, it is necessary to lay out the fundamentals of photochemistry. Photochemistry is a field that studies chemical reactions that are caused by light [126]–[128]. This source, characterized through its wavelength λ, can be infrared (1 mm - 750 nm), visible light (760 nm – 380 nm) and ultraviolet (400 nm - 10 nm) [129], [130]. To assess the energy contained in a photon of a specific wavelength, Planck's equation is used:

$$E(eV) = \frac{hc}{\lambda} \quad (36)$$

Where h is Planck's universal constant and c is the speed of light [129], [130]. The inversely proportional relationship of E and λ show that lower wavelengths possess higher photon energies. It then follows that in photochemistry, these photons provide energy required to initiate a chemical reaction. This activation energy carried by photons is considerably higher when compared thermal energy required for a reaction. For example, a photon at 254 nm at room temperature holds 190 times the amount of energy available thermally (kT) [131]. There are two fundamental criteria that need to be filled for a photochemical reaction to occur: first, there must be an overlap between the spectral emission of the light source and the absorption spectrum of the targeted molecule; second, the absorbed photon must have enough energy to initiate the reaction [131]. Photochemical

reactions can be classified as isomerization, coupling or bond cleaving reactions as seen in Figure 21.

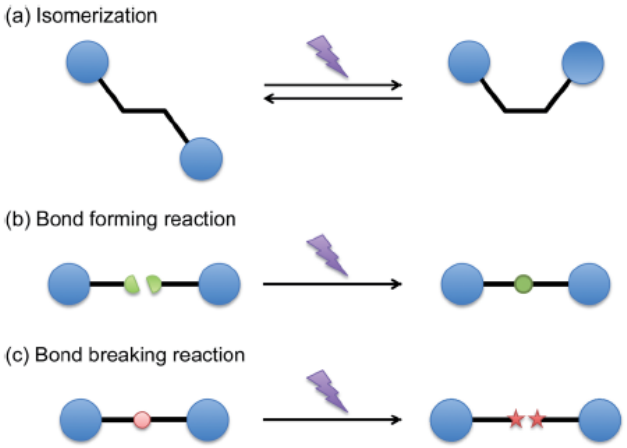

Figure 21. Possible photochemical reactions [131]

The most common reaction that occurs in photochemical polymerization is bond cleavage. The key is to select the appropriate molecules that obey the criterion in order to successfully carry out the desired reaction. Finally, other than the energy density of a photon compared to other energy sources, photochemical reactions are easily controlled by turning the light source on or off and they eliminate the need for external solvents or catalysts for a reaction [131].

In PICVD, the photonic energy can be provided by a range of lamps such as KrL (λ_{peak}=123.6nm) and XeL (λ_{peak}=147nm) [132]. In the case of the research presented here, UVC low-pressure Hg discharge germicidal lamps were employed [116], [133]. This source emits primarily at a wavelength of 253.7 nm but possesses smaller emission peaks at 546nm, 436nm, 405nm, 365 nm, 313 nm and 185 nm (Figure 22). This last peak is especially important because it is highly energetic (6.7 eV) and represents about 7% of the 253.7 nm peak [132]. Thus, by following the criteria for the initiation of a photochemical reaction, precursors for PICVD are selected based on their capacity to absorb at these wavelengths and the energy required to cause a photochemical reaction.

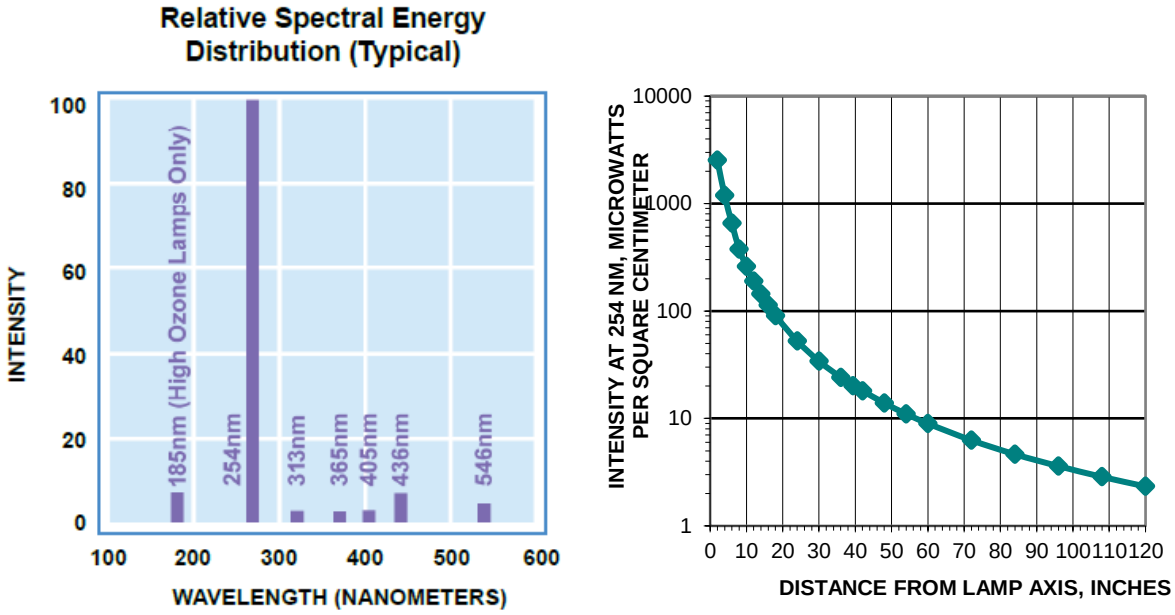

Figure 22. Relative spectral distribution of UVC lamp and intensity with respect to distance from the lamp [241]

In the context of this research project, these precursors consist of carbon monoxide, hydrogen, iron pentacarbonyl and hydrogen peroxide. Table 5 presents the ionization potential, dissociation energies and absorption of these compounds:

Table 5. Photochemical properties of PICVD precursors [134]–[137]

Species	Ionization potential	Dissociation energy	Absorption
H_2	15.42 eV 80.4 nm	4.52 eV 274.3 nm	$< 110.8\ nm$
CO	14.01 eV 88.5 nm	11.14 eV 112.3 nm	$< 200\ nm$
H_2O_2	10.6 eV 117 nm	2.04 eV 608 nm	$< 400\ nm$
$Fe(CO)_5$	8.35 eV 148.5 nm	0.37 eV 3350 nm	$< 253.7\ nm$

From these values, it is possible to observe that the energy provided by the UVC lamps are absorbed by CO, H_2O_2 and $Fe(CO)_5$. Hydrogen is not initiated by the energy source. The energy provided by the secondary emission peak (185nm/6.7eV) is not sufficient to fully dissociate CO. However, 3.7 eV are required to provoke constituent π-bond dissociation and it is thus possible for this to occur in the PICVD system [134]. Generally, UV light initiates a free radical polymerization of

gaseous species. Free radical polymerization (FRP) can be classified as a chain polymerization reaction that is initiated by a free radical [138]. These correspond to highly unstable, unpaired electrons in chemical species. In FRP, a free radical (R*) is generated thermally or, in the case of the work presented in this project, by light. Alternatively, an external initiator molecule can be added to generate R*. Then, R* can attack bonds in the monomer, which will then leave a new unpaired electron at the end of the polymer chain that will continue to react with new monomer. This process is called propagation and ends with a termination step. In this last step, two propagating polymer chains can meet and either combine with one another to form a single and final polymer chain (Combination) or form two separate chains (Disproportionation). The four steps for FRP are therefore: (1) Decomposition of initiator into free radicals, (2) Initiation of the polymerization reaction, (3) Propagation and (4) Termination. Classical kinetic equations for each step are presented below:

$Decomposition\ and\ Initiation$	$I_2 \overset{k_d}{\rightarrow} 2R^*$	$r_i = 2fk_d[I]$
$Propagation$	$M_x^* + M \overset{k_p}{\rightarrow} M_{x+1}^*$	$r_p = k_p[M^*][M]$
$Termination - \begin{matrix} Combination \\ Disproportionation \end{matrix}$	$M_x^* + M_y^* \overset{k_{tc}}{\rightarrow} M_{x+y}$ $M_x^* + M_y^* \overset{k_{td}}{\rightarrow} M_x + M_y$	$2(k_{tc} + k_{td})[M^*]^2$

$I: initiator$; $M_i: monomer\ i$; $R^*: initial\ radical$; $*: free\ radical$; [ ]: $Concentration$

$r_i: initiation\ rate$;

$r_p: propagation\ rate$;

$k_d\ decomposition\ rate\ constant$;

$k_p: propagation\ rate\ constant$;

$k_{tc}: termination\ by\ combination\ rate\ constant$;

$k_{td}: termination\ by\ disproportionation\ rate\ constant$

In the case of photo initiated FRP, the difference in these equation lies in the initiation step. The rate constant k_d is replaced by parameters that account for photo-initiator properties such as extinction coefficient or molar absorptivity of the initiator (ϵ) and free radical efficiency (f), as

well as other important properties like the intensity of the light source (I_0), the thickness of the polymer film (d) and the quantum yield of photocleavage (Φ) [139].

$$r_i = 2f\Phi I_0[I]\epsilon d\ln(10) \quad (37)$$

This reaction can be carried out in all three phases (gas, liquid or solid) but only occur in both the gas and solid phase in the case of the PICVD works described [125], [140]. PICVD therefore produces thin films onto a substrate that can be tailored depending on the process parameters. One of the main aspects studied on the PICVD system is wettability, that is, functionalizing a surface to render it hydrophobic or hydrophilic. This was a crucial element to this research project, as wettability greatly influences fog harvesting capabilities. Therefore, superhydrophilic and superhydrophobic functionalization was performed on our substrates to observe these differences in fog harvesting conditions. In the superhydrophilic case, an aging phenomenon, known as hydrophobic recovery, where the functionalized surface loses its hydrophilicity over time was observed. Hydrophobic recovery has been observed in the literature by several research groups upon hydrophilic functionalization through many methods (PICVD, PECVD…) and is often attributed to surface restructuring and/or diffusion of oxygen-rich functional groups towards the bulk of the deposition rather than remaining exposed at the top of it (interface) [141]–[145]. This phenomenon was studied in depth and the results of this are further described in Chapter 4.

CHAPTER 3 SPECIFIC OBJECTIVES AND METHODOLOGY

In order to contribute to the field of fog harvesting, it is important to learn from past and ongoing work presented in the literature. This includes the major limitations of fog harvesting technologies and how research groups are tackling these. The most important elements that are addressed concerning fog harvesting surface design are geometrical, topological and chemical ones. These were all considered and explored in this research project.

3.1 Main Objectives

The main objective is to design an effective and scalable fog harvesting device that addresses the current drawbacks in fog harvesting technology. As mentioned previously, these include reducing clogging on the harvesting surface, reducing re-entrainment of liquid droplets, durability of the material and increasing the amount of available capture surface area.

3.2 Specific Objectives

The project was therefore divided into three specific objectives:

- Compare the effects of mesh and single vertically aligned wires geometries on clogging of fog harvesters;
- Increase the presence of microscopic topological modifications to improve fog harvesting collection rate;
- Link surface wettability to fog capturing performance and design of optimized fog harvesting surface.

3.2.1 Specific Objective 1

The first specific objective is to determine the effects of macroscopic design parameters on fog harvesting performance. In this objective, macroscopic physical design elements were investigated. Considering that clogging in fog harvesting occurs in mesh-like nets, modifying the basic geometry and assembly of the capturing device was the strategy. Two different types of surfaces were compared to study the effect of surface geometry on fog harvesting performance. In the first case, SS-meshes were used and were then compared to an assembly of single, non-woven SS wires. In

this specific objective, a wide variety of macroscopic parameters were evaluated to achieve an optimal design.

3.2.2 Specific Objective 2

The second specific objective was to determine the effects of micro and nanoscopic features on a fog harvesting surfaces. For topological changes, th-CVD was used to grow CNT forests onto the basic SS mesh. These substrates were then tested in fog harvesting conditions and studied with respect to theory from the literature.

3.2.3 Specific Objective 3

The third specific objective was to determine the effect of surface chemistry. This objective used various surface modification techniques (PICVD, and plasma deposition) to evaluate the effects of surface topology and chemistry. For chemical assay, two characteristics were considered: hydrophobicity and hydrophilicity. Finally, scalability was evaluated through the construction of a large scale fog harvesting device.

3.3 Experimental Setups

3.3.1 Fog Harvesting Experimental Setup

Fog harvesting experiments were performed in an enclosed environmental chamber. This chamber is made of clear acrylic and has a total approximate volume of 0.1 m^3. An ultrasonic mister was used to generate fog and a flexible tube was attached to direct the fog towards fog harvesting samples. In this system, water microdroplets of 1-5 micron size are formed through the vibration of piezoelectric ceramic discs at ultrasonic frequencies [146]–[148]. Due to the high oscillation frequency of these discs, cavitation bubbles form near the disc, implode within the bulk of the

liquid creating capillary waves, also known as ripples, at the surface of the water from which microdroplets are ejected (Figure 23).

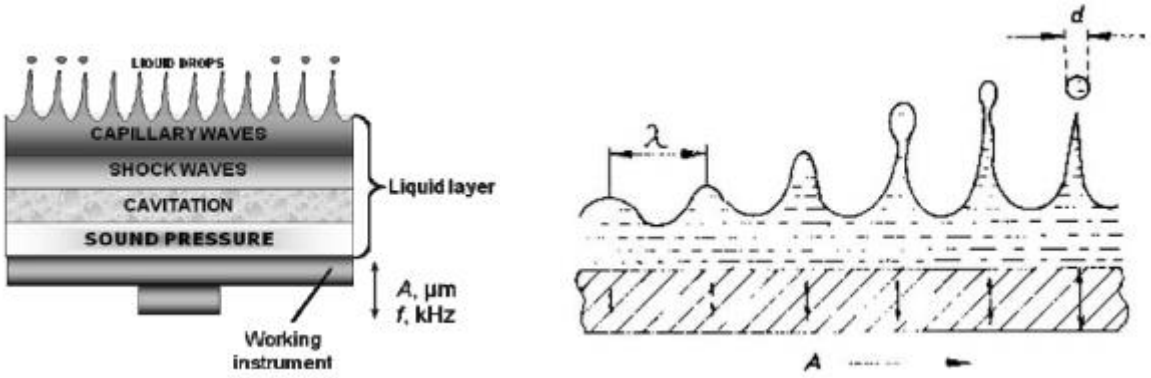

Figure 23. Microdroplet formation through ultrasonic vibration [242], [243]

The droplet sizes generated though this mechanism fall within the range of natural fog droplets [21], [25], [34], [90], [149]. Harvesting surfaces were placed directly in the fog stream, held in place with a clamp and a support stand. Water was collected in a petri dish placed beneath the harvesting surface. A fan was also placed in the environmental chamber in order to create homogeneous atmospheric conditions within the experimental volume. Before each test, the fog harvestor and empty petri dish were weighed before and after each test using an analytical balance to determine the total amount of water collected in the petri dishplaced below the harp. The ultrasonic humidifier was also weighed before and after each experiment to determine the average amount of fog generated. An average mass flow rate of 174±7 (standard deviation) grams/hour was calculated. The percentage of water collected was then calculated using the following equation:

$$\%\, water_{collected} = \frac{Weight\ of\ water\ after\ experiment}{Mass\ of\ fog\ generated} \quad (38)$$

This ensured a valid comparison between experiments rather than reporting solely the amount of water captured due to the variability of the mass of fog generated. Fog harvesting performance of each sample was also expressed as a normalized collection rate:

$$m_{collected}\left(\frac{g}{cm^2 * h}\right) = \frac{\dot{Weight\ of\ water\ after\ experiment}}{(Experiment\ duration)(Active\ surface\ area)} \quad (39)$$

In this experimental system, fog velocity was estimated based on values provided in the literature that use ultrasonic humidifiers. These values can vary between 0.15-1.6 m/s [26], [27], [30], [33], [38], [104], [150]. The reported velocity is highly dependent on the geometry of the outlet, the capacity of the device and the distance where velocity is measured. From this, fog density can be calculated:

$$Q_{fog} = v_{fog} A_{outlet} = 0.02 - 0.2 \frac{m^3}{h} \quad (40)$$

$$\rho_{fog} = \frac{m}{Q_{fog}} = 0.89 - 9.48 \, kg/m^3 \quad (41)$$

In their experimental setups, Shi et al. used an ultrasonic mister and the outlet's diameter was of 2.2 cm [33]. As mentionned previously, an ultrasonic mister was also used in this research and the outlet tube possessed a 2.5 cm diameter. Despite this discrepency, this setup resembled ours the most and therefore, due to similarities in experimental montage, 0.15 m/s was assumed for further analysis of the results obtained. Fog conditions are very rarely the same from region to region. Wind speeds and density are thus variable. It is important to note that the velocity estimated is very low when compared to natural fog that has a velocity of 1-5 m/s [21], [34], [95], [108]. Inversely, the fog density is high as fog has been reported to have densities of 0.5 g/m^3 [151]. Therefore, the results obtained can be compared to other research in the field, however to complete the picture, samples should be tested in real conditions. Each test was carried out for a total duration of 1 hour

and repeated three times to insure reproducibility of the results. Figure 24 shows a schematic of the fog harvesting setup in the laboratory:

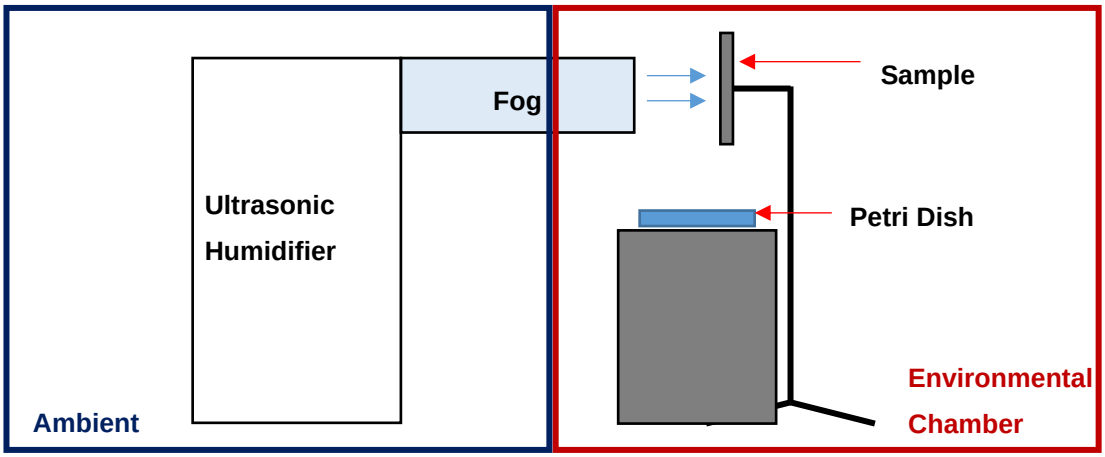

Figure 24. Fog harvesting setup

3.3.2 Fog Harvester Construction

In the literature, it has been highlighted large mesh-like nets were typically employed in fog harvesting projects. It has also been highlighted that a major drawback from this consisted in the wearability of nets over time as polymeric materials are used. For this reason, in this research project, 316 stainless steel grids of mesh sizes of 200 and 400 were initially selected as appropriate candidates. This material provides satisfactory properties to counter degradation such as high tensile strength, corrosion resistance and high Young Modulus. These key mechanical properties are significantly higher in the case of stainless steel when compared to traditional Raschel or Nylon wire fog harvesters as shown in Table 6.

Table 6. Mechanical properties of fog harvesting materials [152]

Property	**Stainless Steel**	**Polyethylene (Raschel)**	**Nylon wire**
Young Modulus	189-210 GPa	0.6-0.9GPa	2.62-3.2 GPa
Tensile Strength	480-2240 MPa	20.7-44.8 MPa	90-165 MPa

These grids consist of woven 25.4 µm SS wires with an opening size of 38.1 µm and an overall open area of 38%. These were then covered in a forest of carbon nanotubes (CNTs) to increase the surface specific area of the substrates and increase contact with incoming water microdroplets. Finally, these CNT covered meshes were functionalized using photo-initiated chemical deposition (PICVD) to modify surface wettability. It is known that there is a trade-off between water adhesion on the harvesting surface and rapid water runoff from the surface. As seen previously, hydrophilic surfaces are beneficial to enhance water capture, but hydrophobicity is then required to cause quick droplet coalescence and removal to allow for surface "regeneration". Therefore, we are looking to study the effect of wettability and surface area on fog harvesting capabilities. To achieve this, three types of SS-CNT substrates were tested: bare SS, hydrophobically and hydrophilically functionalized SS-CNT (Fig. 25).

Figure 25. SS-CNT Grid

As a secondary option, harp-like fog harvesters were designed, aimed for better fog flow aerodynamics and decreased amount of clogging of mesh pores. In this case, single stainless-steel wires were wound in the creases of two 5 cm threaded rods held together by two SS plates (Figure 26).

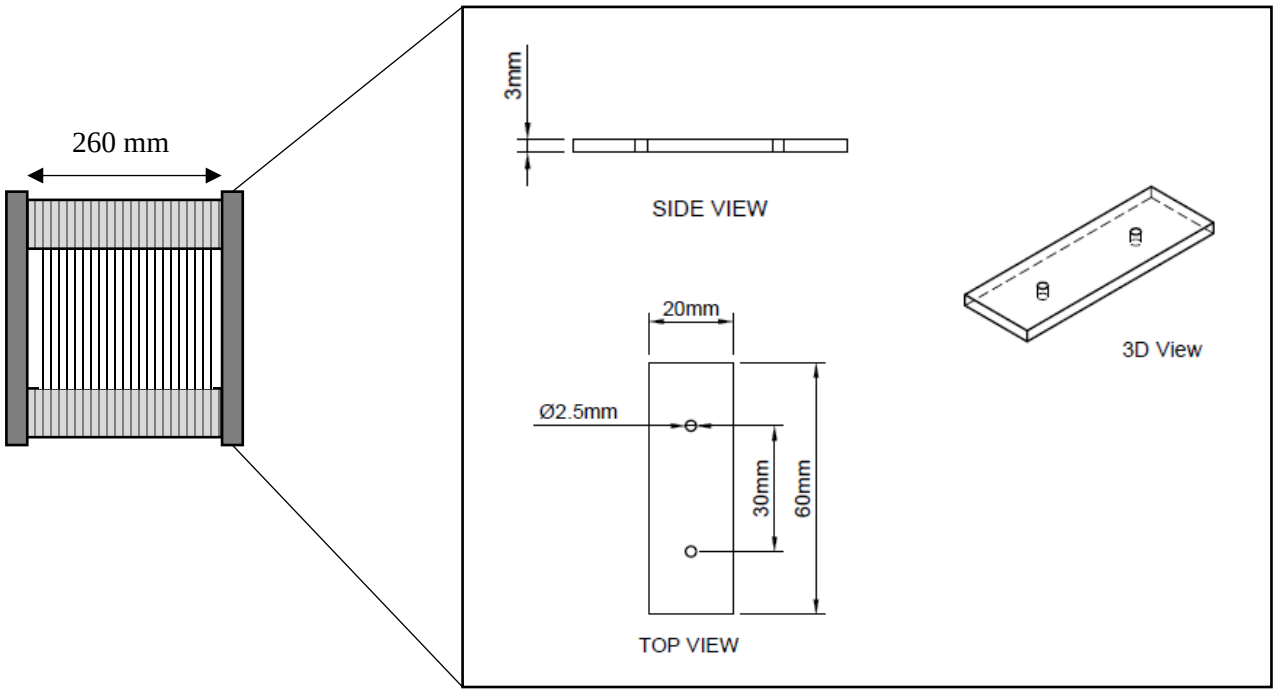

Figure 26. Design of fog harvesting harp

The length and height of the surface were set to 260 and 300 mm, respectively, such that the harps active surface area was set of 78,000 mm^3. This design allowed for a reduction of droplets clogging due to the absence of woven wires, a controllability of wire diameter and the distance between each wire (pitch). In order to achieve maximum water collection, a study to uncover the influence of a wide range of design variables was performed. Stainless steel wires with diameters (d) of 0.18 mm (0.007") and 0.64 (0.025") were tested to assess the effect of this variable on fog harvesting. The pitch and thread distance of the rods were considered to be equivalent. Hence, this value was varied between 0.4 and 1.41 mm by changing the threaded rods accordingly.

3.3.3 PICVD

The custom-made PICVD reactor consists of a quartz tube with a length of 50 cm and a 25 mm diameter illuminated by two UVC, low-pressure, germicidal lamps (Figure 27). These lamps' primary emission peak is at 253.7 nm with a weaker, secondary peak at 185nm. Total irradiance was 0.01W/cm^2 at 3.5 cm. The photo-initiator, H_2O_2 (50% w/w, Fisher Scientific) was injected into the reactor using a syringe pump (New Era Instruments) at a rate of 1 µL /hour in the case of hydrophilic treatments (or second phase of the VCG). Mass flow controllers (Brooks) regulated

the precursor gas flow, namely syngas, composed of hydrogen (H_2, 99.97%) and carbon monoxide (CO, 99.97%), and the purging gas (Ar, 99.9%). All gases were purchased from Air Liquide. Before all experiments (see parameters retained in Table 9), the reactor was purged with Ar for 3 minutes at 3 L/min. Processing was undertaken at room temperature (23°C). An increase in temperature up to ~50 °C was recorded due to the heat given off by the UVC lamps to the reactor over the 60-180-minute treatments. Each experiment was repeated three times to ensure the reproducibility and calculate the uncertainty of measurements.

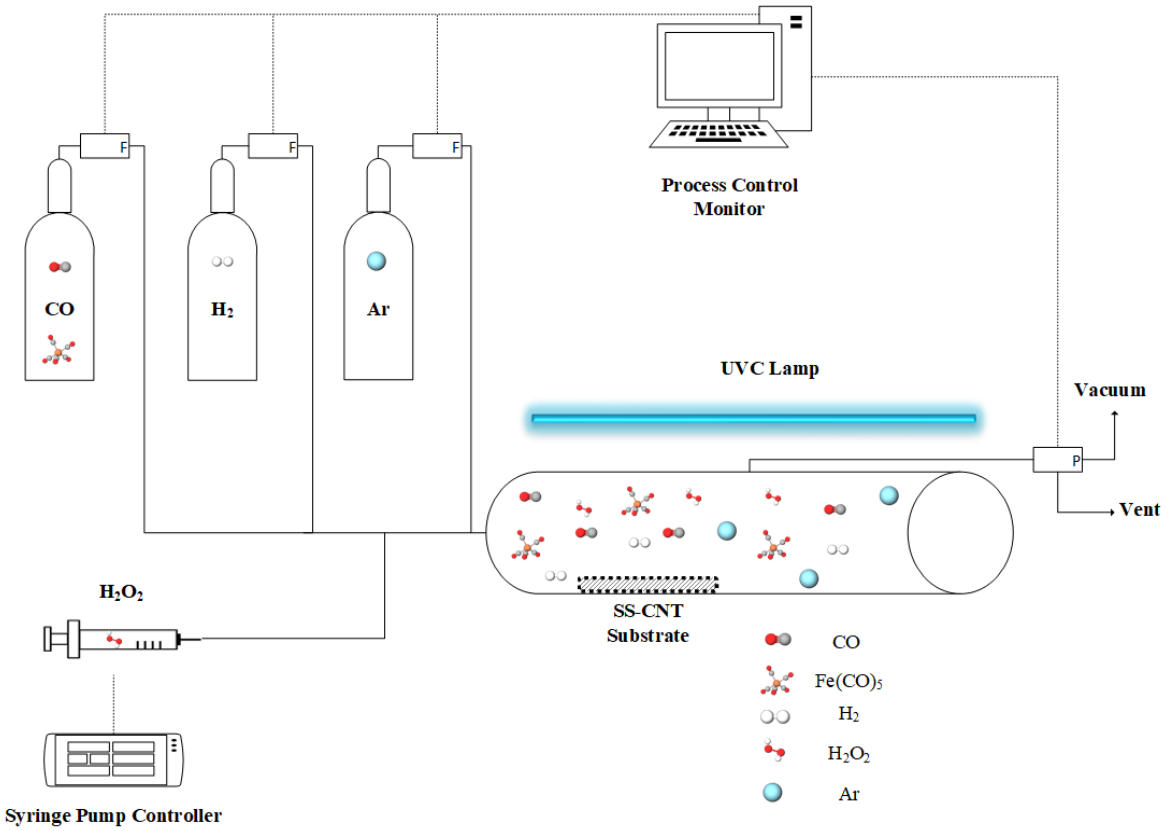

Figure 27. PICVD experimental setup

3.4 Surface Characterization Techniques

3.4.1 Contact Angle Measurement

Contact angle measurements were performed through goniometry [46], [47], [64], [153]. In this technique, solid-vapor (γ_{sv}) and solid-liquid (γ_{sl}) interfacial tension is deduced from the angle that

is formed between a drop of liquid and the surface it is in contact with. To do this, a line tangent to the outline of the liquid drop outline is drawn from the three-phase boundary or the contact line. The angle between this tangent and the surface is measured and corresponds to the contact angle. Experimentally, this is done with a vertical syringe pump, a sample stage, a lighting source and a camera. All of these components are connected to a computer for image and video analysis. Contact angle is measured through the sessile drop method wherein water droplets of selected size of 2μL are pumped out of the syringe and lowered from the top onto the substrate located on the sample stage until the droplet detaches from the syringe and adheres to the substrate. This is visualized on the computer screen through the video feed taken from the camera, enlarging the zone of interest as seen in Figure 28. The software then analyzes the image based on edge detection fitting procedures such as Laplacian of Gaussian and polynomial fitting to extract the outline of the drop and finally, measure the contact angle.

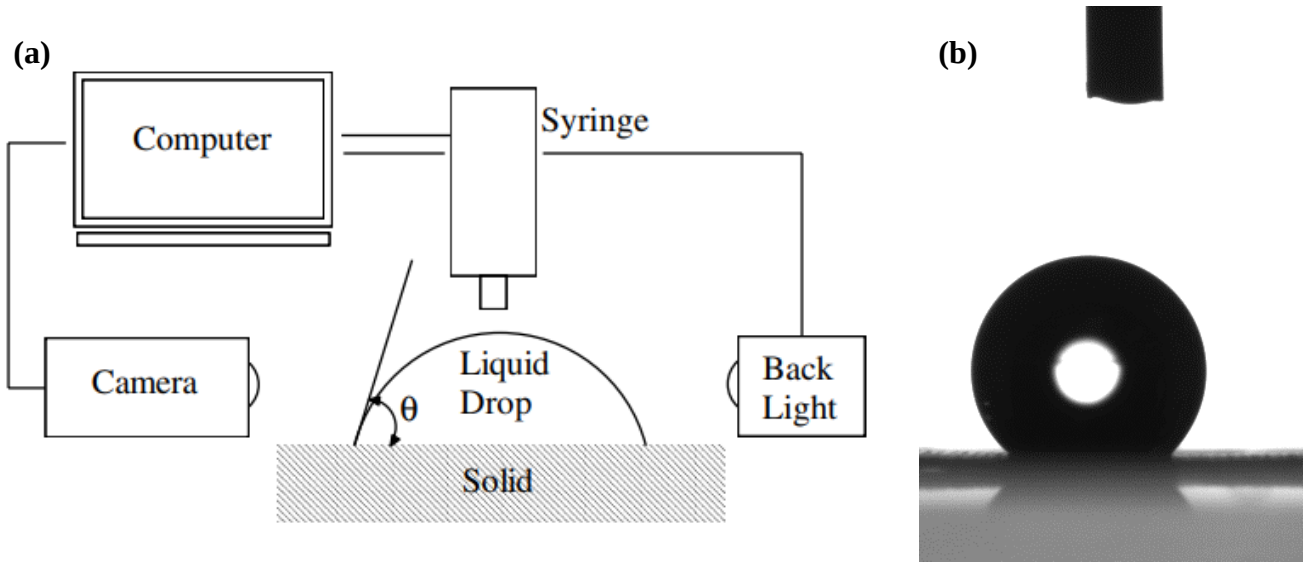

Figure 28. (a) Diagram of tensiometer setup [153], (b) Water droplet on SS-CNT surface

This method is known as the sessile or stalk drop [47]. It is important for the operator to wait a minimum of 10 seconds before measuring contact angle to allow for the droplet and surface interaction to stabilize. That being said, waiting for an extended period is not desired due to the possibility of drop evaporation which would reduce its volume and introduce errors in the measurements. Goniometry is widely considered to be the simplest and most frequently used in scientific literature. Despite its ease, the main drawback lies in the subjectivity of the instrument

operator as he/she must input the baseline where the three-phase boundary point is on the captured image [47]. This can introduce some errors depending on the substrate because of poor lighting, irregularities of the substrate or orientation where there is not a clear a definition between the drop outline and the surface. Contact angle measurements were performed on substrates before and after treatments. For a substrate, three measurements are taken on a single point and a total of three points are taken across the surface to asses homogeneity of the surface contact angle. Generally, a surfaces degree of affinity for water is categorized as hydrophilic or hydrophobic. The distinctions between each are defined by the contact angle and are expressed in Figure 29.

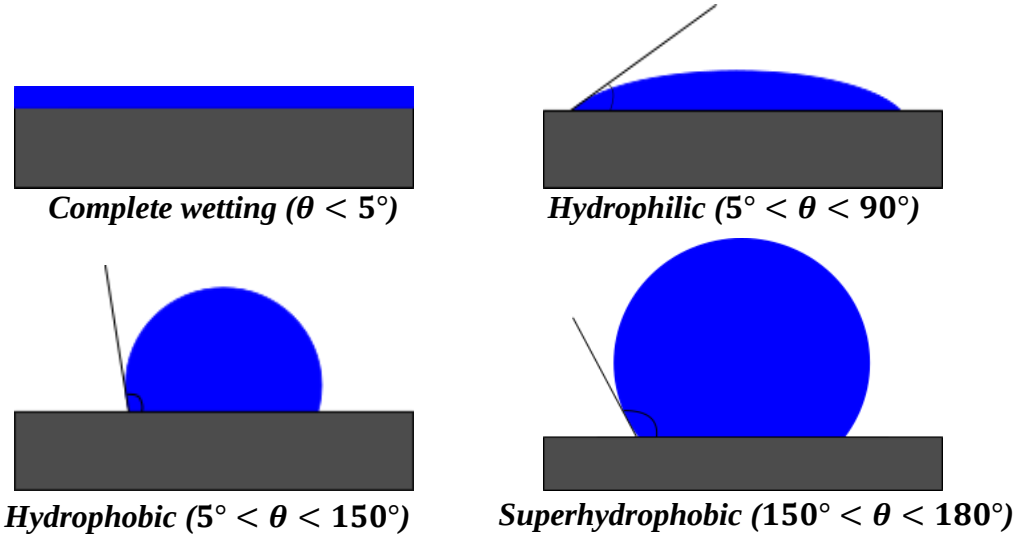

Figure 29. Schematic of surface wettability evaluated trough contact angle with a surface

3.4.2 X-Ray Photoelectron Spectroscopy (XPS)

For chemical characterization of modified surfaces, X-Ray Photoelectron Spectroscopy was used. This technique employs x-ray excited photoelectrons to deduce surface elemental composition [154], [155]. Photoelectrons are generated by an X-ray source, Al Kα (1486.6 eV) in this case, and sent towards the sample surface [154], [156], [157]. Atoms present within the first 2 to 10 nm of the surface then absorb the photoelectron which provokes the ejection of core secondary electrons out of the surface. These exit with a kinetic energy (E_k) equal to the difference between incident photon energy (hv) and the energy needed to displace them. The required energy corresponds to

the sum of binding energy (E_b) and the work function (ϕ) – the difference between the Fermi level and Vacuum level.

$$E_k = hv - (E_b + \phi) \quad (42)$$

The variable of interest in this technique is the binding energy which is specific to bonds between different atoms.

$$E_b = hv - (E_k + \phi) \quad (43)$$

Thus, ejected secondary electrons are directed towards a detector where they are sorted and counted according to their binding energies. This process is schematized in Figure 30. This process is done under vacuum to remove any chance of collisions between electrons and gas molecules that would induce energy loss and introduce errors in the measurement.

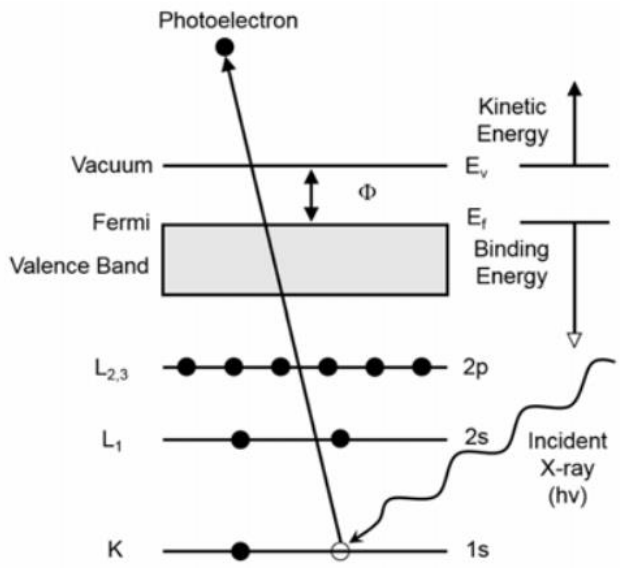

Figure 30 Schematic of XPS principle [156]

XPS was used to characterize the surface elemental composition of treated SS-CNT substrates.

3.4.3 Scanning Electron Microscopy (SEM)

Scanning electron microscopy (SEM) was used as an imaging technique to gain insight into the density and analyze surface topology of substrates used in this project. This technique, like XPS, scans the surface by bombarding it with electrons [158]. Electron sources can be thermionic or field-emission guns (FEG). The former consists in heating a refractory material to the point where

electrons can overcome the potential barrier that hold it to the solid. The latter employs the strength of an electric field to concentrate on a fine point of a material where electrons are then ejected from the material. Thermionic sources are typically used in SEM and use tungsten as the refractory material. Electrons are accelerated through 1-30kV corresponding to wavelengths between 40-1000pm. Upon emission from the source, electrons are then focalised towards a specific point by passing through a series of magnetic condenser lenses. When electrons interact with matter, a multitude of events may occur such as scattering, transmission, cathodoluminescence, Auger emission and secondary electron emission. Like XPS, collisions of the incident electrons with core atoms of the surface can cause the ejection of secondary electrons (SE) out of the surface that will be collected and analyzed. SEM allows for magnification between 10-500 000x. Figure 31 shows all the components of a SEM as well as electron interactions with the specimen. SEM was used in this project to observe the surface structure of SS-CNT substrates.

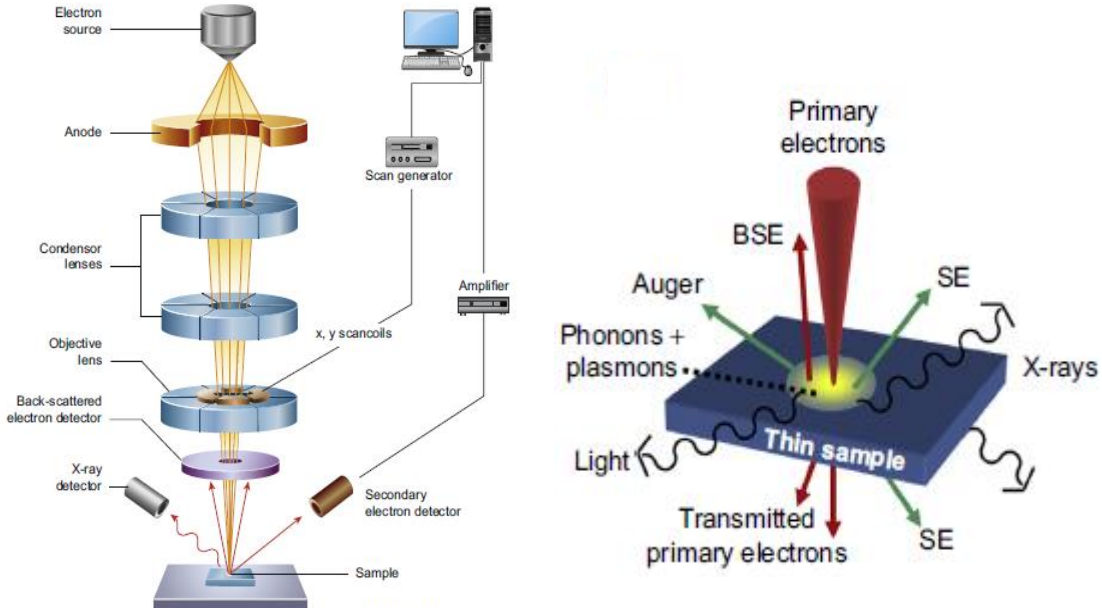

Figure 31. Schematics of scanning electron microscope and electron interaction with sample. [158]

While evaluating surface chemistry, superhydrophilic surfaces exhibited high hydrophobic recovery. In fact, days after a PICVD superhydrophilic treatment, the SS-CNT substrates reverted back to their hydrophobic nature through hydrophobic recovery. This is an aging issue where polar functional groups deposited via PICVD are lost at the surface through diffusion and reorientation towards the bulk of the deposition. This greatly affected the repeatability and overall consistency

of experimental fog harvesting results with SS-CNT substrates. The need for superhydrophilic samples with higher stability led to the development of a PICVD method to reduce this ageing phenomenon. The method relied on the generation of a vertical chemical gradient by which a first layer of highly crosslinked deposition helped maintain polar functional groups at the surface. In fact, cross-linking ensured to lock polymer chains in place and reduce the free volume within the bulk so as to both reduce the rotational movement of groups along the C-C backbone of previously free polymer chains and hinder the diffusion of loose polar groups back into the bulk of the deposition. This is method is presented in the following chapter.

CHAPTER 4 ARTICLE 1: SUPPRESSION OF HYDROPHOBIC RECOVERY IN PHOTO-INITIATED CHEMICAL VAPOR DEPOSITION

Alessio Aufoujal[1], Ulrich Legrand[3], Jean-Luc Meunier[4], Jason Robert Tavares[2]

[1] Polytechnique Montreal; alessio.aufoujal@polymtl.ca

[2] Polytechnique Montreal; jason.tavares@polymtl.ca

[3] Polytechnique Montreal; ulrich.legrand@polymtl.ca

[4] McGill University; jean.luc.meunier@mgcill.ca

Published in mdpi Catalysts: Special Issue "Photocatalysis and Environment" on May 12th 2020

Abstract: Photo-initiated chemical vapor deposition (PICVD) functionalizes carbon nanotube (CNT) enhanced porous substrates with a highly polar polymeric nanometric film, rendering them super-hydrophilic. Despite its ability to generate fully wettable surfaces at low temperatures and atmospheric pressure, PICVD coatings normally undergo hydrophobic recovery. This is a process by which a percentage of oxygenated functional group diffuse/re-arrange from the top layer of the deposited film towards the bulk of the substrate, taking with them the induced hydrophilic property of the material. Thus, hydrophilicity decreases over time. To address this, a vertical chemical gradient (VCG) is deposited onto the CNT-substrate. The VCG consists of a first, thicker highly cross-linked layer followed by a second, thinner highly functionalized layer. In this article, we show through water contact angle and XPS measurements that the increased cross-linking density of the first layer can reduce the mobility of polar functional groups, forcing them to remain at the topmost layer of the PICVD coating and suppressing hydrophobic recovery. We show that employing a bi-layer VCG suppresses hydrophobic recovery for 5 days and reduces its effect afterwards (contact angle stabilizes to 42±1° instead of 125±3°).

Keywords: Hydrophobic Recovery; Photochemistry; Superhydrophilicity; Homogenous catalysis

4.1 Introduction

Special wettability surfaces such as superhydrophobic, superhydrophilic and heterogeneous or patterned wettabilities have gained significant interest since the development of surface modification techniques [54], [76], [159]–[161]. Patterned wettability research focuses on combining both superhydrophobicity and superhydrophilicity on a single surface such that it can benefit from both repellent and spreading properties of each. This can be done two-dimensionally, creating patterns such as lines or shapes on a given substrate that express the opposite behaviour as the remaining, untreated part of the surface. Yu et al. showed an example of this by first spraying a superhydrophobic coating of silica poly(dimethyl siloxane) (PDMS) onto a substrate, creating a hydrophobic background [28]. Then, a superhydrophilic layer of platinum (Pt) was deposited via pulsed laser deposition (PLD) using a grid mask. This yielded patterned wettability surfaces having a hydrophilic background with hydrophobic micro bumps, mimicking the shell of *Stenocara gracilipes*, a beetle that uses this surface texture to capture fog from the atmosphere [28]. Superhydrophilic surfaces on their own have also gained industrial interest for anti-fogging, microfluidic and heat transfer applications [161]. Another important application for superhydrophilic surfaces lies in their anti-fouling properties. Although the mechanism behind biofouling formation is a complex process, it has been demonstrated that overall fouling decreases with high surface energy surfaces, associated with hydrophilic behaviour. High affinity between surface and water molecules generates films on these surfaces [54], [162], [163]. Hence, interactions between fouling agents and the surface are limited. One major drawback is the low stability of such superhydrophilic surfaces, reducing fouling prevention in the long-term. As an example, fouling has been linked to marine applications such as the growth of microorganisms on the submerged surface of ships. Current remediation techniques include the use of biocides. However, this type of substances cause environmental damage [164], [165].

Generally, extreme wettability features can be achieved through the modification of surface topology, tailoring surface chemistry of a material or a combination of both these techniques can prove effective [166], [167]. Superhydrophilic surfaces obtained via chemical approaches suffer from a key drawback: in many cases, artificially induced superhydrophilic surfaces lose their wettability over time resulting through a phenomenon known as hydrophobic recovery [42], [143],

[168]–[170]. This process can occur as soon as minutes or hours [171]. This has been observed extensively for plasma-modified polymers and plasma polymer films (PPF) [172]–[176]. Hydrophobic recovery has been linked to different mechanisms:

(1) rearrangement and reorientation of polar functional groups at the surface [42], [143], [168], [177];

(2) diffusion of the low molecular weight chemical groups from the outer surface towards the bulk of the deposited polymer [178]–[180];

(3) oxidation and degradation reactions occurring at the surface over time [178]–[180]; or

(4) surface roughness changes or adventitious external contamination [143]–[145].

These mechanisms can co-exist within a single polymer layer and are mostly dependent of material properties such as the mobility of the polymer chain, the degree of cross-linking of the polymer structure, the chemical composition of the polymer and any additives that may be present. External factors also influence hydrophobic recovery such as the polarity, temperature and pressure of the storage environment of the samples [172], [174], [180]–[182]. Polymeric molecules in a thin layer have a degree of freedom to move and may change conformations at the interface with another medium to reduce their interfacial energy. Polarity of the outer medium has been found to dictate surface reorganization. In water, a surface will tend to expose its polar components and push their non-polar ones into the bulk of the polymer. The inverse scenario is observed in the case of storage in air. This conclusion has been seen on several polymers such as polyethylene (PE), poly(ethylene terephthalate) (PET) and silicon rubber [143], [183], [184].

A technique that has been shown to reduce hydrophobic recovery in plasma polymer films (PPF) is the use of vertical chemical gradients (VCG) [174]–[176]. Namely, Hegemann et al. have designed PPFs that possess vertical chemical gradients such that a highly-functional film layer is deposited over a stable, less-functional one [176]. The purpose of the first layer is to prevent the reorientation of functional polymer chains at the surface as well as the diffusion of polar functional groups towards the bulk of the substrate. This was done using a capacitively coupled plasma reactor with an ethylene (C_2H_4) and carbon dioxide (CO_2) precursor mixture. By varying this gas ratio, they obtained the desired double layered thin PPF [176], [185]. Similarly, Li et al. deposited a

bilayer of plasma polymerized heptylamine (PPHA) [186]. In this case, they combined two plasma polymerization modes, continuous and pulsed, to obtain cross-linking in one layer and functionality in the second, respectively. Although the results achieved through these methods are promising, the scalability and energy intensity of plasma processing can hinder further development towards the application of stable hydrophilic thin films. Building on this past work done in the field of plasma science, we thus turn to the usage of low-cost and sustainable ultraviolet (UV) energy, a key component leading to reactions in plasma. UV exposure usually photodegrades polymers, observable through loss of color and embrittlement of the material [187]. This irradiation causes polymer chain scission and reorganization in the form of cross-linking of polymer chains. These chemical cross-links effectively reduce the flexibility of a polymer molecule, stiffening the structure, reducing the polymer chain mobility and ultimately limiting the mobility of smaller molecules [188], [189]. We employ this relationship using a chemical vapour deposition (CVD) gas phase technique that uses UVC light to initiate a free radical polymerization of photoactive monomers, using a gas-phase homogeneous photocatalyst. Compared to plasma-enhanced or thermally activated CVD, this photo-initiated CVD (PICVD) is performed at atmospheric temperature and pressure greatly reducing processing cost and energy usage, thus increasing scalability and sustainability of the technique [190]. Typically, PICVD requires a careful selection of initial reaction mixture based on their capacity to polymerize onto a substrate either through self-polymerization or with the help of photo-initiators [191]–[194]. The selection of monomer precursors depends on the desired properties of the produced thin films. Examples of such monomers include styrene, vinyl esters, vinyl ethers, acrylics and methacrylics [191], [194], [195]. It has been used in to produce a variety of polymeric films such poly(2-hydroxylethyl methacrylate) (pHEMA), poly(methyl methacrylate) (PMMA), polydivinylbenzene (PDVB), poly(glycidil methacrylate) (PGMA) and several others [191], [192], [194]. In this work, the precursors consists of a syngas mixture of carbon monoxide (CO), hydrogen (H_2), a photo initiator, hydrogen peroxide (H_2O_2) and trace amounts of iron pentacarbonyl ($Fe(CO)_5$). Iron pentacarbonyl is formed in trace quantities (0.02-6.7 ppm) from the reaction of CO and the steel walls of its storage cylinder, and serves as a homogeneous photocatalyst [196]. Through photo-initiated reactions within the gas mixture, a thin oligomeric film is formed on the substrate surface.

Inspired by current advances in reducing hydrophobic recovery in plasma processes, we impose a VCG by which a first highly cross-linked layer is deposited onto carbon nanotube forest grown on stainless steel grids (SS-CNT) followed by a second, highly functional layer. CNTs were selected because prior research has demonstrated they can be readily be functionalized over a wide range of surface energies using PICVD [197]. This work aims to demonstrate a simple method increasing stability in superhydrophilic thin films. This novel approach is deemed of interest due to the simplicity of the technique when compared to plasma processing or solvent based ones. PICVD uses common and accessible materials (CO, H_2 and H_2O_2) as well as low energy UVC lamps to perform surface treatments and, in the case of this study, suppresses the effects of aging on superhydrophilic samples – which is in itself an issue that is encountered by many in the literature. This makes this technique a highly scalable one. Furthermore, superhydrophilicity is shown here to be maintained over increased time scales. Achieving stable superhydrophilic coatings in this fashion can prove to be beneficial for the industrial purposes described previously. Typically, hydrophobic recovery occurs within a short time frame from hours to days. In this work, we propose a strategy and insight that drastically improve stability in superhydrophilic thin films. To the best of our knowledge, VCG has never been shown in thin film deposition techniques other than capacitively coupled plasma polymerization. In this research article, a vertical chemical gradient strategy employing PICVD films to reduce the effects of hydrophobic recovery on SS-CNT substrates is described.

4.2 Results

4.2.1 Surface Modification

Previous work on functionalization via PICVD has shown that a full range of surface wettabilities, from superhydrophilic to superhydrophobic, can be achieved by modifying process parameters such as pressure, gas volume ratio H_2/CO , sample position and photo-initiator flow rate [190], [197], [198]. The effects of these parameters on the wettability of the deposited polymer film are summarized in Table 7.

Table 7. PICVD processing parameters effects on surface wettability

Process Parameter	Effect on Wettability
Pressure (P)	Increase in pressure decreases wettability ($\theta \propto P$) [197]
Photo-initiator (n_{PI})	Presence of a number density of photo-initiator increases wettability ($\theta \propto \frac{1}{n_{PI}}$) [197]
Position (x)	Wettability is increased when the sample position is near the reactor inlet ($\theta \propto \Delta x_{inlet}$) [197], [198]
Treatment duration (t)	Increase in treatment duration decreases wettability ($\theta \propto \frac{1}{t}$) [197]
Gas Ratio (R)	Increase in gas ratio decreases wettability ($\theta \propto R$) [197]

From these relationships, processing parameters were selected to achieve hydrophobic, super-hydrophilic and VCG depositions (Table 8). The concept of VCG has already been explored in the context of plasma polymerization and, to translate this approach to a PICVD context, we first deposit a thicker hydrophobic layer for 120 minutes. Previous studies demonstrated, through XPS and TOF-SIMS, that this polymeric film chemically resembles phenol formaldehyde resin, with a highly cross-linked structure [125]. For the following 60 min, PICVD parameters are changed by decreasing the pressure to 15 kPa and adding hydrogen peroxide (H_2O_2) at a flow rate of 1mL/min. These conditions correspond to a hydrophilic treatment and are meant to incorporate oxygenated functional groups in the top-most layer of the polymer film. A schematic of the VCG procedure is shown in Figure 32.

Table 8. PICVD process conditions to grow hydrophobic, hydrophilic and VCG coatings.

Wettability	Pressure (kPa)	Flow Rate (ml/min)	Gas Ratio (H_2/CO)	Time (min)	H_2O_2	Immediate Average Contact Angle
Hydrophobic	15	600	0.14	60	No	125±3°
Hydrophilic	-15	600	0.14	60	Yes	<5°
VCG	15/-15	600	0.14	180	No/Yes	<5°

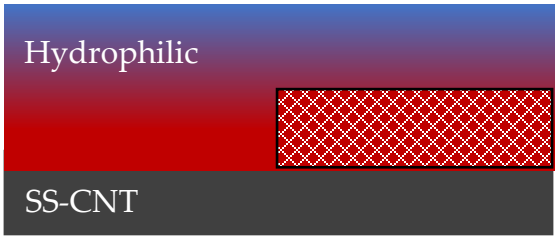

Figure 32. Schematic of PICVD Vertical Chemical Gradient formed by a cross-linked hydrophobic layer beneath a hydrophilic coating.

4.2.2 Effect of Storage Conditions

The native contact angle of SS-CNT is 124°±2 (Table 10). Immediately following hydrophilic PICVD treatment, this value drops to <5°. This shows a complete transition from hydrophobic to superhydrophilic. As highlighted previously, one key mechanism for countering hydrophobic recovery relies on the stability of polar surface groups, which can be affected by storage conditions. Figure 33 highlights that the storage medium does not affect contact angle evolution in the first few days. However, after the tenth day, a clear separation is observed between both sample groups. Samples stored in water and air stabilize at contact angles of 50±4° and 105±7°, respectively, after 2 months (Table 9). This suggests that long-term storage in a polar medium helps slow down hydrophobic recovery (by approximately half) but is not sufficient to maintain superhydrophilic behaviour beyond 1 day. This can be explained by the fact that, over time, polymer chains containing polar functional groups can reorient and diffuse back towards the surface to be stabilized by dipole-dipole attraction with polar water molecules surrounding the surface, effectively

stabilizing the water contact angle [173]. This result is in accordance with Labonté et al., who observed increased stability of PICVD treated polystyrene beads upon storage in water [171]. Other works on PPFs have shown that polymer degradation is possible when stored in a polar medium. This can occur through diffusion of water molecules into the film, leading to swelling or hydrolysis reactions with the polymer causing dissolution of the film into the bulk of the medium [174]. This, however, was not observed in the case of PICVD films. If dissolution occurred, an increase in contact angle towards the initial CNT value should be observed. In the case of air, hydrophobic functional groups are favored near the surface in order to reduce the surface energy [199]. Looking at the evolution of contact angle in Figure 33, a sharp increase occurs during the first days, eventually reaching a maximum. Afterwards, this value decreases and stabilizes to a final value after 2 months. This behaviour has been previously observed in plasma polymerized surfaces [142], [170]. It can be explained as a competition between restructuring and reorientation of surface chains and oxidation reactions with ambient air.

Table 9. Water contact angle after 2 months

Sample	**Contact angle after 2 months (°)**
Bare SS-CNT	123±3°
Air-stored hydrophilic SS-CNT	105±7°
Water-stored hydrophilic SS-CNT	50±4°
VCG SS-CNT	42±1°

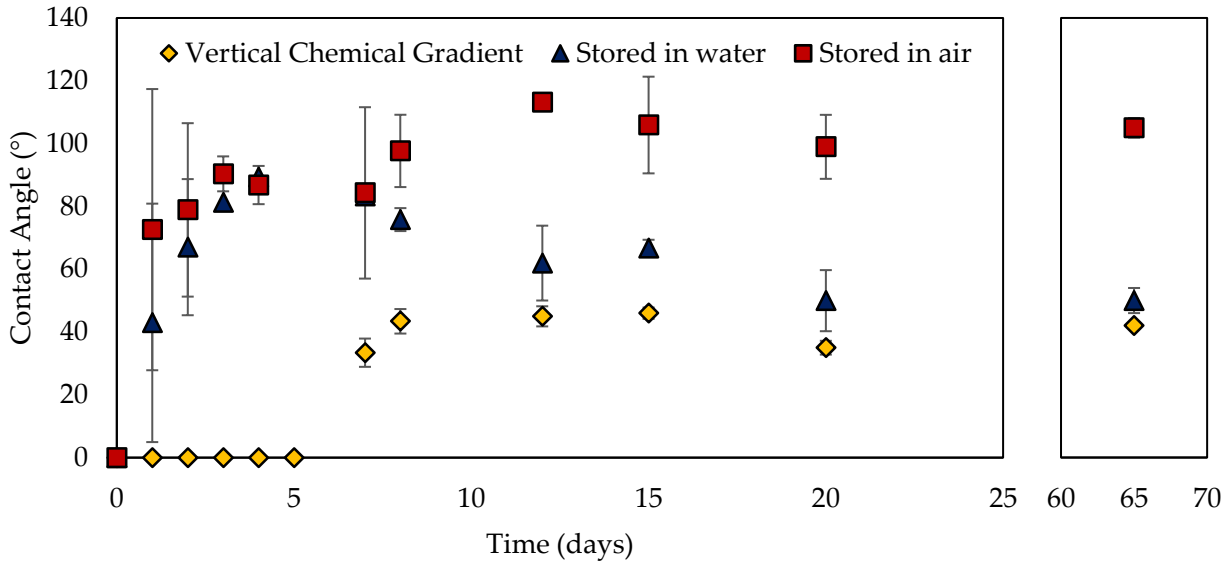

Figure 33. Contact Angle Aging of PICVD Treatment on SS-CNT Samples

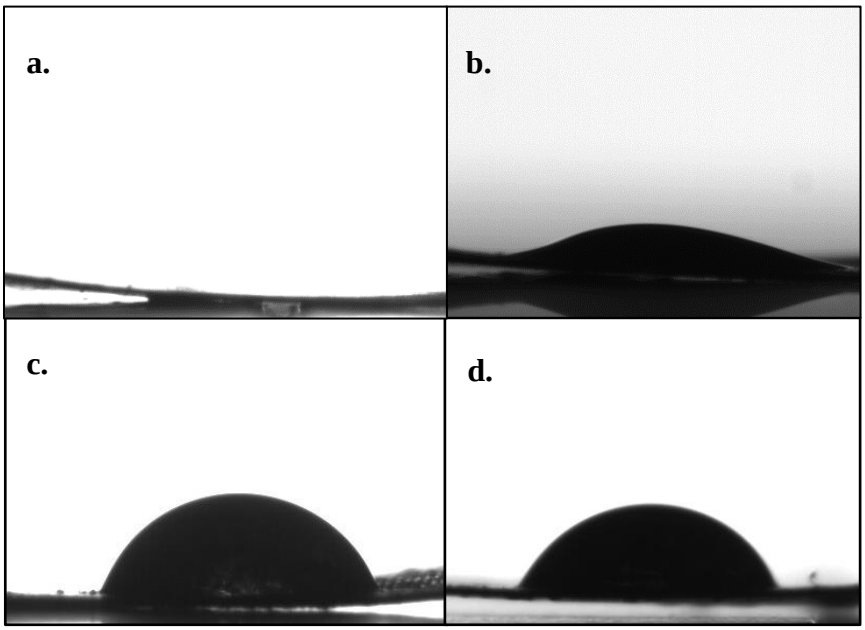

Figure 34. Water contact angle on SS-CNT VCG treated samples, obtained through goniometry at a. Day 0, b. Day 6, c. Day 15 and d. 2 months after treatment

In the first stage of contact angle evolution for samples stored in both air and water, surface reorganization is the dominant mechanism [23,54,55]. Hydrophilic functional groups located at the surface will tend to move towards the bulk, increasing the surface contact angle. This causes the contact angle to steeply increase in the first days post-functionalization. At the same time, oxidation reaction with atmospheric oxygen introduces oxygen on free radicals still present on the surface. This results in the incorporation of oxygenated groups at the surface that will cause the contact angle to steadily decrease until full stabilization. This corresponds to the second stage, where, in the case of hydrophilic and VCG treated films, contact angle slowly reduces towards a new equilibrium point. This stabilization process is also a function of diffusivity of polymer chains in the film, which decreases with increasing cross-linking. Due to the slow deposition rate and the presence of UV light in PICVD, crosslinked structures are formed throughout the treatment [51,54,55]. This may also play a role in the slow diffusivity of polar groups extending the time needed to stabilize at the surface. Finally, the stability of the contact angle measurements taken on treated SS-CNT samples implies that PICVD polymer films are not removed by surface interactions with water. This is also an indicator that the polymer structure has strong links with the SS-CNT substrate near the base of the film and the functional groups it contains near the surface. It has also been shown in previous work that PICVD coating bonds covalently with a variety of substrates. On silicon wafers, for example, Farhanian et al. evaluated Si-C bonds through high resolution XPS of both carbon and silicon [50].

4.2.3 Effect of Surface Chemistry

By depositing a VCG film rather than purely hydrophilic, we observed that hydrophobic recovery was effectively suppressed for 5 days before wettability begins to decrease (Figure 33). θ following VCG-PICVD stabilizes to 42±1° after two months of aging in air (Table 10). The stability of the film is likely due to the successful deposition of a highly cross-linked hydrophobic layer, enhanced by the longer deposition time and UV curing when compared to pure hydrophilic films. In VCG samples, this allows for a trapping of oxygenated functional groups at the surface and limiting their capability of reorienting or diffusing towards the bulk.

XPS was performed to correlate surface chemistry with the degree of hydrophobic recovery. Looking at the high resolution peak fittings of carbon C1s, four functionalities are observed at

different binding energies: (1) 284.6 eV, associated with carbon sp^2, (2) 285.7 eV, corresponding to carbon sp^3, (3) 286.5 eV corresponding to carbon single-bonded to oxygen (C-O) and (4) 288 eV, which is indicative of carbon double-bonded to oxygen (C=O) and pi-pi* transition [157]. These binding energies are likely due to the incorporation of hydroxyl (-OH) and carboxyl (-COOH) groups representative of the oligomeric structure of the PICVD polymer film. Three functionalities are identified in the high-resolution O1s peaks: 529.8 eV, 531.6 eV and 533.0 eV associated with metal oxide, oxygen double-bonded to carbon and oxygen single-bonded to carbon (Figure 35c) [157]. In hydrophilic and VCG treated samples, we observe distinct O-Fe and C=O peaks compared to hydrophobically treated ones (Figure 35a). This, paired with the overall increase of oxygen in the film, indicates a successful incorporation of oxygen-containing functional groups such as O-Fe, C-OH, -COOH and C=O. This result is also valid for VCG treated SS-CNT samples. This result shows how the topmost layer of VCG films behaves hydrophilically for a longer duration of time than purely hydrophilic films.

The XPS analysis is reinforced by studying the near-surface oxygen-to-carbon ratio [O]/[C] (Figure 36): the [O]/[C] only decreases 30% over 2 months for the VCG sample, whereas it drops by 51% and 86% for hydrophobic and hydrophilic samples, respectively. Upon closer investigation of the Fe content in the films, we notice similar behaviour as for oxygen. Looking at Fe, peaks appear at 710.9 eV, and 726 eV. These correspond to $Fe2p_{3/2}$ and $Fe2p_{1/2}$ [157]. Furthermore, the coupling of the Fe peaks situated from 710.8-711 eV and O1s peaks at 529.8 is indicative of the formation of iron oxides such as α-Fe_2O_3 or γ-Fe_2O_3 [155], [200]. Similarly, Fe peaks at binding energy of 711.5 eV coupled with two distinct O peaks at 529.9 and 531.6 eV is associated with the formation of FeOOH [155], [200]. Overall, Fe seems to be present under its different oxidation states in the films.

By analyzing Figure 35a and the elemental atomic percentages in Table 10, hydrophobic recovery can be observed in all samples, indicated by the decrease of O over 2 months and the increase of C content at the surface. The difference lies in the starting amount of O in the films. As a reference, a hydrophobically PICVD treated SS-CNT sample was prepared. Analyzing the XPS surveys for all three samples shown in Table 11, two major difference can be noticed: increase in O content and appearance of Fe peaks between 700 and 740 eV. For all three substrates, O incorporation is associated with the formation of oxygenated functional groups mainly from $Fe(CO)_5$, H_2O_2 and

partly from the CO precursor. The addition of H_2O_2 and decrease in pressure is therefore causing the observed increased O content in hydrophilic and VCG films. We observed a low relative atomic percentage of Fe on the surface because of the introduction of $Fe(CO)_5$ in the PICVD reaction. Interestingly, these two observed features disappear simultaneously after 2 months of storage (Figure 35b). These moieties seem to play an important role in the degree of hydrophilicity of the final surface.

In the hydrophobic reference case, very little O was incorporated into the polymer film as expected and a 49.3% decrease was measured after 2 months. For hydrophilic samples, this value is 79.7%, indicating the reversion from a hydrophilic, wettable surface back to a hydrophobic surface. In the case of VCG samples, O contained near the surface of the film decreased by 25.4%, displaying an increased retention of O resulting in a higher stability in the hydrophilic PICVD treatment and a delayed or decelerated hydrophobic recovery.

Table 10. Chemical Composition of samples obtained through XPS Survey

Sample	**C1s**			**O1s**			**Fe2p**		
	Day 0	**Day 1**	**2 months**	**Day 0**	**Day 1**	**2 months**	**Day 0**	**Day 1**	**2 months**
Hydrophobic	94.3%	-	97.2%	5.3%	-	2.71%	0.4%	-	0.11%
Hydrophilic	84.8%	-	97.6%	11.7%	-	2.38%	3.5%	-	0.07%
VCG	81.9%	79.6%	87.7%	14.9%	17.8%	11.1%	3.2%	2.6%	1.14%

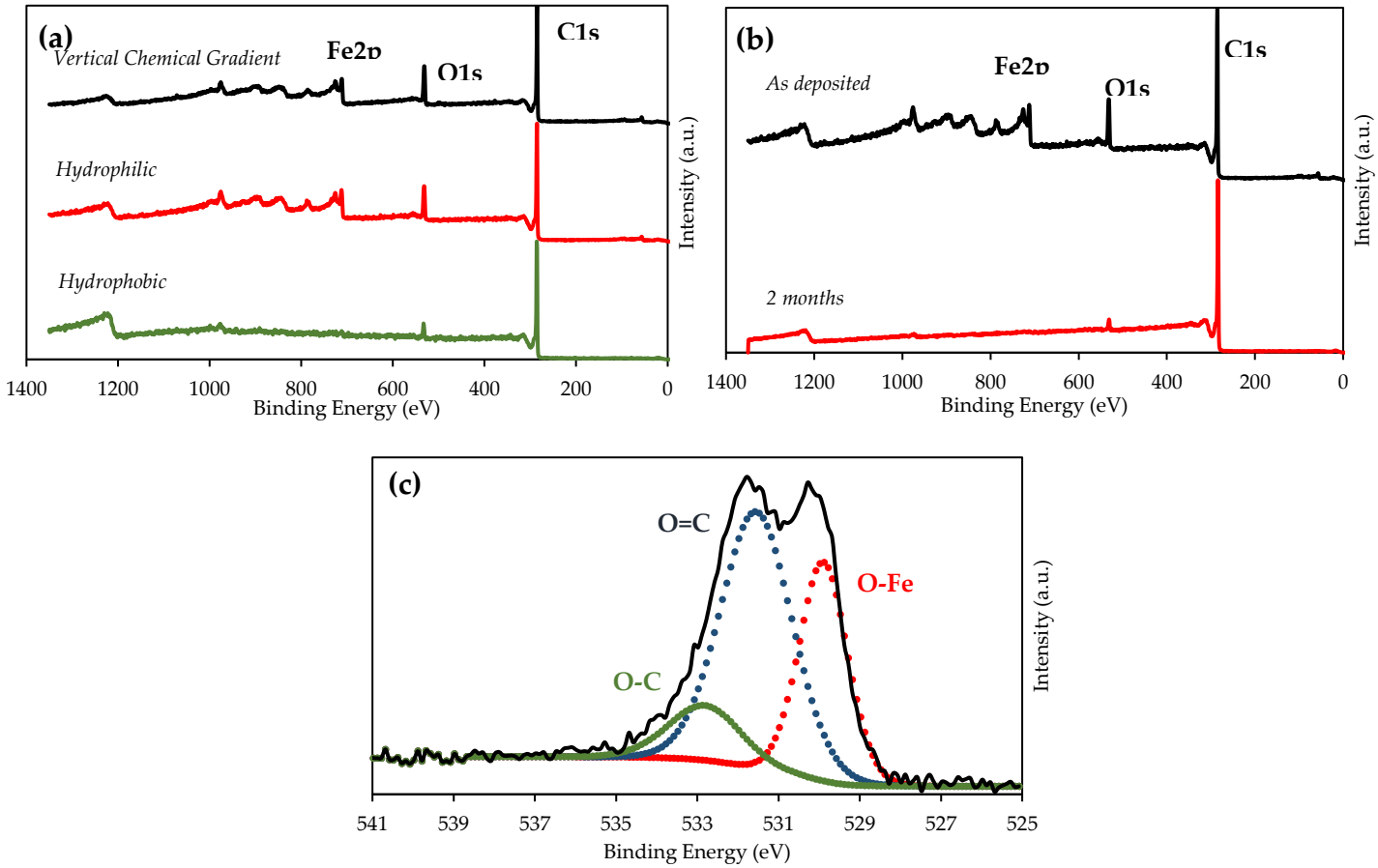

Figure 35. (a) XPS surveys for PICVD treated samples as deposited, (b) Hydrophilic XPS survey as deposited and after 2 months, (c) High Resolution O1s of hydrophilic samples.

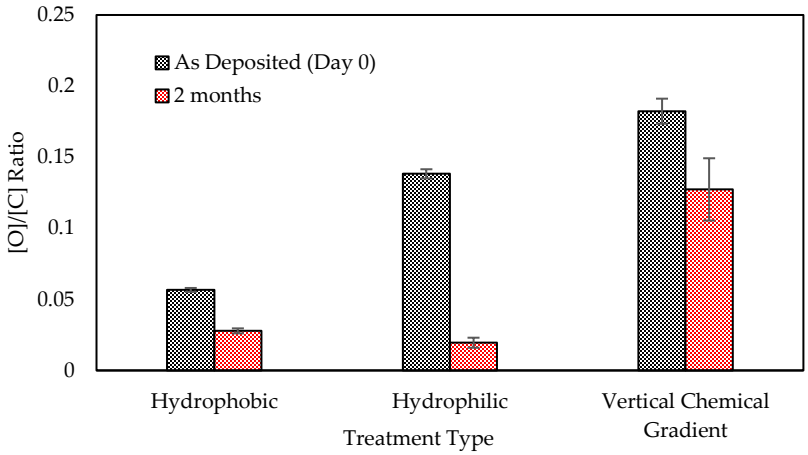

Figure 36. Aging of the coating observed thanks to [O]/[C] ratio of PICVD treated SS-CNTs as deposited and after 2 months.

4.3 Discussion

Oxygen is incorporated into the film through the various functional groups attached to the polymer chains. The decrease in the [O]/[C] ratio must then be due to reoarganization of these chains at the air interface, since functional groups do not spontaneously detach from polymers. These oxygenated groups experience both short and long-range effects based on their immediate surroundings such as neighbouring groups, nature of the substrate and the external media. Thus, their orientation is a crucial factor in the resulting wettability. When oxygenated moieties are facing away from the bulk, a surface will appear more hydrophilic [201]. Short-range motion such as chain rotation around polymer backbone is driven by both long range attraction to other oxygen contained within the bulk and repulsion from the air interface [201]. This alone, however, is not responsible for the decrease in O near the surface as storage in a polar medium would counter this short-range restructuring. Previous theoretical and simulation work has been done to gain a better understanding on polymer chain mobility in thin films. Generally, macromolecular mobility, namely diffusion, is enhanced near the surface as well as non-attractive solids [202]. There are several explanations for this such as an enrichment of chain ends or lower chain packing density near the surface and the non-polar substrate [202], [203]. In this study, this diffusion can be observed in all treatment types and storage mediums through the decrease in oxygen. For samples stored in air, mobility would therefore be enhanced at the air-film interface due to the repulsive

nature between these two mediums. However, in VCG samples, the [O]/[C] suffers less of a loss in oxygen compared to hydrophobic and especially hydrophilic ones. This is likely due to the fact that cross-linking in the base layer hinders the mobility of oxygenated groups and encourages the hypothesis that a higher degree of cross-linking is achieved in the VCG samples. Cross-linking in polymer thin films can occur through several mechanisms depending on compounds and functional groups contained within the film. One way cross-linking occurs is through hydrogen bonding, which can occur between hydroxyl and carboxyls inside PICVD thin films [204]. Metal coordination can also occur to between iron ions incorporated by the $Fe(CO)_5$ precursor and polar functional groups in the polymer structure. It has been found that these metal-ligand interactions were stable at room temperature. However, these noncovalent interactions disappear at slightly higher temperatures (30°C). this also hints to the increased mobility of Fe. In PICVD,cross-linking via UV irradation (photocross-linking) also occurs. As polymer chains are formed in the film, they may grow through addition with a neighbouring chains [205]. However, in radical polimerization, the high density of reactive radicals formed under UV favor intermolecular and intramolecular reactions. These lead to a highly cross-linked product. In this case, dimerization of carboxyl groups may occur resulting in the attachment of two indivudual polymer chains [206]. Additionally, through these processes, radical trapping in restrained spaces in the cross-linked structure may occur due to steric hinderance [205]. These may be radicals that are bonded to the bulk structure or alone. This adds to the fact that post treatment mobility can occur through radical conversion of these loosely bonded groups. In this case, oxygen found near the surface layer is reduced. Another parameter that influences photocrosslinking is irradiation time. Previous studies on photocrosslinking have shown that increased irradiation time significantly reduced oxygen permeability [206], [207]. As cross-linking increases within the polymer structure, rotational movement of functional groups around the C-C backbone is significantly reduced due to the additional bonding that effectively restrict this type of movement [201]. Diffusion within the PICVD film also depends on the free volume within the film [208]. Increased open space within the polymer matrix therefore leads to a higher amount of O diffusion. It is well known that cross-linking within the polymer structure reduces the free volume and as a result limits the segmental mobility.

Despite the current inability to maintain superhydrophilic quality of VCG samples, employing the bilayer strategy increases the hydrophilic stability window for 5 days. Similar works have shown stabilization in hydrophilic regions. It is, however, difficult to compare the results obtained in this study with other work due to the variability in surfaces and methodology. In our work, starting with carbonaceous material that is intrinsically hydrophobic, we have shown a drastic change in wettability (~100% decrease from native value). In PICVD deposited films, superhydrophilicity is achieved through the incorporation of a high number of oxygenated groups that adsorb and grow on the substrate. This is also enhanced by the high surface area of the CNT forest. This allows for a higher amount of available hydrophilic sites onto which water can spread once the deposition is made. From this modified state, hydrophobic recovery does not appear until 5 days later. Such results have been demonstrated with PDMS thin films by Vlachopoulou et al [209]. In an inductively coupled plasma reactor, they were able to achieve completely wetted surfaces by first generating nanostructures through etching with sulfide hexafluoride (SF_6) plasma followed by a functionalization step in O_2 plasma. This technique produced completely wetted surfaces (<5°) that lasted for 7 days. They have found that nanostructuring the surface was an important factor in suppressing hydrophobic recovery [209]. This leads us to believe that a similar phenomenon occurs with SS-CNT surfaces that are intrinsically nanostructured. The degree of hydrophobic recovery can be expressed as the total increase of contact angle from an initially functionalized surface relative to the angle at which it stabilizes once the effect of recovery is no longer observed. When looking at the degree of hydrophobic recovery, VCG samples start from <5° and stabilizes at ~42° after 1440h. From this perspective, it seems as though hydrophobic recovery is still a dominating phenomenon upon its onset. This value, however, also depends on the starting contact angle of a surface post-functionalization. Looking at Rupper et al., for instance, hydrophilic Si wafers with contact angles that aged from approximately 41 to 45° after 5000h were produced by applying VCG PPFs [185]. Although the degree of hydrophobic recovery is only of 9.8%, the hydrophilicity achieved after treatment is lower when compared to the results presented in this study. The surface modification is more pronounced in the case of SS-CNT substrates, going from approximately 120° to <5°, corresponding to almost 100% reduction in contact angle, whereas the native contact angle of argon cleaned Si wafers (~70°) is reduced by 41.4%. Past preliminary observations on hydrophobic recovery of PICVD hydrophilic films on high density polyethylene

(HDPE) extrusion nets show that full hydrophobic recovery is always achieved for samples stored in air [198]. Seeing as this is also the case for SS-CNT substrates, this shows that the nature of the substrate is not sufficient to minimize the degree of hydrophobic recovery and that the chemical nature of the polymeric film itself is dominant. This is further shown with VCG samples, where the chemistry differs in the deposition, and storage in air leads to improved stability. Previous PICVD studies have used polystyrene (PS) beads [171]. Interestingly, hydrophilicity was maintained for a longer duration using SS-CNT substrates when compared to hydrophilically treated PS beads that were also stored in water. This further shows how the nanostructuring of a surface may help reduce the degree of hydrophobic recovery on a surface.

$Fe(CO)_5$ also appears to play a significant role in the behavior of PICVD generated films. This compound is formed from the reaction of CO with the steel walls of the CO gas cylinder. It is known that Fe and Ni carbonyls can form over extended periods of time at low temperature and high pressure [196], [210]–[212]. For a photochemical reaction to occur, a compound must satisfy two conditions. First, there must be an overlap between the spectral emission of the light source and the absorption spectrum of the targeted molecule. Second, the absorbed photon must have enough energy to initiate the reaction. Incidentally, $Fe(CO)_5$ absorbs light in the UV spectrum and has a bond dissociation energy of 55 kcal/mol corresponding to 519.84 nm (in other words, light with shorter wavelengths has sufficient energy for bond scission) [181], [213]. Therefore under 253.7 and 185 nm light, it loses its CO groups through photofragmentation to form reactive intermediates such as $Fe(CO)_4$, $Fe(CO)_3$ and $Fe(CO)_2$. These intermediates react in the gas phase with other species such as -OH radicals, generated through photodissociation of H_2O_2 forming a wide variety of compounds. These finally adsorb onto the substrate and react with C and O groups, as well as other surrounding Fe compounds to form secondary and tertiary oxides [125], [196]. Previous analysis of this compound in our experimental setup found that it is present in the reaction mixture between 0.02-6.7 ppm [196]. Despite these low quantities, it is clear from the results obtained that the $Fe(CO)_5$ acts as a homogeneous photocatalyst that is crucial to the development of stable PICVD coatings, especially in the hydrophilic case. The lack of controllability of this compound stands out as an important aspect to improve upon in the future. Its catalytic properties have been extensively studied in the past. Water gas shift, olefin isomerization, direct liquefaction and alkene hydrogenation reactions are some examples of the use of $Fe(CO)_5$ as a catalyst [214]–

[216]. In the case of water gas shift reactions, for instance, reaction rates have a proportional relationship with $Fe(CO)_5$ concentration [217], [218]. Additionally, a reduction in activation energies was also reported. In this work, an increase in $Fe(CO)_5$ concentration results in a higher formation of iron carbonyl radicals and increase the reaction rates for -OH generation, . Upon photodissociation, secondary and tertiary iron compounds can catalyze photo-Fenton reactions with H_2O_2 [219]. Thus, hydroxyl radical generation is accelerated through the addition of $Fe(CO)_5$. This is particularly interesting considering that Fe content in hydrophobic PICVD films is lower than in hydrophilic ones. Seeing as no H_2O_2 is present in hydrophobic treatments, iron carbonyls present in the reaction mixture exhibit less catalytic behavior.

Furthermore, Fe atoms that have been incorporated into the polymer film also appear to leave the surface after 2 months, as shown in the XPS spectrum. Basic diffusion can result from concentration gradients and in this case, it would be possible that Fe diffuses back into the bulk of the film to achieve a lower energy state – equilibrium [220]. This is possible considering the low amount of Fe found in hydrophobic coatings, generating a gradient between the top layer of the film and the bulk. As a hydrophilic film transitions from hydrophilic to hydrophobic, Fe can thus dig its way as a result of diffusion and reorientation mechanisms commonly responsible for hydrophobic recovery. Transition metal diffusion into polymers has been investigated by many research groups typically in the field of microelectronics [221], [222]. However, there is uncertainty whether metals truly diffuse into polymers or rather agglomerate [221]. Briefly, metal-metal cohesive energy is generally two orders of magnitude higher than that of polymers. This favors metal-metal interactions rather than metal-polymer mixing [221]. Thus, agglomerates are expected to be formed at equilibrium conditions. Faupel et al. have studied the interaction of copper (Cu) in polyimide films through XPS and noticed a decrease in Cu intensity after annealing [222]. In this case, diffusion was ruled out in favor of Cu clustering and the decrease of intensity was attributed to inelastic scattering of photoelectrons in the newly formed agglomerates [222]. This exemplifies the difficulty in assessing the metal-polymer interactions appropriately. In our case, however, we observed, for hydrophilic coatings, that Fe peaks can no longer be seen after 2 months. It therefore seems as though diffusion is the major mechanism at play since the decrease in Fe is quasi-total. This can be explained through Gibbs free energy. Generally, higher cohesive energy results in high surface energy [221]–[223]. For metal particles, Gibbs free energy is lower when it

is surrounded by other metals or polymer molecules compared to when it is situated at the air interface. (i.e. as deposited). Thus, it is possible that Fe atoms diffuse below the top layer into the bulk when the surface tension of the metal is higher than the sum of both polymer surface tension and metal-polymer interfacial tension [221]. As mentioned previously, polymer cohesive energy is considerably lower than metal, resulting in lower polymer surface tension. Therefore, both Fe and polymer compounds look to interact with other Fe compounds first, then with polymer, then with air. However, it is possible that Fe atoms are still pulled inwards due to long range Van der Waals force stemming from the fact that there is more polymer in the bulk that near the surface [221]. The loss of Fe may therefore come from a combination of both diffusion towards the bulk of the film and, possibly, agglomeration, effectively lowering the intensity observed through XPS.

4.4 Materials and Methods

4.4.1 CNT Growth

Type 316 stainless steel (SS) meshes (400 mesh size) were purchased from McMaster-Carr. Direct growth of carbon nanotubes (CNT) on stainless steel meshes was done by thermal chemical vapour deposition following methodology developed from the past work of Baddour et al. and Hordy et al. [224], [225]. The SS grids were cut into 2.5 by 8 cm strips and ultrasonically cleaned in an acetone bath for 10 minutes. These were then inserted into preheated 700°C furnace. The furnace was first purged with Argon (Ar, 99.9%) for 5 minutes at a rate of 3.14 L/min to remove any oxygen present. Subsequently, Ar flow was reduced to 0.592 L/min and acetylene (C_2H_2) was introduced at a flow rate of 0.068 L/min for 2 minutes. C_2H_2 flow was stopped and the furnace allowed to stagnate for 2 minutes (corresponds to the CNT growth phase). The reactor was then purged with Ar at 3.14 L/min for 5 minutes and the stainless steel grids covered with CNT (SS-CNT) were removed from the furnace [225].

4.4.2 Surface Characterization

Surface contact angle (θ and surface energy were measured with an FDS OCA-20 tensiometer (Dataphysics, Germany). For this, water droplets of 1 μL, grown at a rate of 0.1 μL/s, were deposited directly on level samples. This was performed at 3 different regions and repeated 3 times to calculate the average θ.

X-ray photoelectron spectroscopy (XPS) was done using a Thermo Scientific K-Alpha system with an aluminum X-ray source on 400 μm size area. A first survey scan was done on each sample to determine the elements present. This was then followed by a high resolution (HR) pass in order to obtain detailed spectra for both carbon (C 1s) and oxygen (O 1s).

4.5 Conclusions

This work has shown that hydrophobic recovery can be delayed from 0 to 5 days post-PICVD functionalization by using a vertical chemical gradient within a polymer film. It is assumed that this gradient starts as a hydrophobic, heavily cross-linked structure near the substrate and slowly shifts towards a less cross-linked oxygenated layer near the environment exposed surface. This has been proven on SS-CNT substrates, chosen for their high specific surface area that can eventually be beneficial in a wide range of applications. It would be important to push this work to achieve full stability over an extended to illimited period. To do this, it would be necessary to study the nature of the PICVD film, especially, its cross-linking density through swelling tests, From there, it would be pertinent to look more closely at the cross-linking within the polymeric deposition by employing common photo-crosslinkers such as benzophenone in the photo-initiated process or studying the kinetics of photo-curing during and post-illumination, which can give crucial insight into the cross-linking density. We also observe Fe incorporation in the thin film, likely originating from Fe pentacarbonyl formation in the CO gas cylinder, that is known to be photo active under UVC irradiation and thus should play an important role in the process. A control of the insertion of this compound in the system is important to study in future work. This work presents a first step to studying the repression of hydrophobic recovery in PICVD treated surfaces. The degree to which this phenomenon should be suppressed will likely depend on the intended application. Taking anti-fouling as an example, increased free surface energy is required to limit the growth of microorganisms on surfaces. In the case of ships, submerged in water, hydrophilic and VCG samples show potential in maintaining a good degree of hydrophilicity. This is especially true because hydrophilic states are more stable in polar solutions such as water.

CHAPTER 5 FOG HARVESTING EXPERIMENTAL STUDY

5.1 Laboratory Scale

5.1.1 Mesh Harvesters

SS-CNT samples were tested in fog harvesting as a first design iteration. This was done because it was hypothesized that surface texturing could be beneficial for fog collection efficiency, as stipulated in the literature, and well-defined protocols exist to adjust the wettability of CNTs by PICVD. The superhydrophilic nature of the substrate helps reduce the barrier for nucleation and increases the amount of water droplets that are caught by the fog harvester. Azad et al. have found that superhydrophilic surfaces displayed better fog collection due to the formation of a thin film across the surface which aided water transport rather than clog the surface porosities. Thus, the combination of topological and chemical modifications was hypothesized to yield an improved collecting substrate.

However, in Figure 37, it is observed that fog harvesting performance increases with hydrophobicity. This also shows that hydrophilicity increases water retention on the surface, acting as an additional limitation for shedding. This can be seen in the images of Figure 38. On hydrophobically treated SS-CNTs, droplets have low affinity with the surface and tend to form small spherical droplets across the surface that grow until their weight overcomes the adhesion force with the surface. On superhydrophilic surfaces, a film of water can be seen rather than droplets. Looking at the side view of each substrate, drops assume different shapes depending on the functionalization. For hydrophobic samples, water is pulled down by gravity, giving it a pear-like shape whereas a more symmetric shape is seen for superhydrophilic samples. This is attributed to the wettability of the latter substrates that pull water towards themselves against gravity.

Despite the effect of wettability on capture, both capture percentage and water collection rate were found to be surprisingly low in all scenarios. This is attributed to the clogging of the meshes. As the mesh is intrinsically porous, it is likely that the spacing between the woven wires gets filled with water. This can happen when drops coalesce amongst themselves and grow to a size above the dimensions of the pores and capillarity. This increase the contact between water and the substrate which, in turn, increases the adhesion force. This implies that a larger amount of liquid must be accumulated to overcome gravitational forces and onset the detachment of the drop. The negative influence of clogging as exemplified here is undeniably important because the best result, obtained with a hydrophobic material is significantly lower than results from the literature that are generally in the range between 1-5 g/cm^2-h. That being said, there are severe discrepancies between experimental setups and methodology throughout the literature. Further insight into this comparison are presented in Chapter 6.

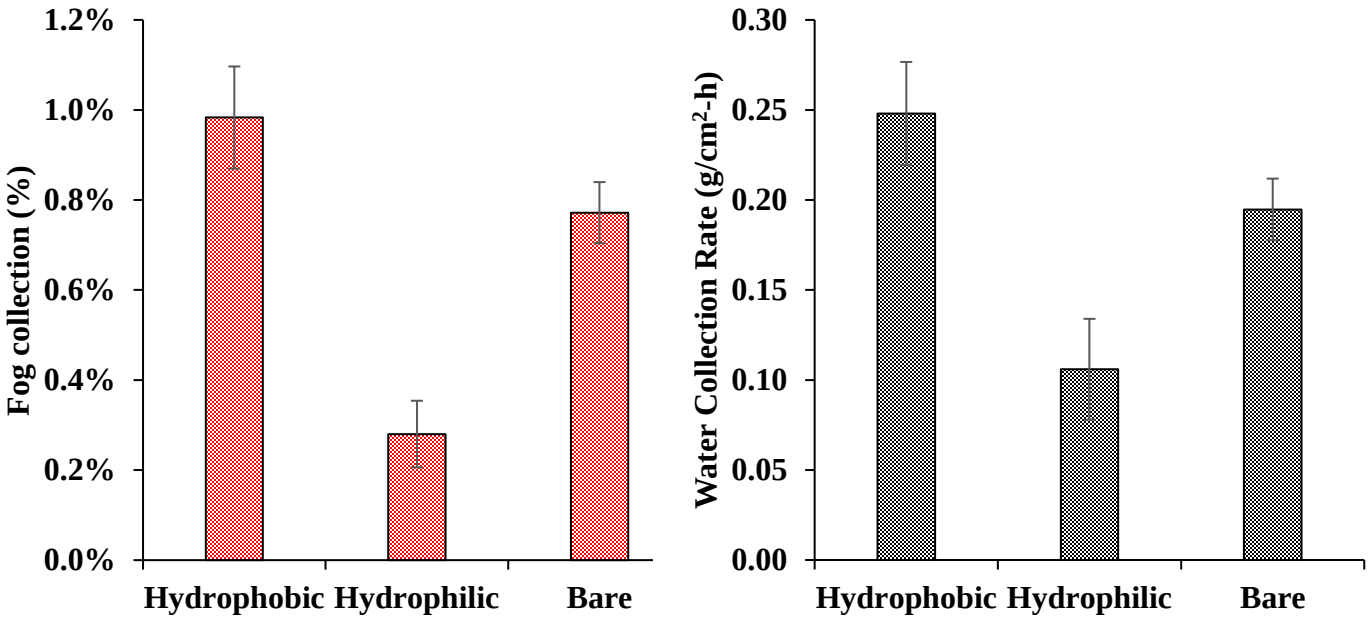

Figure 37. Fog collection and water collection rate as a function of SS-CNT wettability

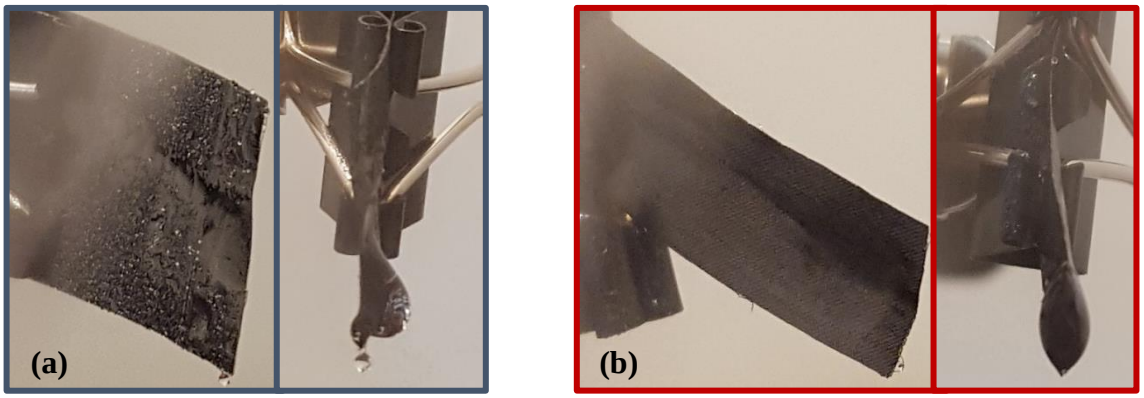

Figure 38. Fog harvesting with (a) hydorphobically and (b) hydrophilically functionalized SS-CNT mesh.

5.1.2 Harp Harvesters

As an alternative fog harvesting design, harps were constructed to compare the SS-CNT meshes to vertically aligned array of wires. Preliminary assessment shown in Figure 39 showed that the latter presented more promising fog collection results than the former. In fact, fog through the usage of harp-like configuration, fog collection rate was increased approximately 7 times. Thus, a study aimed to optimize several parameters involved in the design of the harps was undertaken to improve upon the initial iteration.

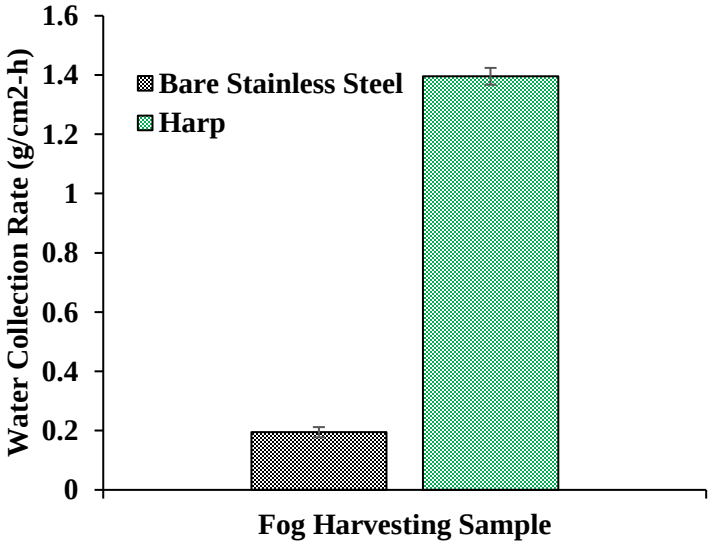

Figure 39. Fog collection rate comparison between mesh and harp geometry fog harvesters.

5.1.2.1 Influence of Tilt Angle (θ_{tilt})

The effect of tilting angle (θ_{tilt}) was assessed by rotating in the plane perpendicular to fog flow between 0 and 40° (see Figure 41). It was hypothesized that by tilting the harps, an increase in performance would be observed. This is because by offsetting the angle, we are effectively creating a single point of conversion for captured water droplets simply due to gravity. In these experiments, water microdroplets adhere to the harp wires, grow, coalesce and trickle down the SS wire until it reaches the base of the frame. It is in this last step, once water has reached the threaded rod at the base of the frame, that tilting will have an influence. In the case of a 0° angle, the harp is vertically straight, water droplets will hang under the wire on which it traveled. Gravity alone will force the droplet to detach and be collected. This will occur when its weight overcomes its adhesive forces with the threaded rod. Droplets will reach this critical weight either through the addition of water coming from incoming fog or coalescence with other droplets at the base. Here, we are looking at a force balance between water normal adhesive work and gravity.

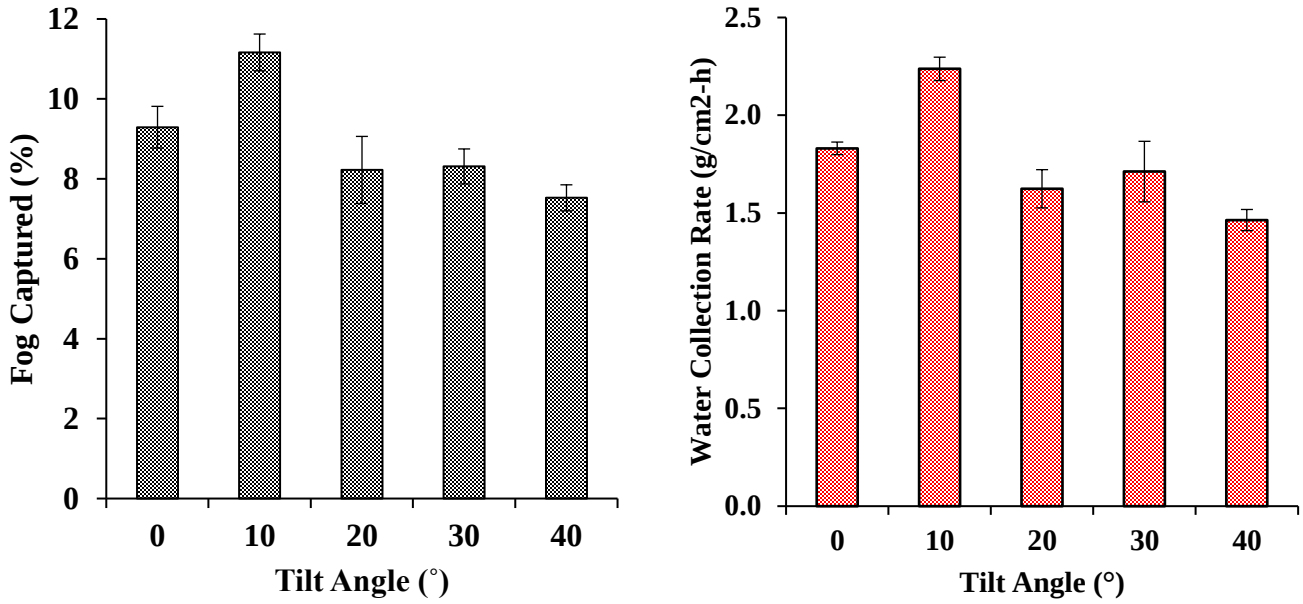

Figure 40. Fog collection and water collection rate as a function of tilting angle.

On the other hand, at extreme inclinations, droplets would no longer be able to slide down the wire. From Figure 40, it is observed that an increase in both fog capture and collection rate increase by increase in the angle from 0 to 10° followed by a decrease onwards. The 10° tilt gave optimal results, capturing 11.2±0.5 % of fog with a rate of 2.24±0.06 g/cm^2-h. Hence, this variable was set for the remainder of the study.

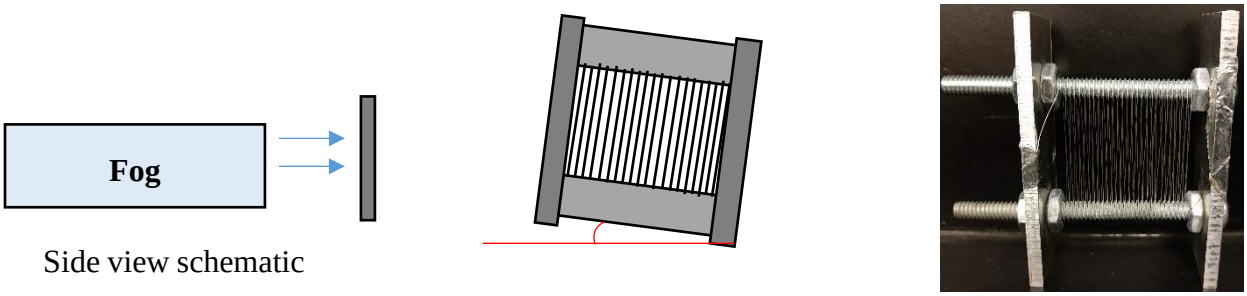

Side view schematic

Front view schematic

Figure 41. Side and front view schematic of harp tilting.

5.1.2.2 Influence of wire diameter (d)

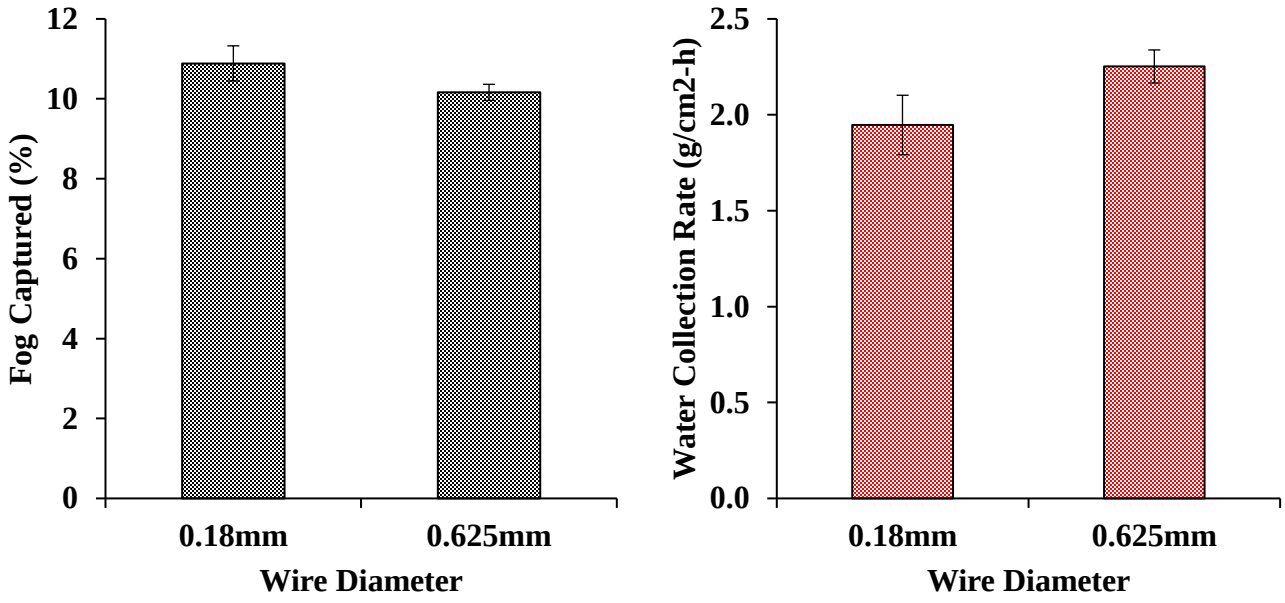

Figure 42. Fog collection and water collection rate as a function of wire diameter

We can see from Figure 42, that, considering the standard deviation, wire diameter does not seem to have a strong impact on both the fog captured and the collection rate. This is contrary to conclusions emitted by the litterature. Generally, the relationship between wire diameter and water collection rate depends on the deposition efficiency (η_d) that represents the ratio of droplets that are deposited on the harp wires and the total amount of incoming fog droplets. For a single wire, this value is calculated with the Stokes number, defined as the ratio between the fog droplet response time to that of the flow around the SS wire.[31] Equations 26 and 27 were used to plot the deposition efficiency and the Stokes number as a function of wire diameter.

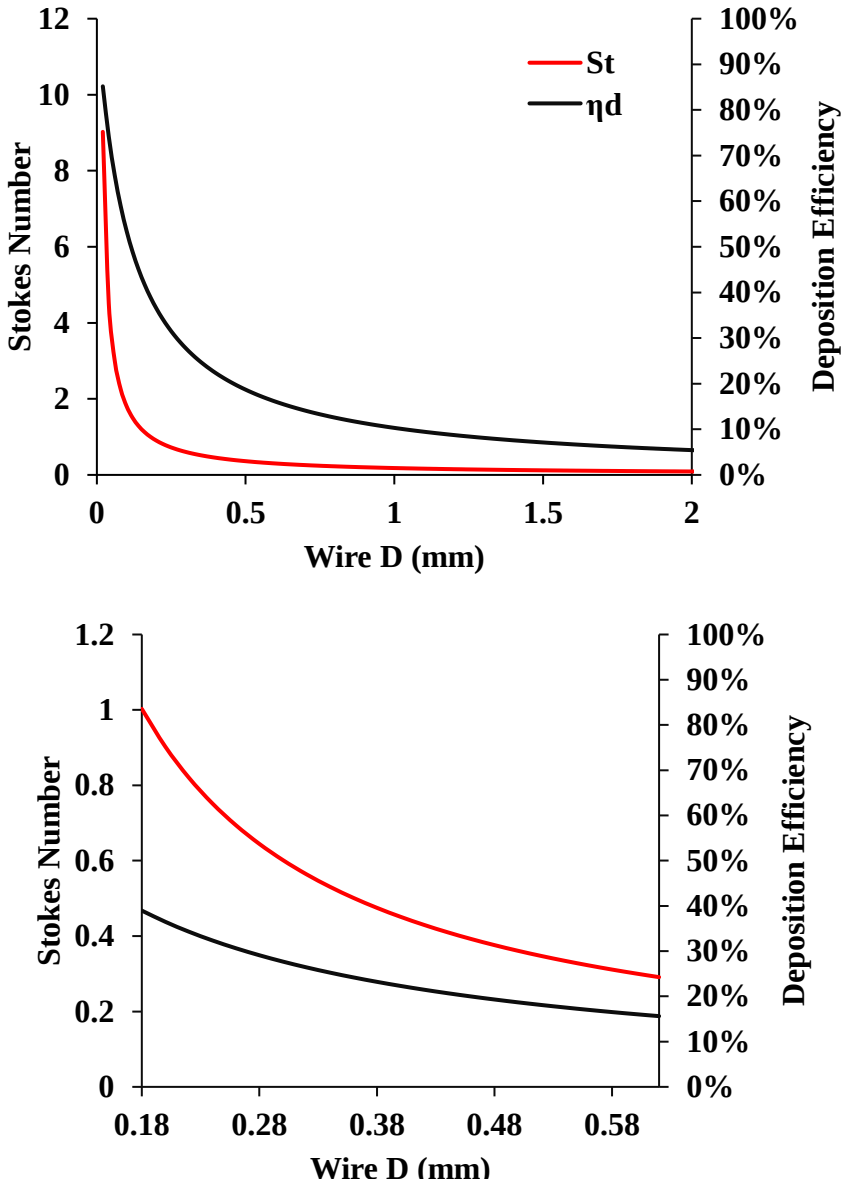

Figure 43. Stokes number (red) and deposition efficiency (black) with respect to wire diameter

Looking at the region between 0.18 and 0.625mm in Figure 43, we see a decrease from 1.00 to 0.31in the Stokes number and 39.0% to 15.63% in the deposition efficiency. From this evaluation, a smaller wire diameter would seem to provide better fog harvesting capabilities. This is the main conclusion that has been shown in the literature for single wire studies. This, however, is not reflected in the results obtained in Figure 42 as very little difference was observed between the tested diameters. One reason to explain this result resides in the fog or wind speed. For both Raschel

and SS meshes coated with a hydrophobic formulation, (1.7wt% polyhedral oligomeric silsesquioxane and 98.3 wt% poly(ethyl methacrylcate)), developed at MIT (identified as sample MIT-14), it was found that fog collection decreased with increasing wind velocity (Fig. 44). However, at fog velocities between 0 and 1 m/s, results are also significantly less than for optimal conditions. In real-life conditions, average fog velocities can vary between 1 and 10 m/s whereas, in this experimental setup, v_0 is estimated to be 0.15-0.2 m/s. Thus, because the effects of wire diameter rely heavily on fog aerodynamics, we attribute the lack of variability to the low wind speed. To confirm this, it would be pertinent to test a wider array of diameters at optimal wind speeds. A wire diameter of 0.18mm was maintained for the remainder of the study due to its theoretical potential, and to minimize the weight of any subsequent scaled-up system.

Moreover, it should be noted that the aerodynamic and deposition efficiencies do not take into account additional factors such as clogging and shedding speed and spacing.

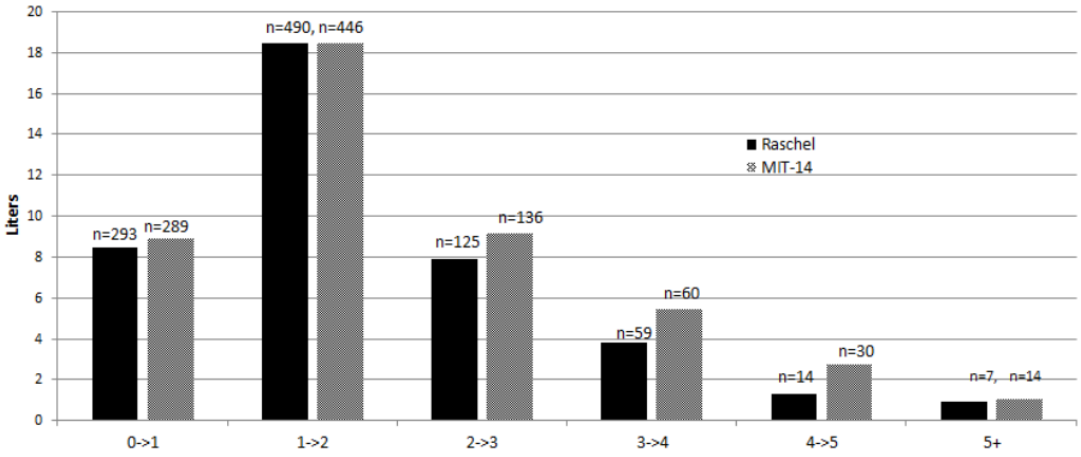

Figure 44. Water collected with fog harvesters with respect to fog velocity [34]

5.1.2.3 Influence of Pitch

Another parameter that was optimised for the harp collector design was the pitch or the distance between each individual wire. From Figure 45, we observe a similar trend between the fog captured and water collection rate.

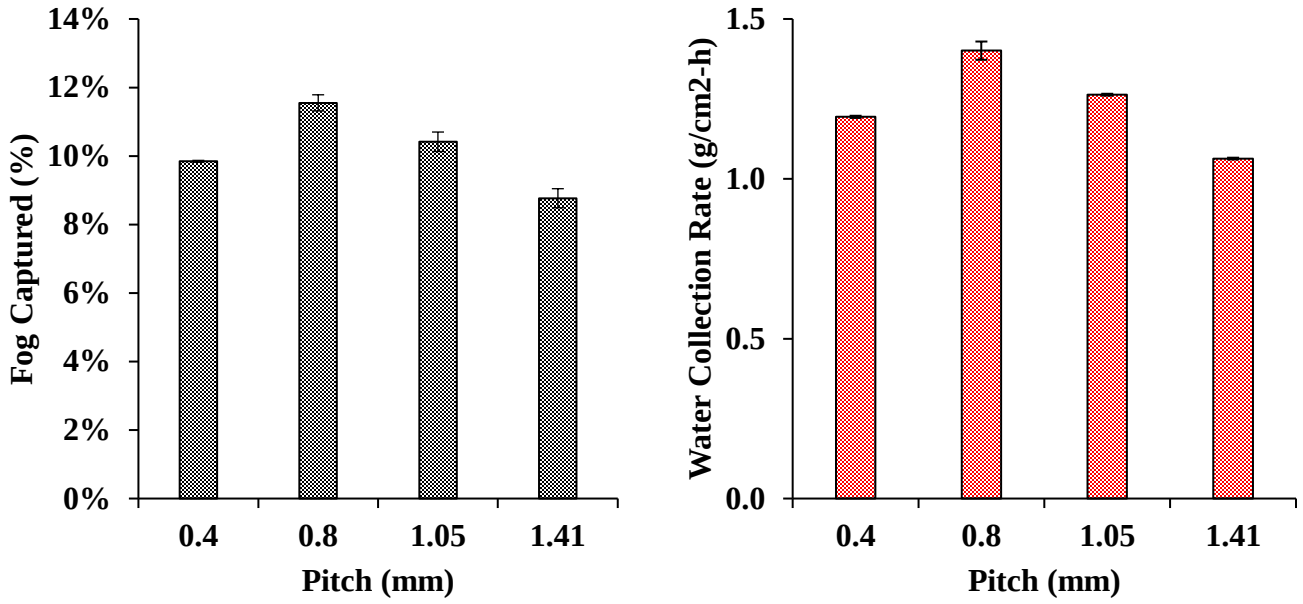

Figure 45. Fog collection and water collection rate as a function of pitch

When the pitch is decreased, an increase in fog harvesting performance was observed. This trend is true until the distance between wires reaches 0.8 mm below which clogging can occur. This phenomena can be seen in Figure 46, where the clogging criteria 2c is equal to the pitch.

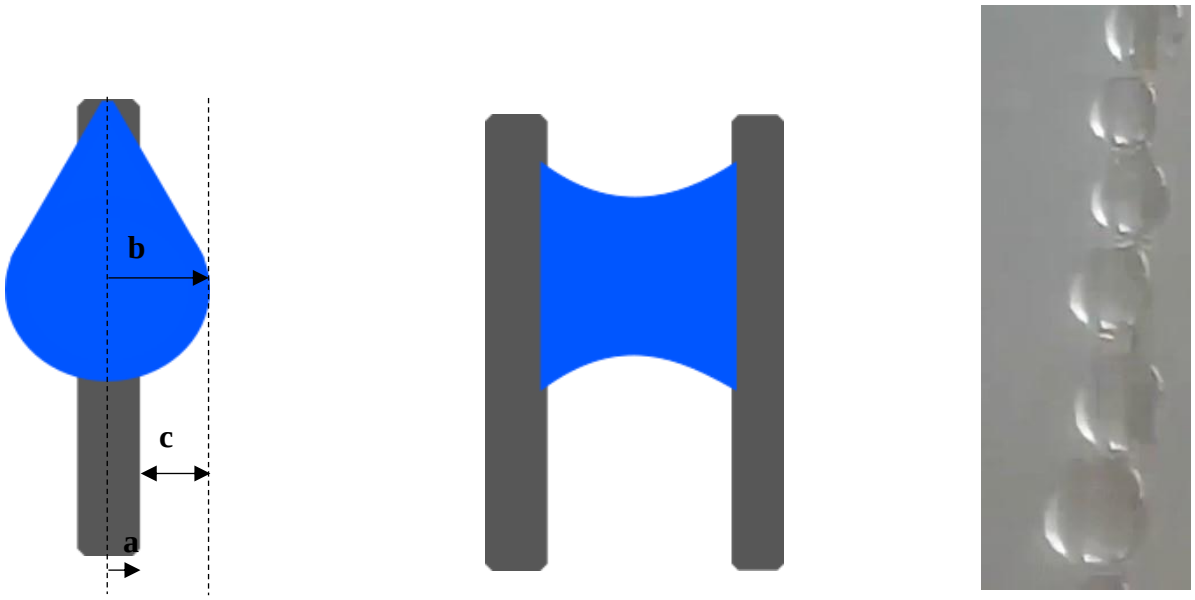

Figure 46. (a) Schematic of droplet geometry on a vertical wire. (b) Clogging between two wires (c) Still frame of maximum droplet diameter

$$2c = pitch$$

The maximum droplet diameter before sliding down the wire was measured through video analysis and was found to be of 1.2±0.2 mm. The maximum radius (b) is then found to be of 0.6±0.1 mm. The wire radius (a) is set to 0.09 mm and thus, the clogging criteria corresponds to 1.02±0.2 mm. This is in accordance with the obtained results as the optimum would be anywhere between 0.82 and 1.22 mm. Above this value, the available water collecting surface decreases due to high spacing between wires. It is also important to note that these theoretical values are valid for single droplets and that it is unlikely that all droplets that form and grow on the harp wires achieve their maximum diameter. Calculating the collection efficiency (Table 11), we can see that as the pitch is decreased, collection efficiency increases. This follows the logic that a higher amount of surface for collection is available the more wires are brought closer together. Even though this is true theoretically, one must take precaution to consider the other highlighted parameters that affect efficiency mentionned previously (clogging, re-entrainment, shedding rate etc.) This is especially noticeable when comparing the collection efficiency of harps and SS-CNT substrates. The latter substrate predicts higher efficiency when in fact, as we have shown, this is far from the reality.

Table 11. Shade coefficient, pressure drop coefficient, aerodynamic and collection efficiencies as a function of pitch

Pitch (mm)	**Shade Coefficient (Riveira et al.)**	**Shade Coefficient (Park et al.)**	**Pressure drop coefficient C_0**	**Aerodynamic efficiency (η_a)**	**Collection efficiency ($\eta_{collection}$)**
1.41	14.5%	21.4%	0.22	10.2%	4.68%
1.05	19.4%	27.1%	0.31	12.8%	5.89%
0.8	25.6%	33.4%	0.45	15.8%	7.28%
0.4	51.9%	52.4%	1.84	23.1%	10.6%
SS-CNT	62.0%	-	3.47	22.8%	20.2%

5.1.2.4 Influence of Wettability

Certain harps were modified to evaluate the effect of wettability on harvesting properties of the harps. Untreated harps possess water contact angles of pure 316 SS, equal to 95±2°. Two different treatments were performed on the other harps. The first employed low pressure plasma (80 Pa) with an output power of 100W to deposit a PTFE-like coating on both the wires and the frame. The precursor used for this treatment was perfluorohexane (C_6F_{14}) and the treatment time was of 10 minutes. Looking at Figure 48, interference patterns can be observed indicating a successful deposition of a nanometric coating. This increased the wires' contact angle to 110±1°. The second surface modification was also achieved through low pressure plasma (10Pa) at 90W, using a HMDSO precursor for 15 seconds. This gave hydrophobic wires whose contact angle was of 115±3°.

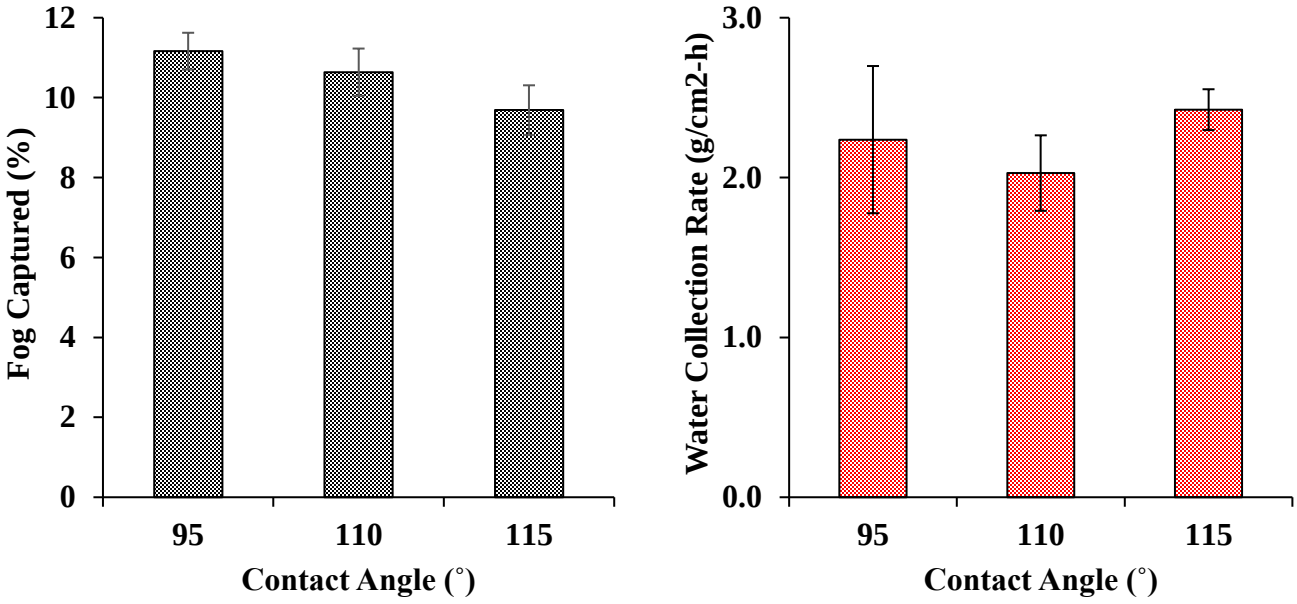

Figure 47. Fog collection and water collection rate as a function surface contact angle

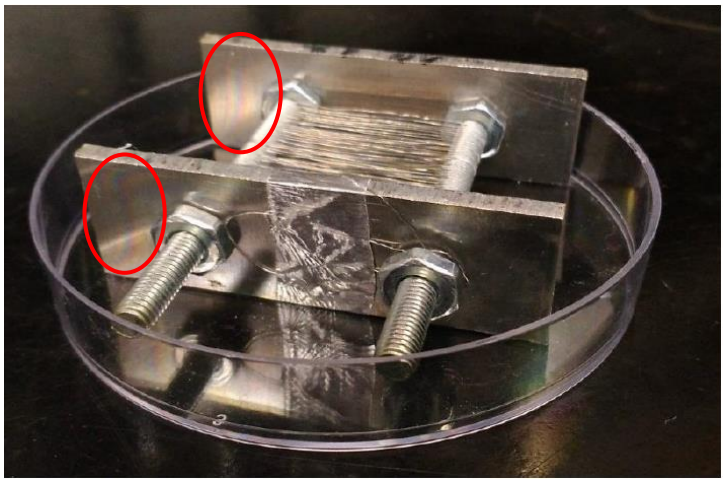

Figure 48. Plasma treated fog harvesting harp

The wettability of fog harvesting surfaces should play a role in the fog harvesting efficiency. Although this was observed for SS-CNT surfaces, fog harvesting harps did not seem to show a significant difference. For a homogeneously wettable surface, it has been demonstrated that hydrophobicity is favorable for fog collection. This was contradicted by Azad et al. who claimed that superhydrophilic surfaces exhibit higher water collection rates than hydrophobic and superhydrophobic surfaces, but otherwise, the literature is in agreement for the opposite claim [30]. In our own studies, this has been shown for SS-CNT. In the case of harps, however, we observe little variability between results for all three surface wettabilities. It should be noted that the hydrophobic treatments performed on the harps lead to similarly hydrophobic surfaces. The lack of variability in wettabilities can potentially explain the results obtained. This leads to several questions on the subtilities of the water contact angle that may be dependent on surface geometries. Drop shape equations like the previously mentioned Young-Laplace equation, should be used in future studies to explain this phenomenon.

5.1.2.5 Influence of Vibration

It was hypothesized that droplet coalescence of water drops could be accelerated by vibrating the harps. This idea came from previous observations where the addition of external force aided droplet coalescence and, when drops approached the critical volume needed to overcome gravity, slide down the wire. This would allow for quicker cycling between collection and shedding. Therefore,

a 3V, 0.1A vibration motors with a frequency between 130-180Hz were added on the harp frame to attempt to improve the amount of water collected. An image of this is shown in Figure 47. Two different vibration modes were defined for testing and are presented in Figure 49. In one case, the vibration motor was left on for the entirety of the experiments. In the other case, vibration was induced for 5 seconds once every minute. This interval was selected based on the time needed for droplets to grow to their maximum diameter (1.2±02 mm), 79±15s, before dropping This was found via video analysis which is discussed further in Chapter 6. When harps were under constant vibration, it was noticed that droplets shed very rapidly down the wire but never grew to sizes previously observed. Therefore, by allowing drops to grow close to their critical volume before shedding, it was possible to explore which option could be most beneficial to fog harvesting efficiency. In Figure 50, we see that both constant and intermittent vibration yielded similar results. A small increase is observed for constant vibration compared to previous results.

While droplets seemed to shed more rapidly, it is assumed that the vibrations induced in the wire contributed to breaking the droplets into lower volume units and that ultimately, the sheer amount of water remained in the same range from test to test. This brought the design variables investigation for single stage harps to a close.

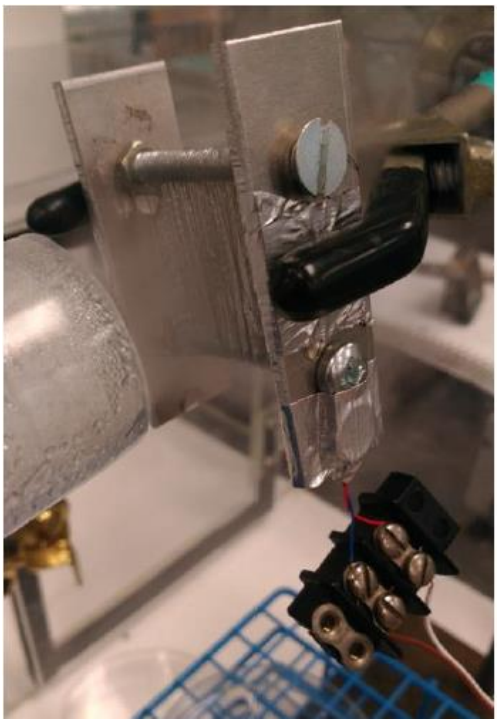

Figure 50. Fog harvesting harp with vibration motor

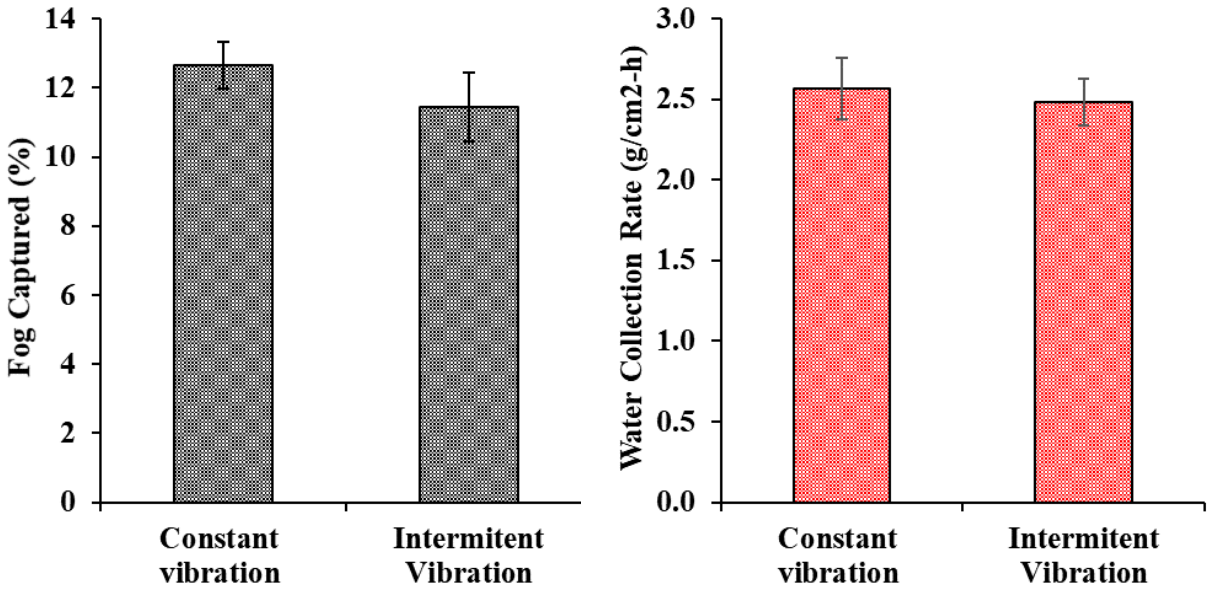

Figure 49. Fog collection and water collection rate as a function of vibration

5.1.2.6 Influence of Additional Stages

The final attempt to improve fog collection efficiency was to put two harps one behind the other. This was inspired by the Eiffel 3D mesh collectors. It is also parallel to multi-stage compressors whose efficiency increases with additional compression and expansion stages. Practically, as fog passes over the harp, only 12%, roughly is captured with a single stage. By adding a second stage, a fraction of the remaining uncaptured fog could be recuperated. Therefore, a new harp frame was built that would allow for up to a total of three stages. This was done to allow for adjustable distance between the first and second stage. The fog harvesting results are presented in Figure 51.

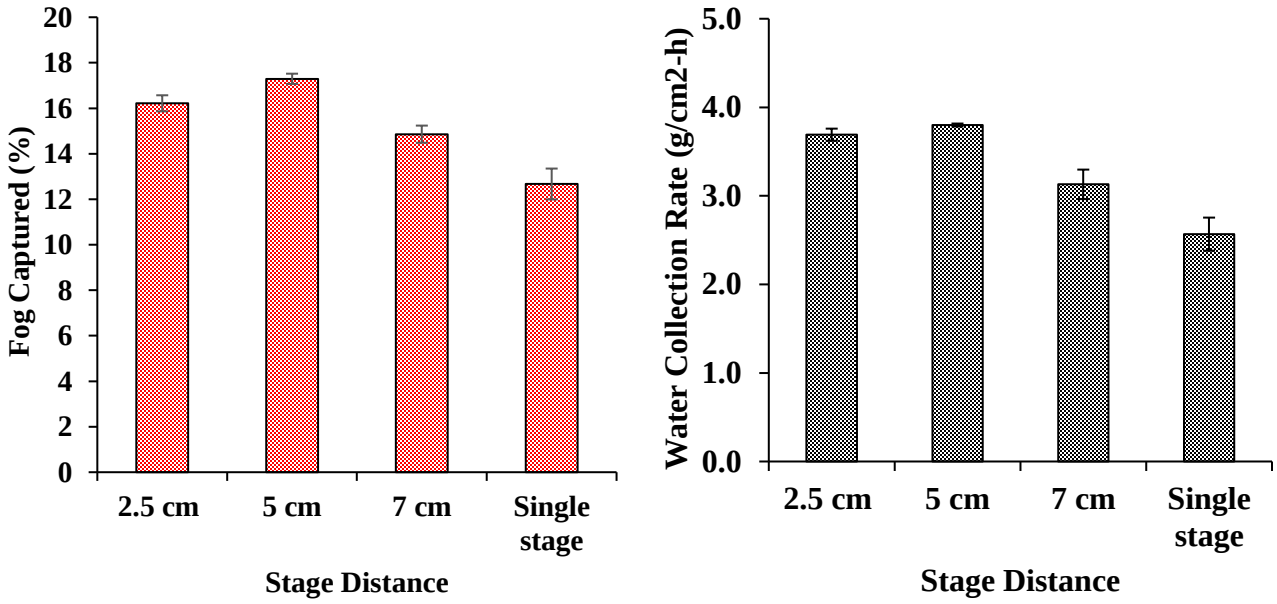

Figure 51. Fog collection and water collection rate as a function of secondary stage distance

Although the results for 2.5 cm and 5.0 cm spacing were found to be similar, when considering the standard deviations, the optimal spacing between the stages was set to 5cm, capturing 17.3±0.2% of fog water. At 7 cm, a noticeable drop in collection is observed. This is likely due to the non-directional seeping of fog away from the harp (upwards or downward) as air no longer pushes the fog and its velocity is at this distance, nearly negligible. Both the amount of fog and the water collection rate were increased when adding a second stage by 4.6%. At the laboratory scale this seems low, however, this could seem promising for larger scales. Also, water collection rate has

increased by 1.2 g/cm^2-h. That being said, the addition of a secondary stage represents an increase in cost and should properly be considered upon scaling.

5.2 Large Scale

5.2.1 Experiment Methodology

For large scale tests, a fog making device was designed using an ultrasonic mister, submerged into an enclosed basin containing liquid water. Two openings were cut onto the top of the basin to add a fan, placed downwards to drive fog out of the container through the second opening. The total amount of fog generated through this system was measured to be of 2670±300 g. The variability of the fog generated is due to the amount of water lost through poor insulation of the container and liquid water “jumping” out of the basin as a result of vibrations caused by the ultrasonic discs.

Finally, a channel was added to direct the fog towards the harp. Figure 52 shows the large scale harp as well at the experimental montage.

Figure 52. Large scale harp (top) and experimental montage (bottom)

5.2.2 Results

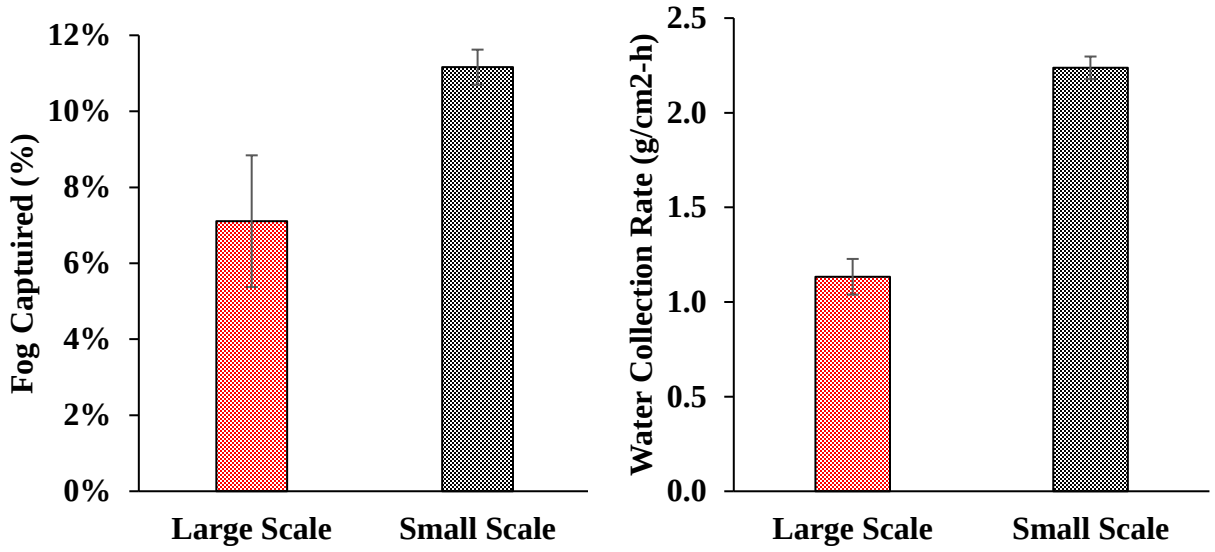

Figure 53. Fog collection and water collection rate of large and small scale harps

From figure 53 we see that, when compared to the small scale harps, the amount of fog captured and water collection rate are decreased. This can be due to many factors. In this larger scale system, the addition of a fan visibly increases the wind speed when compared to the ultrasonic humidifier used for small scale studies. Also, there is a significant amount of uncertainty when measuring the active surface that collects fog. In fact, Figure 54 shows that a fog does not cover the harp completely. Thus, this variability leads to a low-quality assessment of water collection rate. For this reason, the results presented must be taken as purely preliminary. In order to pursue these large-scale tests and compare them to results obtained with the small harps, it would be necessary to obtain a better monitoring and control on basic experimental parameters such as the wind speed and active surface area of the harp. This also implies gaining a better understanding of elements that were overlooked in the small-scale study.

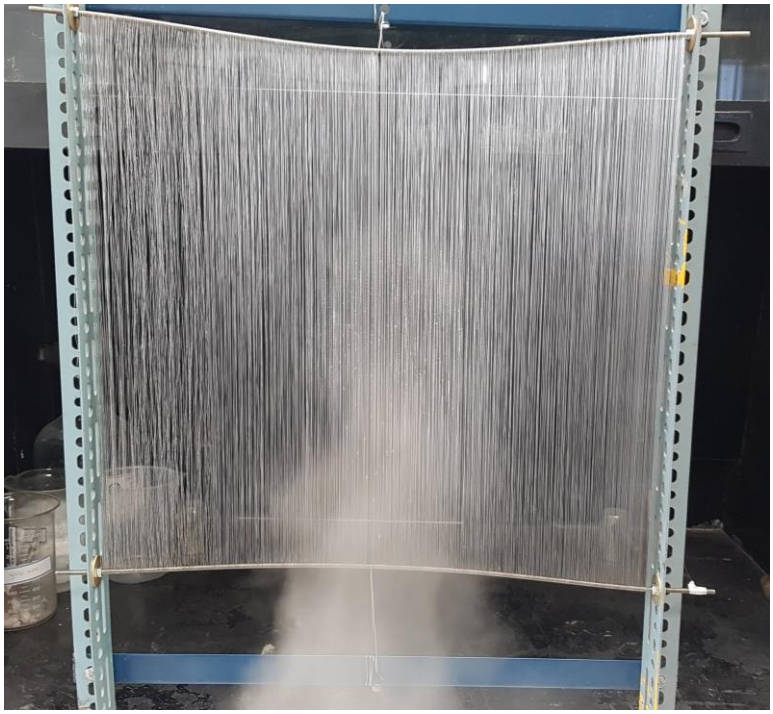

Figure 54. Large scale fog harvesting experiment

Finally, another element that could possibly explain the discrepancies between small and large scale capture is the angle of attack of fog onto the harp. In small scale studies, fog flow was directed perpendicularly to the samples whereas as in the scaled version, this angle is of approximately 40° (Fig. 55). The optimal angle of attack was found to be 90°. Values below this negatively affect the water collection rate. Thus, in this might be a factor that explains the lower performance of the large scale harp.

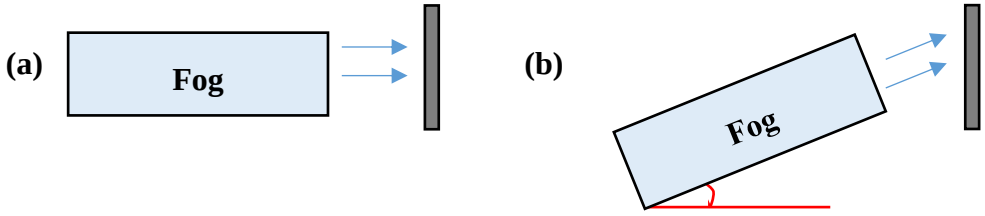

Figure 55. (a) 90° incident fog onto small-scale harp (b) 40° incident fog onto large scale harp.

To conclude this section, a wide range of physico-chemical parameters were assessed for fog harvesting in order to appropriately design and scale an optimal device. This included the geometrical aspect by evaluating mesh-like and harp fog harvesters. Then, surface chemistry was evaluating by comparing fog harvesting performance of hydrophobic and superhydrophilic substrates. Further comparison of the results obtained with the literature are discussed in Chapter 6.

CHAPTER 6 GENERAL DISCUSSION AND COMPLEMENTARY RESULTS

6.1 SEM Images of SS-CNT

Hydrophilic SS-CNT samples were observed in SEM to observe surface topology and obtain a preliminary assessment of the surface elemental composition. Figure 56 show the pristine SS grids before and after CNT growth [226]. It can be seen that the SS wire has increased in diameter from 25.4μm to 39.2μm. This corresponds to CNT heights of approximately 6.9μm, which is in accordance with values published by previous work using the CVD method. Thus, effective micro structuring has been achieved. For untreated SS-CNT samples, surfaces are characterised as hydrophobic, exhibiting contact angles of approximately 120°. That being said, recent studies into CNT forests have shown that the wettability model that resembles that of a rose petal [78]. This is termed parahydrophobicity occurs due to the high contact angle hysteresis of contact angles on CNT forests. This implies a high adhesion force between the liquid and the surface. In fact, while the apparent contact angles can be as high as 150°, the substrate can be completely turned upside down and the droplet will not roll off. Therefore, CNT substrates are in an intermediate state between Wenzel and Cassie-Baxter. In this regime, some of the liquid fills the spaces within the CNT forest while the rest sits atop the air between CNTs. This has implications in fog harvesting in further showing how such surfaces are not desirable as it has been shown that low adhesion surfaces are favorable for drop shedding and surface regeneration.

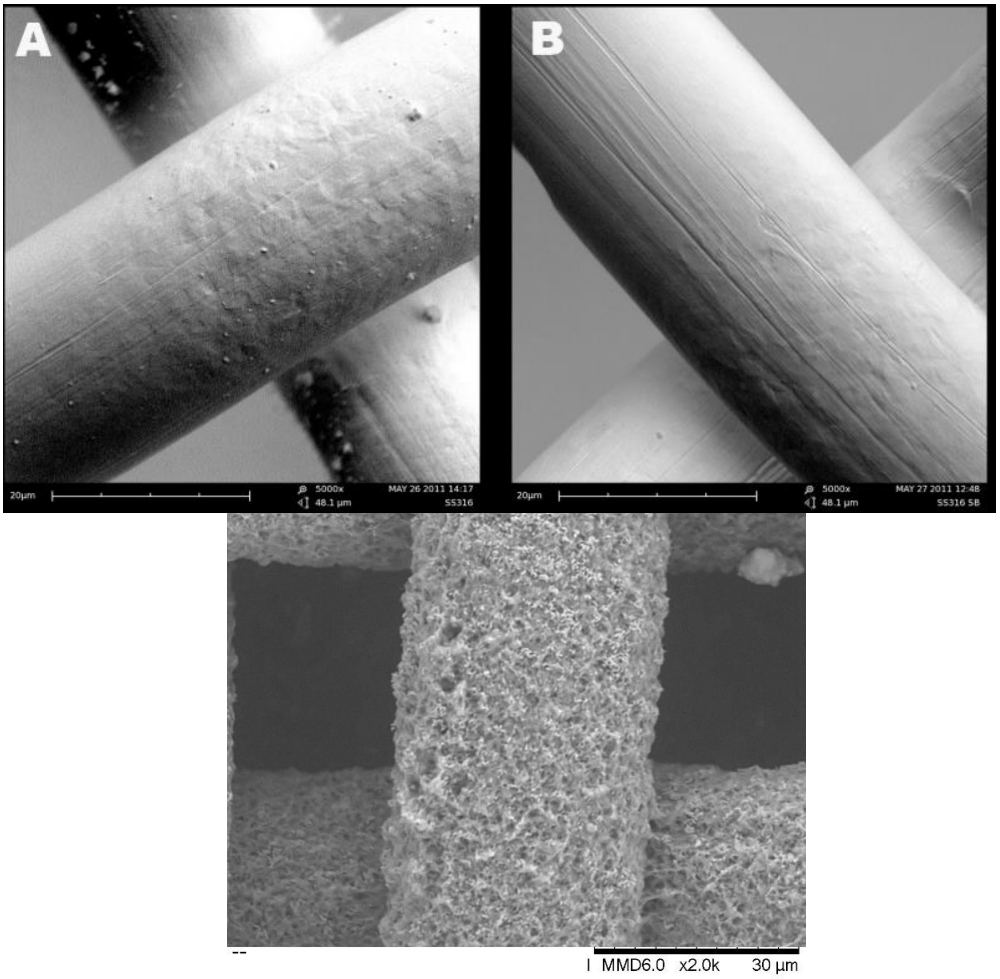

Figure 56. SEM micrographs of pristine (a), HCl etched (b) and (c) CNT covered SS mesh [226]

6.2 Influence of Iron Pentacarbonyl in PICVD Treatments

PICVD provides many advantages in comparison to other coating techniques. However, the lack of controllability on iron pentacarbonyl at the inlet remains an important aspect to study. As mentioned in the article, the effect of iron pentacarbonyl in the PICVD reaction is considerable in depositions. It is clear from the obtained results that iron compounds are found in all coatings, independently of the treatment type. Thus, we can elaborate a list of possible areas where iron pentacarbonyl acts in the experiment. First, it is involved in the photochemical reactions. For thermal decomposition, it has been hypothesized that $Fe(CO)_5$ dissociates into its lower intermediate compounds through the loss of CO groups [140], [196], [212], [227]. For light

decomposition, we refer back to the principles of photochemistry that require absorption and sufficient energy to cause dissociation of FeCO bonds. The bond dissociation energies for iron carbonyl compounds are presented in Table 12:

Table 12. Bond dissociation energies of iron carbonyls [196], [213], [227], [228]

Compounds	**Bond Dissociation Energy**
$\boldsymbol{Fe(CO)_5}$	41.5 ± 2 kcal/mol
$\boldsymbol{Fe(CO)_4}$	27.9 ± 8.8 kcal/mol
$\boldsymbol{Fe(CO)_3}$	29.1 ± 5.8 kcal/mol
$\boldsymbol{Fe(CO)_2}$	36.7 ± 3.5 kcal/mol
$\boldsymbol{FeCO}$	8.1 ± 3.5 kcal/mol

It is thus possible to observe all these intermediates. It has been reported that upon irradiation of 260 nm in the gas phase for 120 femtoseconds, all these species were observed [227]. As a contrast, for the same irradiation for 100 nanoseconds, only Fe was observed. This suggests extremely rapid dissociation rates and shows how short-lived $Fe(CO)_5$ species are under such irradiations. Despite this fact, it is assumed that all intermediate species can react with other PICVD precursors. This adds a layer of complexity when trying to understand the chemistry of PICVD. A second way that iron pentacarbonyl can influence PICVD is through its effect on reaction efficiency. $Fe(CO)_5$ influences the reaction efficiency due to the depositions occur along the reactor tube itself as well as the samples. This reduces the light intensity which can influence the energetics of gas and solid phase reactions. These two examples of how iron pentacarbonyl intervenes within the system, despite their complexity, can be understood in the current stage of PICVD development. However, the significance of its influence raises questions about the practical application of PICVD. At the origin of these questions is controllability. The variability of iron pentacarbonyl concentration introduced in the system affects the reproducibility of experiments. This limit the applicability of this technique in its current form. To respond to this, it is necessary to put in place a system to control this contaminant to perform parametric studies on the limits and magnitude of its implication in photochemical reactions. Ideally, this would become an additional parameter to be included along pressure, distance from inlet, precursor gas ratio etc.

6.3 Droplet Analysis

Information on droplet growth was obtained through video analysis on a single stainless-steel wire (D=0.18mm). Video frames were then extracted to obtain images that could further be analyzed to extract data such as advancing and receding contact angles, geometrical aspects (diameter and volume) as well as gain insight on dripping mechanism. When water microdroplets from incoming fog impinges onto a wire, it can adhere or be re-entrained back into the fog flow. The ratio of droplets that stick to the surface to those that do not has been defined through the deposition efficiency. Water then grows on the surface through absorption of additional aerosol water particles on the already stuck drops along the wire. For hydrophilic surfaces, water forms a thin film and wets the entire wire surface. As new water is absorbed into the film, a barrel formation with regular spacing is typically observed (Figure 57) [229]–[231].

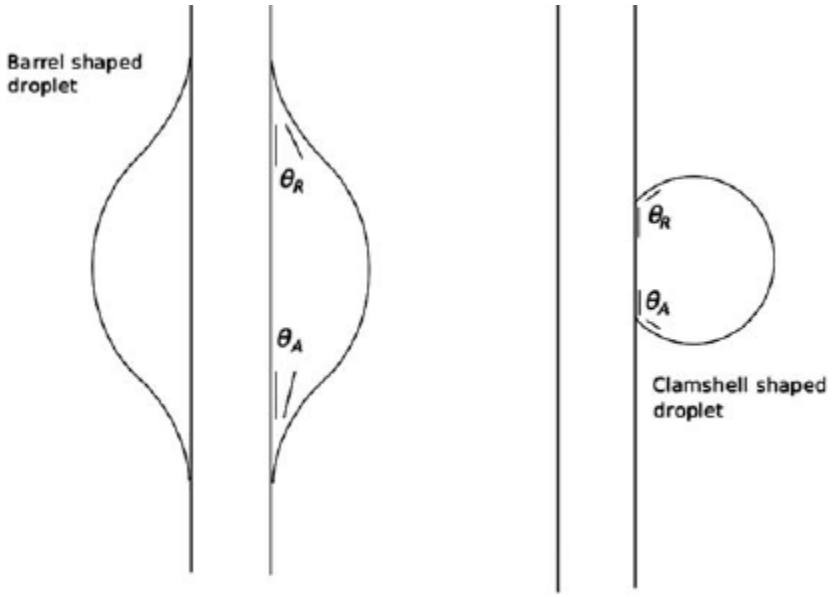

Figure 57. Barrel and clamshell shaped droplets around a cylindrical wire [229]–[231]

It has been suggested that between these barrels, there is always a thin film of liquid [229]. Incoming water is can thus be absorbed by both barrels and the thin film. It has been observed, however, that in this process, the thickness of the liquid film remains constant, suggesting that water is transported towards the closest barrel on the wire. In the case of hydrophobic surfaces, droplets first appear as caps on the wire that will coalesce into a larger shape that is referred to as clamshell [230]. At this stage, there is a distinct three-phase contact line at the pinning points of

the liquid-solid interface. As it further grows, it reaches a stage where the wire is engulfed by the liquid and the contact line disappears. This is known as the barrel state. The droplet will continue to grow through absorption or coalescence with nearby drops until its gravitational force overcomes the adhesive forces retaining it to the wire.

$$\rho_{water} g V sin\alpha > \pi r_{wire} \gamma (cos\theta_r - cos\theta_a) \quad (42) \quad Shi\ et\ al.\ [232]$$

$$\rho_{water} g V sin\alpha > 2 r_{wire} \gamma (cos\theta_r - cos\theta_a) \quad (43) \quad Dussan\ et\ al.; Furmidge\ et\ al.\ [233], [234]$$

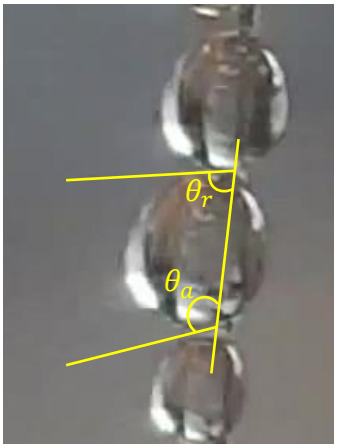

Figure 58. Advancing and receding contact angles of droplet on a vertical wire

It is assumed in these calculations that the droplets assume a perfectly spherical shape. Advancing and receding contact angles were measured through image analysis (Figure 58). These values were found to be $\theta_a = 108° \pm 5°$ and $\theta_r = 83° \pm 4°$. Although the inclination angle α may seem to be non vertical, however, this is explained by the angle at which the video was taken. This angle is 90° because the wire is placed vertically. Although the maximal volume observed before dropping was found to be 1.0±0.2 mm^3, it is impossible to conclude that this is the critical droplet volume for overcoming adhesion. As shown further in this discussion, single droplet detachment is never observed due to the high number density of droplets along a single wire. Thus, it is likely that, while a maximum volume is consistently observed, coalescence with nearby droplets allow for the final push towards the critical volume. We can therefore use the above equations to solve V_c, upon substituting experimental values. The results are presented in table 13:

Table 13. Adhesion force and critical dimensions from various sources

	Adhesion Force	V_c	D_c
Shi et al.	$6.3 \times 10^{-5} N$	$6.42\ mm^3$	$2.31\ mm$
Dussan et al. ; Furmidge et al.	$4.01 \times 10^{-5} N$	$4.09\ mm^3$	$1.98\ mm$

Considering that the maximum droplet diameter observed was of 1.2±0.2 mm, this would mean that it should further increase a minimum of 0.78 mm before dropping. This further shows how the observed maximal droplet volume underestimates the theoretical critical volume. Using hydrophilic SS wires of 0.25 mm in diameter, Shi et al. have found similar trends as the one shown here [33]. They too cannot observe the theoretical maximum. It has also been shown that upon clogging – when a droplet comes into contact with two adjacent wires – the adhesion force effectively doubles. This shows how clogging can negatively influence the collection efficiency, by increasing the barrier towards droplet removal.

From this, we know that, while it is theoretically possible for gravity to induce the detachment of droplets from the wire, it does not happen this way in practice. We therefore must look towards other possible mechanisms that are responsible for the shedding of water. Through video analysis, we can gain better insight into how this occurs. Using a camera that captures 60 frames per second, we look at three separate events. In the first event (Figure 59 (a)), we observe two droplets that are below the maximum observable diameter that are sufficiently close to coalesce together. This initiated detachment. Subsequent frames then show the drop sliding along the wire absorbing all other droplets below it. Interestingly, we also observe a secondary event above the initiating droplet, two other water drops that coalesce together but to not form a sufficiently large product to overcome adhesion. The total time of this event is of 83.4ms. In the following sequence, primary coalescence is seen in the first frame. Here we see a case where a droplet (bottom) achieves the maximum observable volume presented previously. However, it is clear from the following frames that the initiation occurs due to coalescence rather than gravity. A secondary event (Figure 59 (b)) shows three other droplets also combine above the initiation point but in this scenario, the newly formed droplet is large enough to slide down. One distinguishing factor between these two cases is the initial size of the secondary droplets – droplets are much closer to their experimental

maximum in the second scenario. Finally, in the last sequence (Figure 59 (c)), we observe a series of cascading events. In fact, in the first two frames, droplets merge but do not shed. Much like in the first scenario, they form a single droplet that is too small to fall and too far from neighbouring droplets that could also coalesce and increase the volume towards its critical value. It is only in the third frame that larger droplets coalesce and initiate detachment. Similarly, to previous scenarios, a secondary shedding event then occurs. The cascading nature of this particular event, resembling a “domino” like sequence, warranted a further look into the energetics of droplet coalescence.

When two liquid parcels merge, the resulting surface area is lower than the combination of the sum of the individual drops [235]–[237]. This results in an excess of surface energy that has been found to be partially converted into kinetic energy normal to the plane of coalescence [235]. This direction corresponds to a vector perpendicular to the wire. On hydrophobic surfaces, this phenomenon can give rise to droplets literally jumping out of the surface. While jumping is not observed in our experiments, the energetic transfer from surface to kinetic does occur. It is therefore likely that upon coalescence, kinetic energy pushes the droplets outwards and, due to the retention of the newly formed droplet on the wire, it is pulled back towards the surface in an oscillatory manner. This occurs when the dimensions if the new drop are below critical values. This can be at the source of the cascade as this micro-vibration transferred to the wire can onset other droplets to come into contact, coalesce, oscillate and restart the cycle. Figure 60 shows an image of two droplets coalescing and a graph describing the different energy levels as a results of surface energy loss, over time.

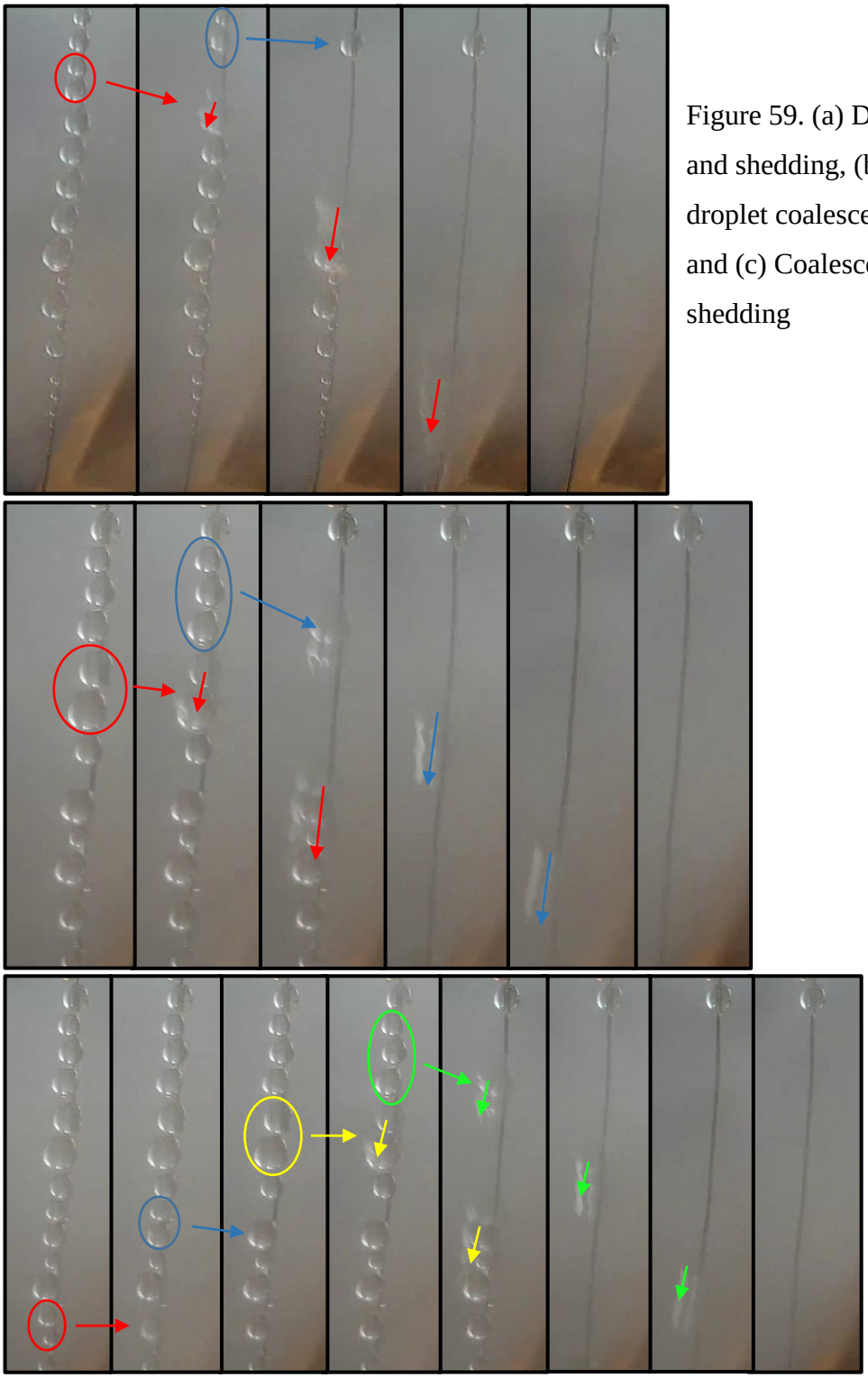

Figure 59. (a) Droplet coalescence and shedding, (b) Successive droplet coalescence and shedding and (c) Coalescence cascade and shedding

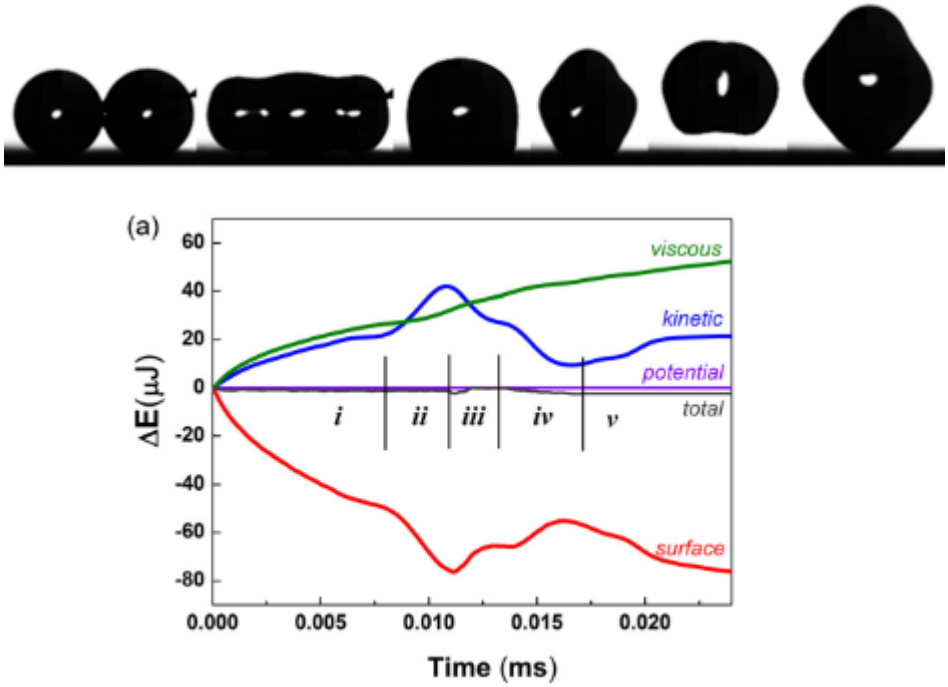

Figure 60. Energy transfer during droplet coalescence [235], [237]

6.4 Limitations of fog harvesting

The optimal harp configurations that were obtained through this study are presented in the Table 14 below:

Table 14. Design parameters for optimal fog harvesting harps

Parameter	Single Stage	Double Stage
Wire Diameter (mm)	0.18	0.18
Pitch (mm)	0.8	0.8
Tilt Angle (°)	10	10
Wettability (°)	95	95
Vibration	No	No
Stage Distance (cm)	-	5

The water collection rates for these samples were compared to literature values for various fog harvesters. Only fog collection rate is presented because fog collection (%) is not always reported. The best results from each study have been presented here. From Figure 61, it can be seen that the single stage designed harps are in the average region along with Shi et al. harp samples. That being said, a distinguishing element between their setup and ours is that in their case, they only began fog harvesting when the environmental chamber reached 100% relative humidity – corresponding to saturation [33]. Consequently, it is likely that condensation can occur along with fog harvesting. As it has been mentioned in Chapter 2, fog microdroplets that are captured on the harvesting surface act as nucleation sites for water vapor condensation. This overestimates the results. Another difference between the harps designed in this project and those from Shi et al.'s work, is the geometrical aspect. Here, we performed a systematic procedure to optimize the spacing, angles, wire diameters, as well as additional novel parameters based on theoretical knowledge from the literature. In Shi et al.'s study, despite elucidating the role of most of these parameters, they were not explored as profoundly. Amongst these parameters, pitch was not investigated in their case and the theoretical optimal wire diameter, 0.18 mm was also not studied. It is therefore expected that we obtain a more efficient fog collection surface.

Upon adding a second stage, it can be seen that the water collection rate becomes a more interesting option when compared to other surfaces. The maximum value obtained in the literature came from a study by Yu et al., who designed patterned wettability substrates [28]. Briefly, these consisted in a hydrophobic background with hydrophilic grid-like pattern atop. While this method yields interesting water collection rates, it recurs to the use of PDMS aerogel particle spray and patterned layer deposition to achieve such a surface. Evaluating the scalability of this method, it can be inferred that it would be more costly and energy-intensive when compared to the solution provided in this report. Also, considering the weak impact of wettability in our findings, it can be stated that our method does not require the use of chemicals for efficient fog collection.

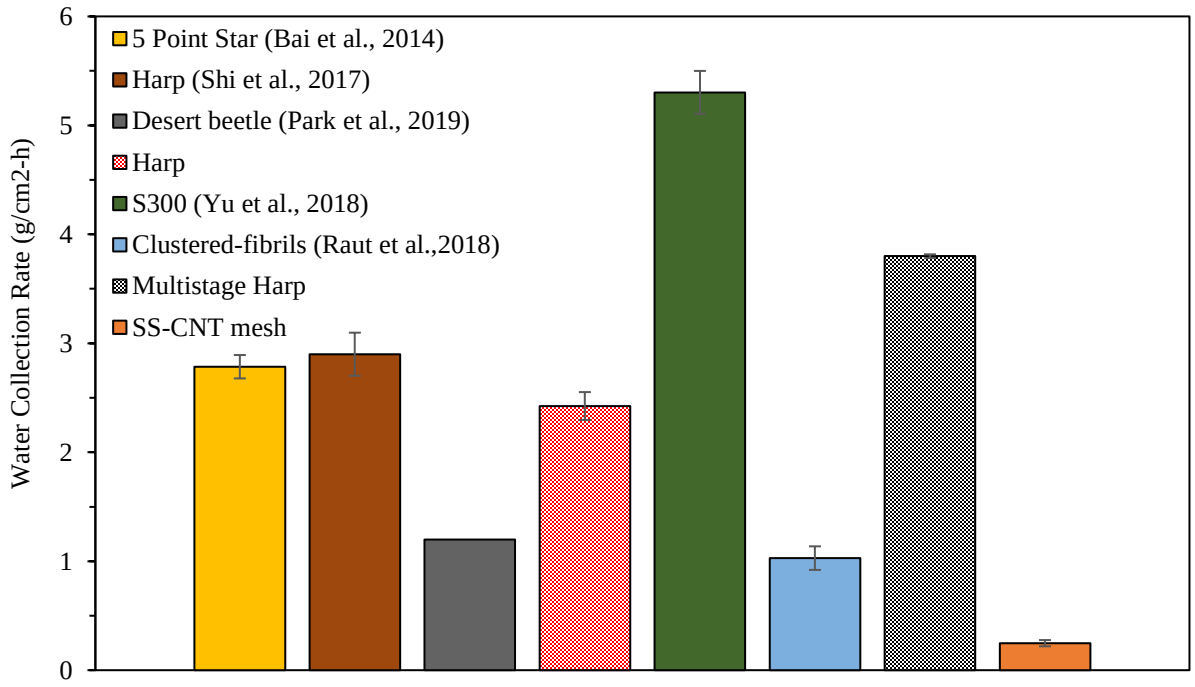

Figure 61. Water collection rate comparison with literature [27], [28], [31], [33], [104]

Though the fog collection performance is acceptable, there are several drawbacks that should be considered in further research. An exploration into surface modification should be done at a deeper level then what has been presented here. This should be investigated in two ways. First, understanding of how macroscopic surface features, curvature in this case, influences contact angle. This would allow for a clearer picture on why the chemical modifications applied did not show a significant difference in fog collection results.

Secondly, once geometrical aspects are mastered, it would be interesting to apply a wettability pattern on the surface, creating small evenly spaced hydrophilic regions along the wire. This could be done chemically by applying a hydrophilic treatment through PICVD for example using a photomask that would only allow for coating in selected regions on the substrate. Inversely, it would be possible to texture selected areas along the wire, increasing the roughness and thus, hydrophobicity, and leaving untextured spots that would maintain its native, less-hydrophobic contact angle. Another possibility to increase collection efficiency would be to mimic spider silk spindle-knots along the wires. this could enhance the movement of water droplets down the wire.

Currently, the montage allows for proof of concept and preliminary evaluation of fog harvesting efficiency. The experimental setup could be improved to achieve higher precision and reproducibility from test to test as well as better simulate real-life conditions. By gaining control on elements such as wind speed, further insight could be gained on the influence of this parameter. The current experimental setup allows for a variation in the amount of fog generated through a dial on the ultrasonic humidifier. A calibration of this manual dial, using a digital anemometer, this could improve control and reproducibility. Furthermore, as the setup is located inside an environmental chamber, it would be beneficial to study the influence of atmospheric conditions like temperature and relative humidity. This would add another element of reality in the laboratory studies and would be possible through monitoring of these parameters.

Another limitation in the fog harvesting project was that no collection mechanism for water was implemented. When water sheds down the wires, it accumulates at the bottom of the device and drips by gravity. As shown in the tilt angle experiments, adding a tilt helps direct water towards a single dripping point. However, this can be impractical upon scaling. Moreover, water is collected in a petri dish beneath the harps, which is not optimal and could lead to problems at higher scales. Much like Standard Fog Collectors have a gutter that gathers and directs water towards a collection recipient, a similar mechanism should be included for the harps.

This leads to another limitation from this project which is the scalability. While the concept and construction are simple for small scale harps, building larger version can quickly become a burden. It would therefore be important to think about how large version can easily be assembled. No investigation was undertaken to evaluate the water quality. This is the most crucial aspect of the project as it will evaluate the potability of water. This would likely be dependent of compounds that are found in fog. Fog samples from Mont Tremblant, for example, were found to be highly acidic with a pH of approximately 4 [238]. Thus, a quality test of harvested water should be done in the future and atmospheric studies should be done for site evaluation, for example, to determine how water should be treated, post-collection. Finally, it would be interesting to test the large-scale harp in real-life conditions. Although difficult to predict, fog is a natural occurrence and data from outdoor tests would be extremely beneficial to the advancement of this project.

CHAPTER 7 CONCLUSION AND RECOMMENDATIONS

To conclude, the study of each design parameter for fog harvesting were investigated. First, a wide array of macroscopic properties were studied to gain a better understanding on their influence in the fog harvesting process. This led to the conclusion that using single wire arrays or “harps” rather that meshed surfaces was preferable due to the reduced amount of clogging on the material. This provided a better air flow around the collection surface and increased the water collection efficiency. A simple device was designed from this observation. This design consisted of using a single stainless-steel wire wound into the evenly spaced grooves of two parallel threaded rods, held together by a frame. The choice of material was also informed by a major drawback of current deployed fog harvesters: durability. Then, physical microscopic elements were investigated through the study of nanotexturing and wettability of SS-CNT meshes. Limits to texturing a surface for enhancement of fog harvesting have been found in our case. Topology does not equate to increased performance in all scenarios. However, hydrophobicity was found to be ideal in fog harvesting. Therefore, texturing a surface to induce a change in wettability towards a hydrophobic regime would be beneficial. Then, chemical microscopic and nanoscopic elements were investigated through surface functionalization. Hydrophobic, low adhesion surfaces were found to provide better properties for fog harvesting in accordance with literature. Fully hydrophilic surfaces are not desirable for fog harvesting. From the results obtained in the harp wettability study, it became interesting to find that geometrical aspects may come into play at lower scales such that surface chemistry becomes irrelevant. Finally, a large-scale device was constructed and preliminarily tested. Along the way, an important PICVD parameters was troubleshoot: iron pentacarbonyl. From this, a method to reduce the aging effect of PICVD films was developed and a paper was written to present its details.

The results of this master’s project have given ample amount of insight into the further development of an efficient fog harvesting device and has provided some answers to the specific objective that were outlined at the start of the project. However, it is important to consider the current limitations. All tests were performed with an ultrasonic humidifier which may not be fully representative of real-life fog. Variations can be found in the size of the water microdroplets, the velocity and the density, bringing a degree of uncertainty to the results presented in this master’s thesis. Secondly, wettability should be further investigated by evaluating a wider range of contact

angles. This would imply a further look into the effect of millimetric surface curvature on wettability.

In future work, it is recommended that these small-scale elements should be further investigated. This can be done by performing a parametric study on the design variable, as well as develop a better understanding of wettability on the harp substrates. Also, it would be pertinent to look into varying the spacing on the mesh-like harvesters to fully assess this aspect as only one mesh size was tested. It is also recommended to perform tests in well controlled conditions. Additionally, an economical assessment should be done to gain insight into the scalability potential of this fog harvester. It is also recommended to include a water collection aspect to the current device using, for example, gutters like SFC's use.

REFERENCES

[1] T. Kahil *et al.*, “A nexus modeling framework for assessing water scarcity solutions,” *Curr. Opin. Environ. Sustain.*, vol. 40, pp. 72–80, 2019.

[2] P. Chowdhary, R. N. Bharagava, S. Mishra, and N. Khan, “Role of Industries in Water Scarcity and Its Adverse Effects on Environment and Human Health,” *Environ. Concerns Sustain. Dev.*, no. Dm, pp. 235–256, 2020.

[3] I. Shiklomanov, “World fresh water resources,” in *Water in crisis a guide to the world’s fresh water resources*, P. H. Gleick, Ed. New York: Oxford University Press, 1993, pp. 13–24.

[4] M. Kummu *et al.*, “The world’s road to water scarcity: Shortage and stress in the 20th century and pathways towards sustainability,” *Sci. Rep.*, vol. 6, no. May, pp. 1–16, 2016.

[5] L. Ohlsson, “Water conflicts and social resource scarcity,” *Phys. Chem. Earth, Part B Hydrol. Ocean. Atmos.*, vol. 25, no. 3, pp. 213–220, 2000.

[6] The World Bank, “Renewable Internal Freshwater Resources per Capita,” 2020. [Online]. Available: https://data.worldbank.org/indicator/ER.H2O.INTR.PC?end=2016&start=1965&view=chart.

[7] N. Fitton *et al.*, “The vulnerabilities of agricultural land and food production to future water scarcity,” *Glob. Environ. Chang.*, vol. 58, no. July 2018, p. 101944, 2019.

[8] H. Ritchie and M. Roser, “Water Use and Stress,” 2020.

[9] Statistics Canada, “Potable water use by sector and average daily use,” *Statistics Canada*, 2020. [Online]. Available: https://www150.statcan.gc.ca/t1/tbl1/en/tv.action?pid=3810027101. [Accessed: 17-Feb-2020].

[10] OECD, “GDP long-term forecast,” *OECD*, 2020. [Online]. Available: https://data.oecd.org/gdp/gdp-long-term-forecast.htm. [Accessed: 17-Feb-2020].

[11] World Health Organization, “Drinking Water,” *World Health Organization*, 2019. [Online].

Available: https://www.who.int/news-room/fact-sheets/detail/drinking-water. [Accessed: 17-Feb-2020].

[12] B. L. Pangarkar, M. G. Sane, and M. Guddad, "Reverse Osmosis and Membrane Distillation for Desalination of Groundwater: A Review," *ISRN Mater. Sci.*, vol. 2011, pp. 1–9, 2011.

[13] K. Zotalis, E. G. Dialynas, N. Mamassis, and A. N. Angelakis, "Desalination technologies: Hellenic experience," *Water (Switzerland)*, vol. 6, no. 5, pp. 1134–1150, 2014.

[14] E. Metzger, B. Owens, P. Reig, W. Hua Wen, and R. Young, "Water-energy nexus: Business risks and rewards," *Water Resour. Inst.*, p. 30, 2015.

[15] E. Jones, M. Qadir, M. T. H. van Vliet, V. Smakhtin, and S. mu Kang, "The state of desalination and brine production: A global outlook," *Sci. Total Environ.*, vol. 657, pp. 1343–1356, 2019.

[16] R. Rautenbach, "Chapter 7 Reverse Osmosis," pp. 410–452, 1989.

[17] V. G. Gude, "Energy consumption and recovery in reverse osmosis," *Desalin. Water Treat.*, vol. 36, no. 1–3, pp. 239–260, 2011.

[18] A. Al-Karaghouli and L. L. Kazmerski, "Energy consumption and water production cost of conventional and renewable-energy-powered desalination processes," *Renew. Sustain. Energy Rev.*, vol. 24, pp. 343–356, 2013.

[19] L. F. Greenlee, D. F. Lawler, B. D. Freeman, B. Marrot, and P. Moulin, "Reverse osmosis desalination: Water sources, technology, and today's challenges," *Water Res.*, vol. 43, no. 9, pp. 2317–2348, 2009.

[20] J. Kim, K. Park, D. R. Yang, and S. Hong, "A comprehensive review of energy consumption of seawater reverse osmosis desalination plants," *Appl. Energy*, vol. 254, no. July, p. 113652, 2019.

[21] J. L. Pérez-Díaz *et al.*, "Fogs: Physical basis, characteristic properties, and impacts on the environment and human health," *Water (Switzerland)*, vol. 9, no. 10, 2017.

[22] J. K. Domen, W. T. Stringfellow, M. K. Camarillo, and S. Gulati, "Fog water as an alternative and sustainable water resource," *Clean Technol. Environ. Policy*, vol. 16, no. 2, pp. 235–249, 2014.

[23] O. Klemm *et al.*, “Fog as a fresh-water resource: Overview and perspectives,” *Ambio*, vol. 41, no. 3, pp. 221–234, 2012.

[24] F. H. Ludlam and B. J. Mason, “The Physics of Clouds,” in *Geophysics II*, J. Bartels, Ed. Springer, Berlin, Heidelberg, 1957, pp. 479–540.

[25] J. J. George, “Fog,” *Compend. Meteorol.*, pp. 1179–1180, 1951.

[26] H. Dong *et al.*, “Bioinspired electrospun knotted microfibers for fog harvesting,” *ChemPhysChem*, vol. 13, no. 5, pp. 1153–1156, 2012.

[27] H. K. Raut, A. S. Ranganath, A. Baji, and K. L. Wood, “Bio-inspired hierarchical topography for texture driven fog harvesting,” *Appl. Surf. Sci.*, vol. 465, pp. 362–368, 2019.

[28] Z. Yu *et al.*, “Desert Beetle-Inspired Superwettable Patterned Surfaces for Water Harvesting,” *Small*, vol. 13, no. 36, pp. 1–6, 2017.

[29] K. F. Kaseke and L. Wang, “Fog and Dew as Potable Water Resources: Maximizing Harvesting Potential and Water Quality Concerns,” *GeoHealth*, vol. 2, no. 10, pp. 327–332, 2018.

[30] M. A. K. Azad, D. Ellerbrok, W. Barthlott, and K. Koch, “Fog collecting biomimetic surfaces: Influence of microstructure and wettability,” *Bioinspiration and Biomimetics*, vol. 10, no. 1, 2015.

[31] Y. Jiang, S. Savarirayan, Y. Yao, and K. C. Park, “Fog collection on a superhydrophilic wire,” *Appl. Phys. Lett.*, vol. 114, no. 8, pp. 1–6, 2019.

[32] S. Yi *et al.*, “Fog Harvesting System: Cactus-Inspired Conical Spines with Oriented Microbarbs for Efficient Fog Harvesting (Adv. Mater. Technol. 12/2019),” *Adv. Mater. Technol.*, vol. 4, no. 12, p. 1970068, 2019.

[33] W. Shi, M. J. Anderson, J. B. Tulkoff, B. S. Kennedy, and J. B. Boreyko, “Fog Harvesting with Harps,” *ACS Appl. Mater. Interfaces*, vol. 10, no. 14, pp. 11979–11986, 2018.

[34] D. M. Fernandez *et al.*, “Fog water collection effectiveness: Mesh intercomparisons,” *Aerosol Air Qual. Res.*, vol. 18, no. 1, pp. 270–283, 2018.

[35] M. Qadir, G. C. Jiménez, R. L. Farnum, L. L. Dodson, and V. Smakhtin, “Fog water collection: Challenges beyond technology,” *Water (Switzerland)*, vol. 10, no. 4, pp. 1–10,

2018.

[36] F. T. Malik, R. M. Clement, D. T. Gethin, W. Krawszik, and A. R. Parker, “Nature’s moisture harvesters: A comparative review,” *Bioinspiration and Biomimetics*, vol. 9, no. 3, 2014.

[37] D. Seo, J. Lee, C. Lee, and Y. Nam, “The effects of surface wettability on the fog and dew moisture harvesting performance on tubular surfaces,” *Sci. Rep.*, vol. 6, no. March, pp. 1–11, 2016.

[38] K. C. Park, S. S. Chhatre, S. Srinivasan, R. E. Cohen, and G. H. McKinley, “Optimal design of permeable fiber network structures for fog harvesting,” *Langmuir*, vol. 29, no. 43, pp. 13269–13277, 2013.

[39] S. Hosseini, F. Ibrahim, I. Djordjevic, and L. H. Koole, “Recent advances in surface functionalization techniques on polymethacrylate materials for optical biosensor applications,” *Analyst*, vol. 139, no. 12, pp. 2933–2943, 2014.

[40] R. Taherian, *Nanocomposites in dielectrics*. Elsevier Inc., 2018.

[41] M. Stepanova and S. Dew, “Nanofabrication: Techniques and principles,” *Nanofabrication Tech. Princ.*, vol. 9783709104, pp. 1–344, 2014.

[42] J. D. Andrade, L. M. Smith, and D. E. Gregonis, “The Contact Angle and Interface Energetics,” *Surf. Interfacial Asp. Biomed. Polym.*, pp. 249–292, 1985.

[43] J. Jeevahan, M. Chandrasekaran, G. Britto Joseph, R. B. Durairaj, and G. Mageshwaran, “Superhydrophobic surfaces: a review on fundamentals, applications, and challenges,” *J. Coatings Technol. Res.*, vol. 15, no. 2, pp. 231–250, 2018.

[44] J. N. Israelachvili, “Special Interactions: Hydrogen-Bonding and Hydrophobic and Hydrophilic Interactions,” *Intermol. Surf. Forces*, vol. 4, pp. 151–167, 2011.

[45] C. Bruel, S. Queffeulou, T. Darlow, N. Virgilio, J. R. Tavares, and G. S. Patience, “Experimental methods in chemical engineering: Contact angles,” *Can. J. Chem. Eng.*, vol. 97, no. 4, pp. 832–842, 2019.

[46] D. Y. Kwok and A. W. Neumann, *Contact angle measurement and contact angle interpretation*, vol. 81, no. 3. 1999.

[47] S. Fundamentals, *Encyclopedia of Tribology*. 2013.

[48] E. Blokhuis, “Liquid Drops at Surfaces,” 2004.

[49] N. K. Adam and H. K. Livingston, “Nature - contact angle and work of adhesion.pdf.” .

[50] S. Ebnesajjad and A. H. Landrock, “Surface Tension and Its Measurement,” *Adhes. Technol. Handb.*, pp. 19–34, 2015.

[51] J. M. Berg, L. G. T. Eriksson, P. M. Claesson, and K. G. N. Børve, “Three-Component Langmuir-Blodgett Films with a Controllable Degree of Polarity,” *Langmuir*, vol. 10, no. 4, pp. 1225–1234, 1994.

[52] S. Wang, K. Liu, X. Yao, and L. Jiang, “Bioinspired surfaces with superwettability: New insight on theory, design, and applications,” *Chem. Rev.*, vol. 115, no. 16, pp. 8230–8293, 2015.

[53] K. Y. Law and H. Zhao, *Surface wetting: Characterization, contact angle, and fundamentals*. 2015.

[54] J. Drelich, E. Chibowski, D. D. Meng, and K. Terpilowski, “Hydrophilic and superhydrophilic surfaces and materials,” *Soft Matter*, vol. 7, no. 21, pp. 9804–9828, 2011.

[55] J. N. Israelachvili, *Adhesion and Wetting Phenomena*. 2011.

[56] D. E. Rosner and M. Epstein, “Fog formation conditions near cool surfaces,” *J. Colloid Interface Sci.*, vol. 28, no. 1, pp. 60–65, 1968.

[57] L. T. Matveev, “Models of Fog Formation,” in *Cloud Dynamics*, L. T. Matveev, Ed. D. Reidel Publishing Company, 1984, pp. 85–110.

[58] G. I. Taylor, “The formation of fog and mist,” *Q. J. R. Meteorol. Soc.*, vol. 43, no. 183, pp. 241–268, 1917.

[59] J. A. Curry and P. J. Webster, *Thermodynamics of atmospheres and oceans*, vol. 82, no. 51. Academic Press, 2001.

[60] D. Lamb and J. Verlinde, “Cloud formation and evolution,” in *Physics and Chemistry of Clouds*, D. Lamb and J. Verlinde, Eds. Cambridge: Cambridge University Press, 2011, pp. 1689–1699.

[61] J. M. Wallace and P. V. Hobbs, “Cloud Microphysics,” *Atmos. Sci.*, pp. 209–269, 2006.

[62] S. Ebnesajjad, “Surface Tension and Its Measurement,” in *Adhesives Technology Handbook*, 2nd ed., S. Ebnesajjad, Ed. William Andrew Inc., 2009, pp. 21–36.

[63] G. Callegari, A. Calvo, and J. P. Hulin, “Contact line motion : Hydrodynamical or molecular,” vol. 4, pp. 29–41, 2006.

[64] K. Katoh, “Contact Angle and Surface Tension Measurement,” in *Surface and Interfacial Tension: Measurement, Theory, and Applications*, S. Hartland, Ed. New York: Marcel Dekker, Inc., 2004, pp. 375–423.

[65] Y. Xiu, L. Zhu, D. W. Hess, and C. P. Wong, “Relationship between work of adhesion and contact angle hysteresis on superhydrophobic surfaces,” *J. Phys. Chem. C*, vol. 112, no. 30, pp. 11403–11407, 2008.

[66] W. A. ZISMAN, “Relation of the Equilibrium Contact Angle to Liquid and Solid Constitution,” pp. 1–51, 1964.

[67] N. K. ADAM, “The Chemical Structure of Solid Surfaces as Deduced from Contact Angles,” pp. 52–56, 1964.

[68] R. J. GOOD, “Theory for the Estimation of Surface and Interfacial Energies,” pp. 74–87, 1964.

[69] O. Carrier and D. Bonn, *Contact Angles and the Surface Free Energy of Solids*, no. 1950. Elsevier Inc., 2015.

[70] K. Seo, M. Kim, and D. H. Kim, “Re-derivation of Young’s Equation, Wenzel Equation, and Cassie-Baxter Equation Based on Energy Minimization,” *Surf. Energy*, 2015.

[71] M. Linke *et al.*, “Leaf surface structures enable the endemic Namib desert grass Stipagrostis sabulicola to irrigate itself with fog water,” *J. R. Soc. Interface*, vol. 9, no. 73, pp. 1965–1974, 2012.

[72] K. Gerasopoulos, W. L. Luedeman, E. Ölçeroglu, M. McCarthy, and J. J. Benkoski, “Effects of Engineered Wettability on the Efficiency of Dew Collection,” *ACS Appl. Mater. Interfaces*, vol. 10, no. 4, pp. 4066–4076, 2018.

[73] B. White, A. Sarkar, and A. M. Kietzig, “Fog-harvesting inspired by the Stenocara beetle -

An analysis of drop collection and removal from biomimetic samples with wetting contrast," *Appl. Surf. Sci.*, vol. 284, pp. 826–836, 2013.

[74] S. Yang *et al.*, "Hydrophilic directional slippery rough surfaces for water harvesting," *Sci. Adv.*, vol. 4, no. 3, p. eaaq0919, 2018.

[75] J. A. Von Fraunhofer, "Adhesion and cohesion," *Int. J. Dent.*, vol. 2012, 2012.

[76] S. Zhang, J. Huang, Z. Chen, and Y. Lai, "Bioinspired Special Wettability Surfaces: From Fundamental Research to Water Harvesting Applications," *Small*, vol. 13, no. 3, pp. 1–28, 2017.

[77] A. Elzaabalawy and S. A. Meguid, "Effect of surface topology on the wettability of superhydrophobic surfaces," *J. Dispers. Sci. Technol.*, vol. 41, no. 3, pp. 470–478, 2020.

[78] Z. Zhou *et al.*, "Parahydrophobicity and stick-slip wetting dynamics of vertically aligned carbon nanotube forests," *Carbon N. Y.*, vol. 152, pp. 474–481, 2019.

[79] D. Möller, "On the history of the scientific exploration of fog, dew, rain and other atmospheric water," *Erde*, vol. 139, no. 1–2, pp. 11–44, 2008.

[80] C. N. Nanev, *Theory of Nucleation*, Second Edi., vol. 1. Elsevier B.V., 2015.

[81] S. Karthika, T. K. Radhakrishnan, and P. Kalaichelvi, "A Review of Classical and Nonclassical Nucleation Theories," *Cryst. Growth Des.*, vol. 16, no. 11, pp. 6663–6681, 2016.

[82] J. W. P. Scmelzer, *Nucleation Theory and Applications*. Wiley-VCH Verlag GmbH & Co. KGaA, 2005.

[83] A. Narayanan, A. Meriin, J. Owen Andrews, J. H. Spille, M. Y. Sherman, and I. I. Cisse, "A first order phase transition mechanism underlies protein aggregation in mammalian cells," *Elife*, vol. 8, pp. 1–26, 2019.

[84] M. Gudala, "Modelling of Methane Hydrate Formation and Dissociation in Presence of Surfactants By Chemical Affinity," no. May 2013, 2016.

[85] B. J. Mason, *Physics of Clouds and Precipitation*, vol. 174, no. 4438. 1954.

[86] H. J. Maris, "Introduction to the physics of nucleation," *Comptes Rendus Phys.*, vol. 7, no.

9–10, pp. 946–958, 2006.

[87] M. Volmer and A. Weber, “Keimbildung in übersättigten Gebilden,” *Zeitschrift für Phys. Chemie*, vol. 119U, no. 1, pp. 277–301, 2017.

[88] X. F. Zhang *et al.*, “Gas-deposition mechanisms of 7YSZ coating based on plasma spray-physical vapor deposition,” *J. Eur. Ceram. Soc.*, vol. 36, no. 3, pp. 697–703, 2016.

[89] H. Jarimi, R. Powell, and S. Riffat, “Review of sustainable methods for atmospheric water harvesting,” *Int. J. Low-Carbon Technol.*, pp. 1–24, 2020.

[90] Y. Tu, R. Wang, Y. Zhang, and J. Wang, “Progress and Expectation of Atmospheric Water Harvesting,” *Joule*, vol. 2, no. 8, pp. 1452–1475, 2018.

[91] A. LaPotin, H. Kim, S. R. Rao, and E. N. Wang, “Adsorption-Based Atmospheric Water Harvesting: Impact of Material and Component Properties on System-Level Performance,” *Acc. Chem. Res.*, vol. 52, no. 6, pp. 1588–1597, 2019.

[92] H. Kim *et al.*, “Adsorption-based atmospheric water harvesting device for arid climates,” *Nat. Commun.*, vol. 9, no. 1, pp. 1–8, 2018.

[93] T. Pan, K. Yang, and Y. Han, “Recent Progress of Atmospheric Water Harvesting Using Metal-Organic Frameworks,” *Chem. Res. Chinese Univ.*, vol. 36, no. 1, pp. 33–40, 2020.

[94] K.-C. Park, D. Fox, M. Hoang, B. McManus, and J. Aizenberg, “Dropwise Condensation on Hydrophobic Cylinders,” pp. 14–16, 2016.

[95] P. Gandhidasan, H. I. Abualhamayel, and F. Patel, “Simplified modeling and analysis of the fog water harvesting system in the asir region of the kingdom of Saudi Arabia,” *Aerosol Air Qual. Res.*, vol. 18, no. 1, pp. 200–213, 2018.

[96] J. de D. Rivera, “Aerodynamic collection efficiency of fog water collectors,” *Atmos. Res.*, vol. 102, no. 3, pp. 335–342, 2011.

[97] C. Duret, “Histoire admirable des plantes et herbes esmerueillables & miraculeuses en nature (The Admirable History of Plants & Herbs),” 1605.

[98] D. Suolo, E. D. Ambiente, D. Suolo, and E. D. Ambiente, “Dipartimento Di Scienze Delle Produzioni Vegetali, Del Suolo E Dell’Ambiente Agroforestale, University of Florence,” vol. 23, pp. 81–86, 2015.

[99] M. Fessehaye, S. A. Abdul-Wahab, M. J. Savage, T. Kohler, T. Gherezghiher, and H. Hurni, "Fog-water collection for community use," *Renew. Sustain. Energy Rev.*, vol. 29, no. January, pp. 52–62, 2014.

[100] R. S. Schemenauer and P. Cereceda, "A Proposed Standard Fog Collector for Use in High-Elevation Regions," *J. Appl. Meteorol.*, vol. 33, no. 11, pp. 1313–1322, 1994.

[101] A. Lummerich and K. J. Tiedemann, "Fog water harvesting on the verge of economic competitiveness," *Erdkunde*, vol. 65, no. 3, pp. 305–306, 2011.

[102] W. J. Hamilton, J. R. Henschel, and M. K. Seely, "Fog collection by Namib Desert beetles," *S. Afr. J. Sci.*, vol. 99, no. 3–4, p. 181, 2003.

[103] A. R. Parker and C. R. Lawrence, "Water capture by a desert beetle," *Nature*, vol. 414, no. November, pp. 33–34, 2001.

[104] H. Bai, L. Wang, J. Ju, R. Sun, Y. Zheng, and L. Jiang, "Efficient water collection on integrative bioinspired surfaces with star-shaped wettability patterns," *Adv. Mater.*, vol. 26, no. 29, pp. 5025–5030, 2014.

[105] S. Deng *et al.*, "Controlled droplet transport to target on a high adhesion surface with multi-gradients," *Sci. Rep.*, vol. 7, no. April, 2017.

[106] A. Ghosh, R. Ganguly, T. M. Schutzius, and C. M. Megaridis, "Wettability patterning for high-rate, pumpless fluid transport on open, non-planar microfluidic platforms," *Lab Chip*, vol. 14, no. 9, pp. 1538–1550, 2014.

[107] Y. Zheng *et al.*, "Directional water collection on wetted spider silk," *Nature*, vol. 463, no. 7281, pp. 640–643, 2010.

[108] D. Gurera and B. Bhushan, "Optimization of bioinspired conical surfaces for water collection from fog," *J. Colloid Interface Sci.*, vol. 551, pp. 26–38, 2019.

[109] S. Knoch, G. Chouinard, M. J. Dumont, and J. R. Tavares, "Dip-dip-dry: Solvent-induced tuning of polylactic acid surface properties," *Colloids Surfaces A Physicochem. Eng. Asp.*, vol. 578, no. June, p. 123591, 2019.

[110] F. Chen, C. N. Lee, and S. H. Teoh, "Nanofibrous modification on ultra-thin poly(e-caprolactone) membrane via electrospinning," *Mater. Sci. Eng. C*, vol. 27, no. 2, pp. 325–

332, 2007.

[111] A. V. Vakhrushev, A. V. Severyukhin, A. Y. Fedotov, M. A. Korepanov, O. Y. Severyukhina, and S. A. Gruzd, “Short communications: Trends on technological concepts,” *Appl. Nanotechnol. Mater. Appl.*, no. 1, pp. 109–113, 2016.

[112] V. Jourdain and C. Bichara, “Current understanding of the growth of carbon nanotubes in catalytic chemical vapour deposition,” *Carbon N. Y.*, vol. 58, pp. 2–39, 2013.

[113] Y. Xu and X.-T. Yan, *Chemical Vapour Deposition*. 2010.

[114] D. Sugumar and L. Kong, “Chemical Vapor Deposition for Film Deposition,” *Encyclopedia of Microfluidics and Nanofluidics*. Springer, pp. 1–8, 2013.

[115] M. Aliofkhazraei and A. S. H. Makhlouf, *Handbook of Nanoelectrochemistry: Electrochemical Synthesis Methods, Properties, and Characterization Techniques*. Springer Reference, 2016.

[116] C. A. Dorval Dion and J. R. Tavares, “Photo-initiated chemical vapor deposition as a scalable particle functionalization technology (a practical review),” *Powder Technol.*, vol. 239, pp. 484–491, 2013.

[117] K. K. Gleason, *CVD Polymers Fabrication of Organic Surfaces and Devices*. 2015.

[118] C. E. Morosanu, *Thin Films by Chemical Vapour Deposition*, vol. 55, no. May 2008. 1990.

[119] P. M. Martin, *Deposition technologies for films and coatings*. 2005.

[120] H. O. Pierson, W. A. Publishing, and N. York, *HANDBOOK OF CHEMICAL VAPOR DEPOS I TION (CVD) by*, no. Cvd. 1999.

[121] S. Shukrullah, N. M. Mohamed, M. S. Shaharun, and M. Y. Naz, “Parametric study on vapor-solid-solid growth mechanism of multiwalled carbon nanotubes,” *Mater. Chem. Phys.*, vol. 176, pp. 32–43, 2016.

[122] G. D. Nessim, “Properties, synthesis, and growth mechanisms of carbon nanotubes with special focus on thermal chemical vapor deposition,” *Nanoscale*, vol. 2, no. 8, pp. 1306–1323, 2010.

[123] K. Jiang, C. Feng, K. Liu, and S. Fan, “A vapor-liquid-solid model for chemical vapor

deposition growth of carbon nanotubes," *J. Nanosci. Nanotechnol.*, vol. 7, no. 4–5, pp. 1494–1504, 2007.

[124] M. Hashempour, A. Vicenzo, F. Zhao, and M. Bestetti, "Direct growth of MWCNTs on 316 stainless steel by chemical vapor deposition: Effect of surface nano-features on CNT growth and structure," *Carbon N. Y.*, vol. 63, no. July, pp. 330–347, 2013.

[125] D. Farhanian, G. De Crescenzo, and J. R. Tavares, "Kinetics, Chemistry, and Morphology of Syngas Photoinitiated Chemical Vapor Deposition," *Langmuir*, vol. 33, no. 8, pp. 1780–1791, 2017.

[126] J. C. BEVINGTON, "Chemical Reviews," *Nature*, vol. 227, no. 5256, pp. 419–419, 1970.

[127] W. A. Noyes and L. S. Kassel, "A review of photochemistry," *Chem. Rev.*, vol. 3, no. 2, pp. 199–225, 1926.

[128] A. B. Beeler, "Introduction: Photochemistry in Organic Synthesis," *Chem. Rev.*, vol. 116, no. 17, pp. 9629–9630, 2016.

[129] J. C. Zwinkels and C. Canada, "Encyclopedia of Color Science and Technology," *Encycl. Color Sci. Technol.*, no. August, 2020.

[130] D. H. Sliney, "What is light? the visible spectrum and beyond," *Eye*, vol. 30, no. 2, pp. 222–229, 2016.

[131] S. Chatani, C. J. Kloxin, and C. N. Bowman, "The power of light in polymer science: Photochemical processes to manipulate polymer formation, structure, and properties," *Polym. Chem.*, vol. 5, no. 7, pp. 2187–2201, 2014.

[132] E. Kasparek, J. R. Tavares, M. R. Wertheimer, and P. L. Girard-Lauriault, "VUV Photodeposition of Thiol-Terminated Films: A Wavelength-Dependent Study," *Langmuir*, vol. 34, no. 41, pp. 12234–12243, 2018.

[133] N. Hordy, D. Rabilloud, J. L. Meunier, and S. Coulombe, "High temperature and long-term stability of carbon nanotube nanofluids for direct absorption solar thermal collectors," *Sol. Energy*, vol. 105, pp. 82–90, 2014.

[134] P. B. Roussel and R. A. Back, "Photochemistry of CO-H2 Mixtures Irradiated at 193.3 m," *J. Photochem. Photobiol. A*, vol. 52, pp. 235–239, 1990.

[135] Y. L. Yung and W. B. DeMore, *Photochemistry of Planetary Atmospheres*. New York: Oxford University Press, 1999.

[136] B. D. Darwent, "National Standard Reference Data Series, National Bureau of Standards, vol. 42," *J. Chem. Educ., Washingt. DC*, p. 502, 1965.

[137] P. Erman *et al.*, "Direct determination of the ionization potential of CO by resonantly enhanced multiphoton ionization mass spectroscopy," *Chem. Phys. Lett.*, vol. 215, no. 1–3, pp. 173–178, 1993.

[138] P. C. Painter and M. M. Coleman, *Fundamentals of Polymer Science An Introductory Text*, 2nd ed. CRC Press, 1997.

[139] Y. Yagci, S. Jockusch, and N. J. Turro, "Photoinitiated polymerization: Advances, challenges, and opportunities," *Macromolecules*, vol. 43, no. 15, pp. 6245–6260, 2010.

[140] S. Hosseininasab, N. Faucheux, G. Soucy, and J. R. Tavares, "Reaction kinetics and temperature effects in syngas photo-initiated chemical vapor deposition on single-walled carbon nanotubes," *J. Nanoparticle Res.*, vol. 21, no. 6, 2019.

[141] S. Guimond and M. R. Wertheimer, "Surface degradation and hydrophobic recovery of polyolefins treated by air corona and nitrogen atmospheric pressure glow discharge," *J. Appl. Polym. Sci.*, vol. 94, no. 3, pp. 1291–1303, 2004.

[142] T. Senzai and S. Fujikawa, "Fast hydrophobicity recovery of the surface-hydrophilic poly(dimethylsiloxane) films caused by rechemisorption of dimethylsiloxane derivatives," *Langmuir*, vol. 35, no. 30, pp. 9747–9752, 2019.

[143] E. P. Everaert, H. C. Van Der Mei, and H. J. Busscher, "Hydrophobic recovery of repeatedly plasma-treated silicone rubber. Part 2. A comparison of the hydrophobic recovery in air, water, or liquid nitrogen," *J. Adhes. Sci. Technol.*, vol. 10, no. 4, pp. 351–359, 1996.

[144] E. P. Everaert, H. C. van der Mei, J. De Vries, and H. J. Busscher, "Hydrophobic recovery of repeatedly plasma-treated silicone rubber. Part 1. Storage in air," *J. Adhes. Sci. Technol.*, vol. 9, no. 9, pp. 1263–1278, 1995.

[145] M. J. Owen and P. J. Smith, "Plasma treatment of polydimethylsiloxane," *J. Adhes. Sci. Technol.*, vol. 8, no. 10, pp. 1063–1075, 1994.

[146] B. P. Husted, G. Homstedt, and T. Hertzberg, “The physics behind water mist systems,” *IWMA Conf.*, no. October, pp. 6–8, 2004.

[147] A. J. Yule and Y. Al-Suleimani, “On droplet formation from capillary waves on a vibrating surface,” *Proc. R. Soc. A Math. Phys. Eng. Sci.*, vol. 456, no. 1997, pp. 1069–1085, 2000.

[148] S. Kooij, A. Astefanei, G. L. Corthals, and D. Bonn, “Size distributions of droplets produced by ultrasonic nebulizers,” *Sci. Rep.*, vol. 9, no. 1, pp. 1–8, 2019.

[149] A. Ritter, C. M. Regalado, and J. C. Guerra, “Quantification of fog water collection in three locations of tenerife (Canary Islands),” *Water (Switzerland)*, vol. 7, no. 7, pp. 3306–3319, 2015.

[150] H. Bai *et al.*, “A hierarchical hydrophilic/hydrophobic cooperative fog collector possessing self-pumped droplet delivering ability,” *J. Mater. Chem. A*, vol. 6, no. 42, pp. 20966–20972, 2018.

[151] L. Csurgai-Horváth and J. Bitó, “Fog attenuation on V band terrestrial radio and a low-cost measurement setup,” *2010 Futur. Netw. Mob. Summit*, no. May 2014, 2010.

[152] Cambridge University Engineering Department, *Materials Data Book*. Cambridge University Press, 2003.

[153] M. Koc and R. Bulut, “Assessment of a sessile drop device and a new testing approach measuring contact angles on aggregates and asphalt binders,” *J. Mater. Civ. Eng.*, vol. 26, no. 3, pp. 391–398, 2014.

[154] J. J. Shea, *Microstructural characterization of materials [Book Reveiw]*, vol. 16, no. 2. 2005.

[155] S. Oswald, *X-Ray Photoelectron Spectroscopy in Analysis of Surfaces*. 2013.

[156] Z. Qiu, *Transition Metal-Based Electrocatalysts for Alkaline Water Splitting and CO 2 Reduction*, no. May. 2019.

[157] D. Briggs, “X-ray photoelectron spectroscopy (XPS),” *Handb. Adhes. Second Ed.*, pp. 621–622, 2005.

[158] B. J. Inkson, *Scanning Electron Microscopy (SEM) and Transmission Electron Microscopy (TEM) for Materials Characterization*. Elsevier Ltd, 2016.

[159] E. Ueda and P. A. Levkin, “Emerging applications of superhydrophilic-superhydrophobic micropatterns,” *Adv. Mater.*, vol. 25, no. 9, pp. 1234–1247, 2013.

[160] Y. Si, Z. Dong, and L. Jiang, “Bioinspired Designs of Superhydrophobic and Superhydrophilic Materials,” *ACS Cent. Sci.*, vol. 4, no. 9, pp. 1102–1112, 2018.

[161] T. A. Otitoju, A. L. Ahmad, and B. S. Ooi, “Superhydrophilic (superwetting) surfaces: A review on fabrication and application,” *J. Ind. Eng. Chem.*, vol. 47, no. March, pp. 19–40, 2017.

[162] M. Salta *et al.*, “Designing biomimetic antifouling surfaces,” *Philos. Trans. R. Soc. A Math. Phys. Eng. Sci.*, vol. 368, no. 1929, pp. 4729–4754, 2010.

[163] A. G. Nurioglu, A. C. C. Esteves, and G. De With, “Non-toxic, non-biocide-release antifouling coatings based on molecular structure design for marine applications,” *J. Mater. Chem. B*, vol. 3, no. 32, pp. 6547–6570, 2015.

[164] K. V. Thomas and S. Brooks, “The environmental fate and effects of antifouling paint biocides,” *Biofouling*, vol. 26, no. 1, pp. 73–88, 2010.

[165] E. Occurrence, C. Of, and A. Biocides, “Biocides in antifouling paints : environmental concentration levels and distribution,” no. January, pp. 52–56, 2014.

[166] B. Majhy, R. Iqbal, and A. K. Sen, “Facile fabrication and mechanistic understanding of a transparent reversible superhydrophobic – superhydrophilic surface,” *Sci. Rep.*, vol. 8, no. 1, pp. 1–11, 2018.

[167] L. Zhang, N. Zhao, and J. Xu, “Fabrication and application of superhydrophilic surfaces: A review,” *J. Adhes. Sci. Technol.*, vol. 28, no. 8–9, pp. 769–790, 2014.

[168] S. Granick, “Polymer surface dynamics,” *MRS Bull.*, vol. 21, no. 1, pp. 33–36, 1996.

[169] M. Morra, E. Occhiello, and F. Garbassi, “Contact Angle Hysteresis in Oxygen Plasma Treated Poly(tetrafluoroethylene),” *Langmuir*, vol. 5, no. 3, pp. 872–876, 1989.

[170] M. T. Van Os, “Surface modification by plasma polymerization: film deposition, tailoring of surface properties and biocompatibility,” *Film*, pp. 1–146, 2000.

[171] V. Labonté, A. Marion, N. Virgilio, and J. R. Tavares, “Gas-phase surface engineering of polystyrene beads used to challenge automated particle inspection systems,” *Ind. Eng.*

Chem. Res., vol. 55, no. 27, pp. 7362–7372, 2016.

[172] C. Borcia, I. L. Punga, and G. Borcia, "Surface properties and hydrophobic recovery of polymers treated by atmospheric-pressure plasma," *Appl. Surf. Sci.*, vol. 317, pp. 103–110, 2014.

[173] E. Bormashenko, G. Chaniel, and R. Grynyov, "Towards understanding hydrophobic recovery of plasma treated polymers: Storing in high polarity liquids suppresses hydrophobic recovery," *Appl. Surf. Sci.*, vol. 273, pp. 549–553, 2013.

[174] M. Vandenbossche and D. Hegemann, "Recent approaches to reduce aging phenomena in oxygen- and nitrogen-containing plasma polymer films: An overview," *Curr. Opin. Solid State Mater. Sci.*, vol. 22, no. 1, pp. 26–38, 2018.

[175] D. Hegemann *et al.*, "Deposition of Functional Plasma Polymers Influenced by Reactor Geometry in Capacitively Coupled Discharges," *Plasma Process. Polym.*, vol. 13, no. 2, pp. 279–286, 2016.

[176] D. Hegemann *et al.*, "Suppression of Hydrophobic Recovery by Plasma Polymer Films with Vertical Chemical Gradients," *Langmuir*, vol. 32, no. 3, pp. 651–654, 2016.

[177] F. J. Holly and M. F. Refojo, "Wettability of hydrogels I. Poly(2-hydroxyethyl methacrylate)," *J. Biomed. Mater. Res.*, vol. 9, no. 3, pp. 315–326, 1975.

[178] L. Deng, Y. Li, F. Feng, and H. Zhang, "Study on wettability, mechanical property and biocompatibility of electrospun gelatin/zein nanofibers cross-linked by glucose," *Food Hydrocoll.*, vol. 87, no. June 2018, pp. 1–10, 2019.

[179] J. M. Spruell *et al.*, "Reactive, multifunctional polymer films through thermal cross-linking of orthogonal click groups," *J. Am. Chem. Soc.*, vol. 133, no. 41, pp. 16698–16706, 2011.

[180] E. Bormashenko, G. Chaniel, and R. Grynyov, "Towards understanding hydrophobic recovery of plasma treated polymers: Storing in high polarity liquids suppresses hydrophobic recovery," *Appl. Surf. Sci.*, vol. 273, pp. 549–553, 2013.

[181] A. Marquez, C. Daniel, and J. F. Sanz, "The vacuum-ultraviolet spectrum of Fe(CO)5: An experimental analysis supported by a CASSCF CCI study of the Rydberg states," *J. Phys. Chem.*, vol. 96, no. 1, pp. 121–123, 1992.

[182] Y. Zhang, I. Kobayashi, M. A. Neves, K. Uemura, and M. Nakajima, “Effects of surface treatment and storage conditions of silicon microchannel emulsification plates on their surface hydrophilicity and preparation of soybean oil-in-water emulsion droplets,” *J. Food Eng.*, vol. 167, pp. 106–113, 2015.

[183] L. Lavielle and J. Schultz, “Surface properties of graft polyethylene in contact with water. I. Orientation phenomena,” *J. Colloid Interface Sci.*, vol. 106, no. 2, pp. 438–445, 1985.

[184] C. Vergelati, A. Perwuelz, L. Vovelle, M. A. Romero, and Y. Holl, “Poly(ethylene terephthalate) surface dynamics in air and water studied by tensiometry and molecular modelling,” *Polymer (Guildf).*, vol. 35, no. 2, pp. 262–270, 1994.

[185] P. Rupper, M. Vandenbossche, L. Bernard, D. Hegemann, and M. Heuberger, “Composition and Stability of Plasma Polymer Films Exhibiting Vertical Chemical Gradients,” *Langmuir*, vol. 33, no. 9, pp. 2340–2352, 2017.

[186] L. Li *et al.*, “Combined continuous wave and pulsed plasma modes: For more stable interfaces with higher functionality on metal and semiconductor surfaces,” *Plasma Process. Polym.*, vol. 6, no. 10, pp. 615–619, 2009.

[187] E. Yousif and R. Haddad, “Photodegradation and photostabilization of polymers, especially polystyrene: Review,” *Springerplus*, vol. 2, no. 1, pp. 1–32, 2013.

[188] M. S. Hedenqvist, *Barrier Packaging Materials*, Second Edi. Elsevier Inc., 2012.

[189] O. Galant, M. Davidovich-Pinhas, and C. E. Diesendruck, “The Effect of Intramolecular Cross-Linking on Polymer Interactions in Solution,” *Macromol. Rapid Commun.*, vol. 39, no. 16, pp. 1–5, 2018.

[190] C. A. Dorval Dion, W. Raphael, E. Tong, and J. R. Tavares, “Photo-initiated chemical vapor deposition of thin films using syngas for the functionalization of surfaces at room temperature and near-atmospheric pressure,” *Surf. Coatings Technol.*, vol. 244, pp. 98–108, 2014.

[191] K. Chan and K. K. Gleason, “Photoinitiated chemical vapor deposition of polymeric thin films using a volatile photoinitiator,” *Langmuir*, vol. 21, no. 25, pp. 11773–11779, 2005.

[192] B. J. McMahon, C. A. Pfluger, B. Sun, K. S. Ziemer, D. D. Burkey, and R. L. Carrier,

"Photoinitiated chemical vapor deposition of cytocompatible poly(2-hydroxyethyl methacrylate) films," *J. Biomed. Mater. Res. - Part A*, vol. 102, no. 7, pp. 2375–2382, 2014.

[193] S. H. Baxamusa, "Photoinitiated Chemical Vapor Depostion: Mechanism and Applications," p. 128, 2009.

[194] J. Zhao, M. Wang, and K. K. Gleason, "Stabilizing the Wettability of Initiated Chemical Vapor Deposited (iCVD) Polydivinylbenzene Thin Films by Thermal Annealing," *Adv. Mater. Interfaces*, vol. 4, no. 18, pp. 1–9, 2017.

[195] H. N. Lari, J. Chaouki, and J. R. Tavares, "Continuous aerosol photopolymerization to coat de-agglomerated nanoparticles," *Chem. Eng. J.*, vol. 390, no. December 2019, p. 124526, 2020.

[196] H. Nasri Lari *et al.*, "Shedding light on iron pentacarbonyl photochemistry through a CVD case study," *Catal. Commun.*, vol. 100, no. April, pp. 19–23, 2017.

[197] S. Hosseininasab, N. Faucheux, G. Soucy, and J. R. Tavares, "Full range of wettability through surface modification of single-wall carbon nanotubes by photo-initiated chemical vapour deposition," *Chem. Eng. J.*, vol. 325, pp. 101–113, 2017.

[198] A. Berard, G. S. Patience, G. Chouinard, and J. R. Tavares, "Photo Initiated Chemical Vapour Deposition to Increase Polymer Hydrophobicity," *Sci. Rep.*, vol. 6, no. July, pp. 1–9, 2016.

[199] C. D. Petruczok, E. Armagan, G. O. Ince, and K. K. Gleason, "Initiated chemical vapor deposition and light-responsive cross-linking of poly(vinyl cinnamate) thin films," *Macromol. Rapid Commun.*, vol. 35, no. 15, pp. 1345–1350, 2014.

[200] A. P. Grosvenor, B. A. Kobe, M. C. Biesinger, and N. S. McIntyre, "Investigation of multiplet splitting of Fe 2p XPS spectra and bonding in iron compounds," *Surf. Interface Anal.*, vol. 36, no. 12, pp. 1564–1574, 2004.

[201] H. Yasuda, A. K. Sharma, and T. Yasuda, "Effect of Orientation and Mobility of Polymer Molecules At Surfaces on Contact Angle and Its Hysteresis.," *J. Polym. Sci. Part A-2, Polym. Phys.*, vol. 19, no. 9, pp. 1285–1291, 1981.

[202] K. C. Tseng, N. J. Turro, and C. J. Durning, "Molecular mobility in polymer thin films,"

Phys. Rev. E - Stat. Physics, Plasmas, Fluids, Relat. Interdiscip. Top., vol. 61, no. 2, pp. 1800–1811, 2000.

[203] T. Kerle, Z. Lin, H. C. Kim, and T. P. Russell, "Mobility of polymers at the air/polymer interface," *Macromolecules*, vol. 34, no. 10, pp. 3484–3492, 2001.

[204] W. Hu, Z. Wang, Y. Xiao, S. Zhang, and J. Wang, "Advances in crosslinking strategies of biomedical hydrogels," *Biomater. Sci.*, vol. 7, no. 3, pp. 843–855, 2019.

[205] E. Andrzejewska, "Photopolymerization kinetics of multifunctional monomers," *Prog. Polym. Sci.*, vol. 26, no. 4, pp. 605–665, 2001.

[206] K. Hunger, N. Schmeling, H. B. T. Jeazet, C. Janiak, C. Staudt, and K. Kleinermanns, "Investigation of cross-linked and additive containing polymer materials for membranes with improved performance in pervaporation and gas separation," *Membranes (Basel).*, vol. 2, no. 4, pp. 727–763, 2012.

[207] J. S. Kang, J. Won, H. C. Park, U. Y. Kim, Y. S. Kang, and Y. M. Lee, "Morphology control of asymmetric membranes by UV irradiation on polyimide dope solution," *J. Memb. Sci.*, vol. 169, pp. 229–235, 2000.

[208] A. Boersma, D. Cangialosi, and S. J. Picken, "Mobility and solubility of antioxidants and oxygen in glassy polymers II. Influence of physical ageing on antioxidant and oxygen mobility," *Polym. Degrad. Stab.*, vol. 79, no. 3, pp. 427–438, 2003.

[209] M. E. Vlachopoulou, P. S. Petrou, S. E. Kakabakos, A. Tserepi, K. Beltsios, and E. Gogolides, "Effect of surface nanostructuring of PDMS on wetting properties, hydrophobic recovery and protein adsorption," *Microelectron. Eng.*, vol. 86, no. 4–6, pp. 1321–1324, 2009.

[210] T. Myrstad and G. R. Fredriksen, "Removal of Fe(CO)5 from CO gas as detected by FTIR spectroscopy," *Chem. Eng. Technol.*, vol. 21, no. 3, pp. 297–299, 1998.

[211] T. C. Williams and C. R. Shaddix, "Contamination of carbon monoxide with metal carbonyls: Implications for combustion research," *Combust. Sci. Technol.*, vol. 179, no. 6, pp. 1225–1230, 2007.

[212] H. E. Carlton and J. H. Oxley, "Kinetics of the heterogeneous decomposition of iron

pentacarbonyl," *AIChE J.*, vol. 11, no. 1, pp. 79–84, 1965.

[213] M. Poliakoff and E. Weitz, "Shedding Light on Organometallic Reactions: The Characterization of Fe(CO)4, a Prototypical Reaction Intermediate," *Acc. Chem. Res.*, vol. 20, no. 11, pp. 408–414, 1987.

[214] P. W. N. M. van Leeuwen, *Homogeneous Catalysis*, vol. 3. 2004.

[215] D. E. Herrick, J. W. Tierney, I. Wender, G. P. Huffman, and F. E. Huggins, "Activity and Characterization of Coprocessing Catalysts Produced from an Iron Pentacarbonyl Precursor," *Energy and Fuels*, vol. 4, no. 3, pp. 231–236, 1990.

[216] T. W. Smith and D. Wychlck, "Colloidal iron dispersions prepared via the polymer-catalyzed decomposition of iron pentacarbonyl," *J. Phys. Chem.*, vol. 84, no. 12, pp. 1621–1629, 1980.

[217] J. L. Davidson, "Homogeneous catalysis," no. 8, pp. 346–373, 2007.

[218] A. D. King, R. B. King, and D. B. Yang, "Homogeneous Catalysis of the Water Gas Shift Reaction Using Iron Pentacarbonyl," *J. Am. Chem. Soc.*, vol. 102, no. 3, pp. 1028–1032, 1980.

[219] J. J. Pignatello, E. Oliveros, and A. MacKay, "Advanced oxidation processes for organic contaminant destruction based on the fenton reaction and related chemistry," *Crit. Rev. Environ. Sci. Technol.*, vol. 36, no. 1, pp. 1–84, 2006.

[220] S. C. George and S. Thomas, "Transport phenomena through polymeric systems," *Prog. Polym. Sci.*, vol. 26, no. 6, pp. 985–1017, 2001.

[221] F. Faupel, A. Thran, M. Kiene, T. Strunskus, V. Zaporojtchenko, and K. Behnke, "Diffusion Of Metals In Polymers And During Metal/Polymer Interface Formation," pp. 221–251, 2003.

[222] F. Faupel, R. Willecke, and A. Thran, "Diffusion of metals in polymers," *Mater. Sci. Eng. R Reports*, vol. 22, no. 1, pp. 1–55, 1998.

[223] M. Sonnenberg *et al.*, "Polymer-induced metal diffusion during plastic processing: A reason for deposit formation," *J. Polym. Eng.*, vol. 39, no. 5, pp. 472–480, 2019.

[224] N. Hordy, S. Coulombe, and J. L. Meunier, "Plasma functionalization of carbon nanotubes

for the synthesis of stable aqueous nanofluids and poly(vinyl alcohol) nanocomposites," *Plasma Process. Polym.*, vol. 10, no. 2, pp. 110–118, 2013.

[225] C. E. Baddour, F. Fadlallah, D. Nasuhoglu, R. Mitra, L. Vandsburger, and J. L. Meunier, "A simple thermal CVD method for carbon nanotube synthesis on stainless steel 304 without the addition of an external catalyst," *Carbon N. Y.*, vol. 47, no. 1, pp. 313–318, 2009.

[226] N. Hordy, *Direct growth of Carbon Nanotubes from Stainless Steel Grids and Plasma Functionalization for Poly (Vinyl Alcohol) Composite Production*, no. June. 2011.

[227] S. A. Trushin, W. Fuss, K. L. Kompa, and W. E. Schmid, "Femtosecond Dynamics of Fe(CO)5 Photodissociation at 267 nm Studied by Transient Ionization," *J. Phys. Chem. A*, vol. 104, no. 10, pp. 1997–2006, 2000.

[228] J. Z. Wen, C. F. Goldsmith, R. W. Ashcraft, and W. H. Green, "Detailed kinetic modeling of iron nanoparticle synthesis from the decomposition of Fe(CO)5," *J. Phys. Chem. C*, vol. 111, no. 15, pp. 5677–5688, 2007.

[229] G. McHale and M. I. Newton, "Global geometry and the equilibrium shapes of liquid drops on fibers," *Colloids Surfaces A Physicochem. Eng. Asp.*, vol. 206, no. 1–3, pp. 79–86, 2002.

[230] C. Luo and X. Wang, "Conditions for Barrel and Clam-Shell Liquid Drops to Move on Bio-inspired Conical Wires," *Sci. Rep.*, vol. 7, no. 1, 2017.

[231] H. B. Eral *et al.*, "Drops on functional fibers: From barrels to clamshells and back," *Soft Matter*, vol. 7, no. 11, pp. 5138–5143, 2011.

[232] W. Shi, M. J. Anderson, J. B. Tulkoff, B. S. Kennedy, and J. B. Boreyko, *Fog Harvesting with Harps*, vol. 10, no. 14. p. 11979−11986.

[233] P. S. Yadav, P. Bahadur, R. Tadmor, K. Chaurasia, and A. Leh, "Drop retention force as a function of drop size," *Langmuir*, vol. 24, no. 7, pp. 3181–3184, 2008.

[234] C. G. L. Fumridge, *Studies At Phase Interfaces I. the Sliding of Liquid Drops on Solid Surfaces and a Theory for Spray Retention*, vol. 17. p. 309−324.

[235] H. Vahabi, W. Wang, J. M. Mabry, and A. K. Kota, "Coalescence-induced jumping of droplets on superomniphobic surfaces with macrotexture," *Sci. Adv.*, vol. 4, no. 11, pp. 1–7, 2018.

[236] F. Liu, “Surface Energy Powered Processes upon Drop Coalescence by Surface Energy Powered Processes,” 2015.

[237] Y. Nam, H. Kim, and S. Shin, “Energy and hydrodynamic analyses of coalescence-induced jumping droplets,” *Appl. Phys. Lett.*, vol. 103, no. 16, 2013.

[238] A. Jenkins, M. H. Unsworth, and D. Fowler, *Acid Deposition at High Elevation Sites*, vol. 156, no. 1. 1990.

[239] F. Gassert, P. Reig, T. Luo, and A. Maddocks, “Aqueduct Country and River Basin Rankings,” 2013.

[240] Wikipedia, “Polarnost.” [Online]. Available: https://hr.wikipedia.org/wiki/Polarnost. [Accessed: 29-May-2020].

[241] Atlantic Ultraviolet Corporation, “Biolux Germicidal Ultraviolet Fixtures.” 2019.

[242] V. N. Khmelev, A. V. Shalunov, R. N. Golykh, V. A. Nesterov, R. S. Dorovskikh, and A. V. Shalunova, “Determination of the modes and the conditions of ultrasonic spraying providing specified productivity and dispersed characteristics of the aerosol,” *J. Appl. Fluid Mech.*, vol. 10, no. 5, pp. 1409–1419, 2017.

[243] V. Jokanović, A. M. Spasić, and D. Uskoković, “Designing of nanostructured hollow TiO 2 spheres obtained by ultrasonic spray pyrolysis,” *J. Colloid Interface Sci.*, vol. 278, no. 2, pp. 342–352, 2004.